CRUST AND UPPER MANTLE STRUCTURE BENEATH SOCORRO, NEW MEXICO, INFERRED FROM TELESEISMIC RECEIVER FUNCTIONS

by

Kraig E. Sheetz

Submitted in Partial Fulfillment of the Requirements for the Degree of Master of Science in Geophysics

New Mexico Institute of Mining and Technology
Socorro, New Mexico
May, 1992

ABSTRACT

The existence of crustal magma bodies in rift environments raises a number of questions concerning the transport and storage of magma that reaches crustal depths from some asthenospheric source region. The Rio Grande rift is a unique example of a continental rift where numerous studies have delineated a thin (about 150 m) magma body at a depth of about 19 km. The Socorro magma body covers an area of about 2000 km^2 in the central Rio Grande rift and provides an ideal site for studying magma transport in a continental rift.

In this study, source equalized teleseismic receiver functions are used to delineate the shear–wave velocity structure of the crust and upper mantle beneath station WTX in Socorro, New Mexico. Receiver functions were stacked for events that clustered in both distance and azimuth from station WTX. Seven events from the southeast, three events from the south, and four events from the northwest were used in this study. Inversion of the stacked receiver functions were constrained using upper crustal shear–wave velocities determined from a previous microearthquake study. Results show anomalously low shear–wave velocities (3.0–3.5 km/s) in the lower crust (20–30 km) which suggests elevated temperatures and possibly partial melting. However, the receiver functions contain strong arrivals corresponding to conversions and multiples from the Moho, which inversion solutions place at 33–35 km. According to forward modeling results, these arrivals would be severely attenuated if the lower crust had very low Q values associated with pervasive melting. It is therefore believed that the region beneath the Socorro magma body is transporting magma to mid–crustal depths via discrete conduits through anomalously hot but solid lower crust.

ACKNOWLEDGMENTS

I would especially like to thank my advisor, Dr. John Schlue, for his help and encouragement throughout the study, as well as for his trust in granting me "dweebing rights" on his new workstation. I thank George Zandt, who not only provided the modeling programs and instruction on their usage, but was very responsive to my questions about results interpretation. I also thank Chuck Ammon for his helpful comments and suggestions.

I would also like to thank Dr. Allan Sanford for always taking time to answer my questions about previous studies of the Socorro magma body, and Dr. Rick Aster for responding to my questions about signal processing.

TABLE OF CONTENTS

1. INTRODUCTION

Magma Chambers in Rift Environments

An interesting characteristic of rift environments, both oceanic and continental, is the presence of magma that has been injected into the crust from some asthenospheric source region. Of particular interest are questions concerning the origin, modes of transport, and accumulation of magma in the crust of rifts. While viable mechanisms exist for the migration of magma through the asthenosphere [*Turcotte,* 1982], magma migration through the lithosphere is much less understood, mainly due to the lack of relevant data. *Turcotte* [1982] discusses some of the possible mechanisms for lithospheric magma migration, but the main problem for modeling such magma migration is that a heated path must exist through which the magma can pass. In oceanic rifts, the lithosphere is considered to have negligible thickness [*Turcotte*, 1982], and magma transport has been modeled primarily with theoretical models of asthenospheric migration, hence many aspects of how a continuously heated path in the lithosphere is established remain poorly understood . In order to answer questions about the origin and transport of magma that becomes trapped in the crust beneath rifts, the detailed structure of the lower crust and upper mantle beneath magma bodies must be ascertained. Are mid–crustal magma bodies fed by one or more discrete conduits similar to those believed to exist in volcanic regions [*Ryan*, 1988]? Or are they underlain by a region of partial melt mush that extends to the top of the asthenosphere like that believed to exsist beneath fast spreading oceanic ridges [*Sinton and Detrick*, 1992]? Since the detailed velocity structure for each of these end member models would differ considerably, the shear wave velocity structure beneath magma bodies should provide important insight into these questions. The objective of this study is to investigate an area in the Rio Grande rift where the accumulation of magma at mid crustal depths provides an excellent opportunity to study the transport and storage of magma in a continental rift environment. Socorro, New

Mexico, located in the central Rio Grande rift (Figure 1.1) is a unique area where a number of geophysical observations indicate the presence of significant quantities of magma in the crust, a rare occurrence in continental rifts [*Sanford and Einarsson*, 1982]. I will use teleseismic receiver functions from events recorded at station WTX in Socorro, NM to model the detailed shear wave velocity structure of the lower crust and upper mantle in an attempt to learn more about the region that underlies the Socorro magma body.

Although magma is also known to accumulate in the crust of non–rift environments (e.g. subduction zones [*Reasenberg et al.*, 1980; *Duffield et al.*, 1980] and in association with intraplate volcanism [*Eaton and Murita*, 1960; *Machado*, 1974]), the following sections focus on a review of magma chambers found in the extensional regimes of oceanic and continental rifts. Magma bodies in oceanic rifts have been studied much more extensively [*Santon and Detrick*, 1992] than those in continental rifts, and can thus provide insight for understanding the continental analog.

Oceanic Rifts

Oceanic rift structures are associated with the diverging plate boundaries where new oceanic crust is generated by intrusion and extrusion of magma [*Sanford and Einarsson*, 1982]. To understand the evolution of the oceanic lithosphere, it is essential to understand from where the magma comes and how it is stored. In the past, geologic models for crustal formation at oceanic rifts assumed a magma chamber at some shallow but unspecified depth [e.g. *Chan*, 1974; *Sleep*, 1975, 1978; *Hall and Robinson*, 1979]. In most of these models, the magma chamber was assumed to be a rather large reservoir where partial melting, fractional crystalization, and magma mixing take place (Figure 1.2). A recent study by *Sinton and Detrick* [1992] however, discusses new geophysical evidence [*Detrick et al.*, 1987; *Kent et al.*, 1990; *Toomey et al.*, 1989] and petrological evidence [*Langmuir et al.*, 1986; *Mevel*, 1987; *Bloomer et al.*, 1989; *Sinton et al.*, 1991] that limits the potential size of crustal magma chambers to bodies that are volumetrically quite small. Using these new data, *Sinton and Detrick* [1992]

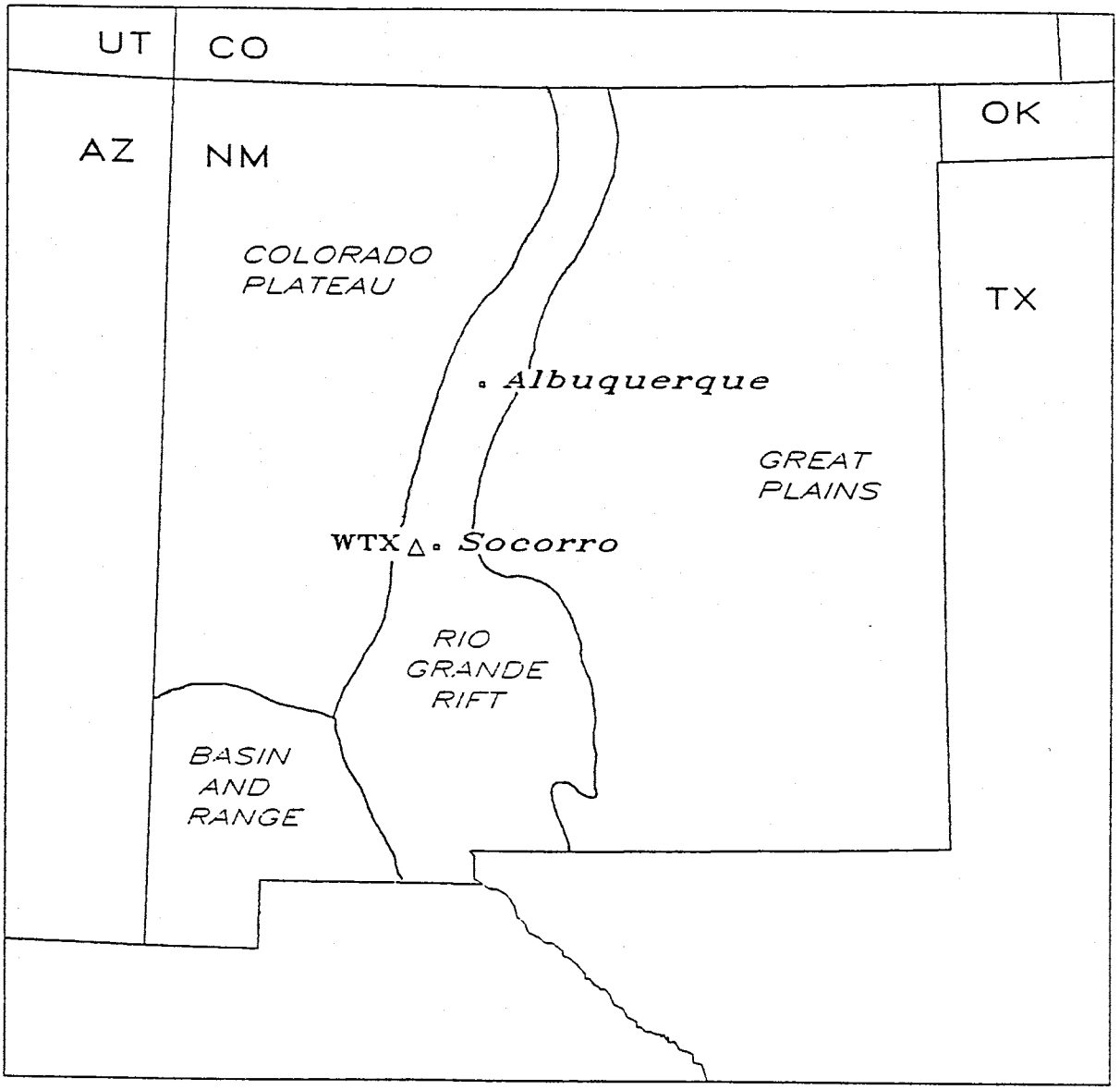

Figure 1.1. Socorro and station WTX in relation to the physiographic provinces in the state of New Mexico.

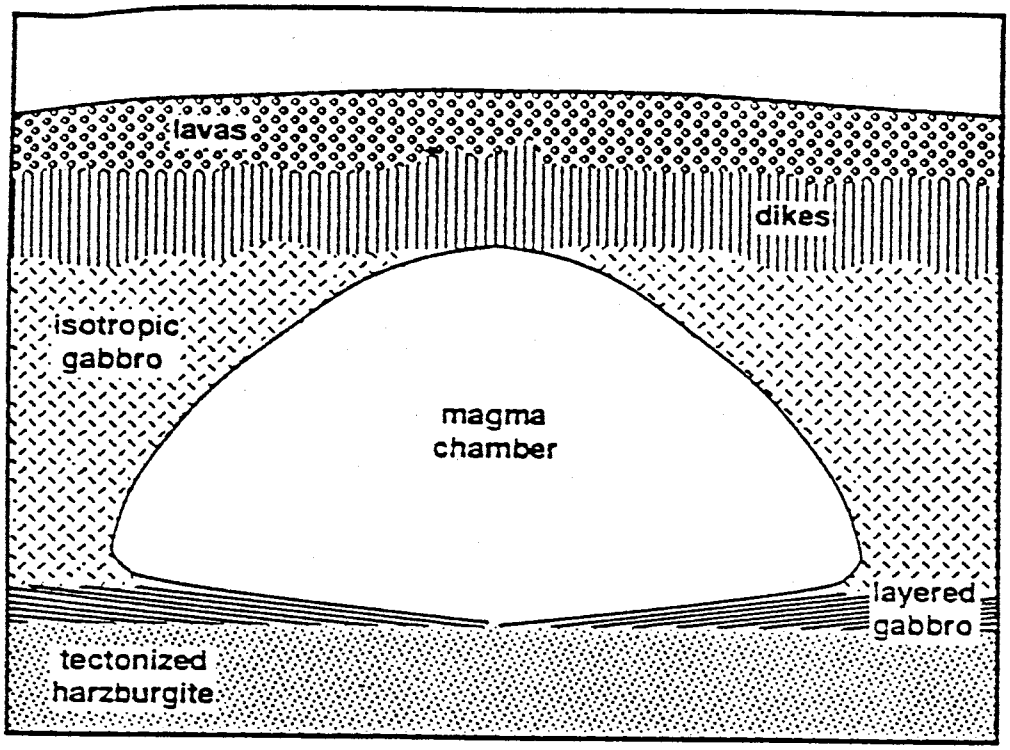

Figure 1.2. Schematic model showing the large molten magma chambers once envisioned to exist at mid–ocean ridges [from *Sinton and Detrick*, 1992].

propose a magma chamber model that includes a thin, narrow, sill–like body of melt overlying a thick, wide crystal mush zone at fast spreading ridges (Figure 1.3) and short–lived, largely mush filled chamber without a melt lens at slowly spreading ridges (Figure 1.4). Examples of oceanic ridges representing each of these spreading rate extremes are the East Pacific Rise (fast spreading) and the Mid–Atlantic Ridge (slow spreading).

In the East Pacific Rise (EPR), *Toomey et al.* [1990] found a large low velocity zone (LVZ) at the ridge crest that extended from a depth of 1–2 km to the base of the crust (about 5 km). However, analysis of high amplitude reflectors [*Vera et al.*, 1990] constrain the molten part of the LVZ to be less than a few hundred meters thick. This thin sill–like body of molten material is surrounded by a wide LVZ which, due to the small velocity anomaly, is thought to be predominantly solid with the possibility of minor amounts of melt [*Sinton and Detrick*, 1992]. A vertical P–wave velocity profile for a segment beneath the EPR is shown in Figure 1.5.

In the slower spreading Mid–Atlantic Ridge (MAR), low velocities and densities have been found in sections of the rift [*Fowler*, 1976; *Louden et al.*, 1986], but no geophysical evidence has been found for crustal magma chambers. Microearthquake studies [*Toomey et al.*, 1985, 1988] found that earthquakes can occur at depths greater than 8 km beneath the MAR, suggesting that magma injection takes place through crack propagation or via thin, intermittent, and possibly vertical magma bodies [*Sanford and Einarsson*, 1982]

Continental Rifts

There are only four continental rifts that are known to have Cenozoic thermal activity: The Baikal rift, The East African rift (the Kenya rift), the Rhine Graben and the Rio Grande rift [*Morgan*, 1982]. Whether these continental rifts are classified as active or passive in nature (Figure 1.6) (see *Sengor and Burke* [1978] and *Baker and Morgan* [1981] for details on the active and passive classification of continental rifts), a common feature seems to be asthenospheric upwelling or modification of the uppermost mantle beneath the rift axis

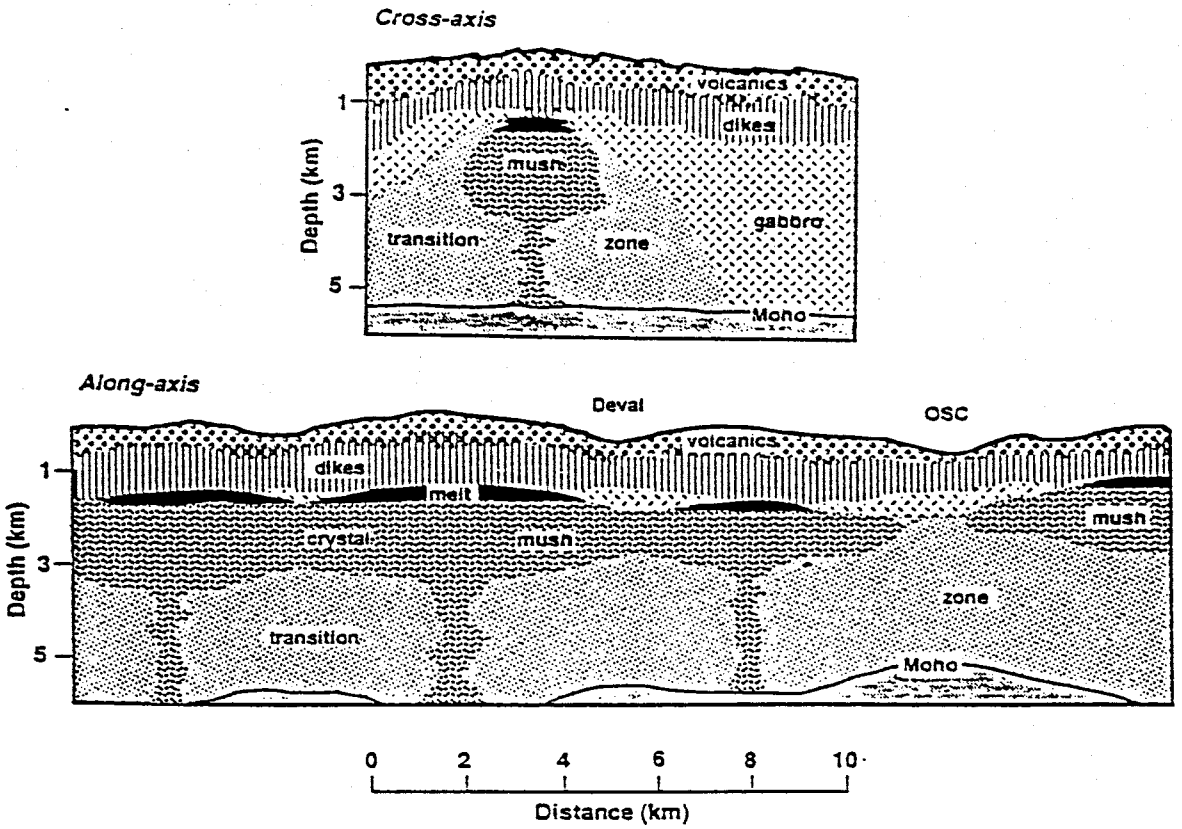

Figure 1.3. Interpretive model of a magma chamber along a fast spreading (high magma supply) ridge like the East Pacific Rise, based on recent geophysical and petrological constraints. The essential elements of this model are a narrow, sill–like body of melt 1–2 km below the ridge axis that grades downward into a partially solidified crystal mush zone, which is in turn surrounded by a transition zone to the solidified, but still hot, surrounding rock [from *Sinton and Detrick*, 1992].

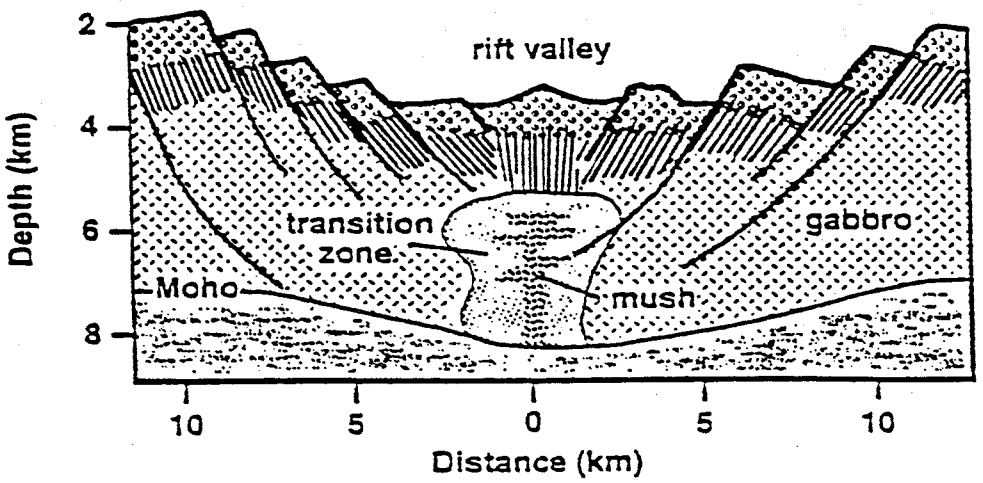

Figure 1.4. Interpretive model of a magma chamber beneath a slow spreading (low magma supply) ridge like the Mid–Atlantic Ridge, based on recent geophysical and petrological constraints. Such ridges are unlikely to be underlain by an eruptable magma lens in any steady state sense. A dike–like mush zone is envisioned beneath the rift valley forming small sill–like intrusive bodies which progressively crystallize to form oceanic crust [from *Sinton and Detrick,* 1992].

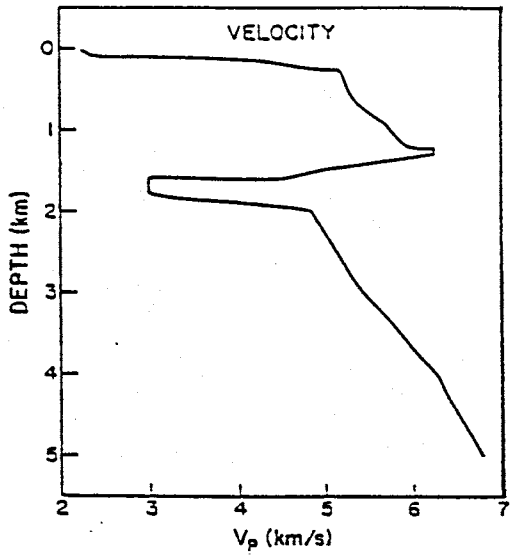

Figure 1.5. Vertical profile in P−wave velocity (from the data of *Vera et al.* [1990] and *Toomey et al.* [1990]) beneath the East Pacific Rise axis near 9°N [after *Sinton and Detrick*, 1992].

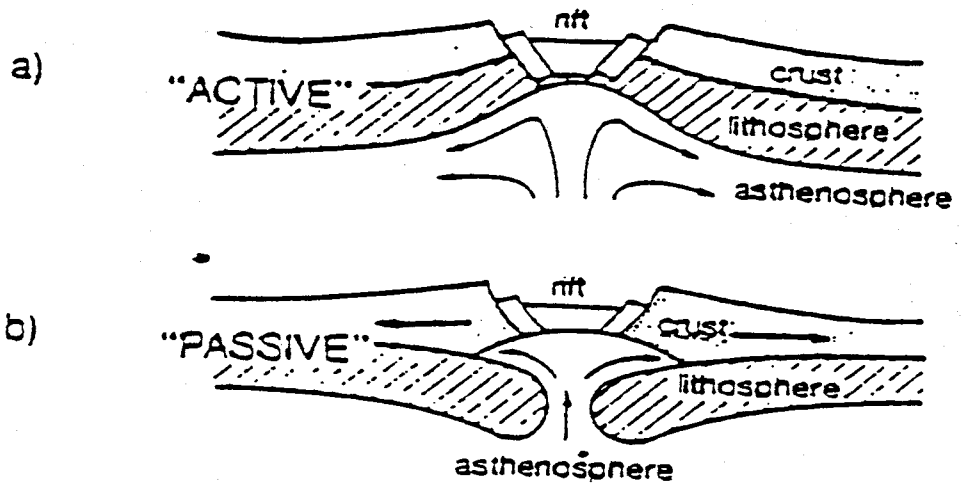

Figure 1.6. Generalized models showing two different aspects of the rifting process [after *Olsen et al.*, 1987].

[*Olsen,* 1983]. In some studies, the above–average heat flow values found in rifts [*Morgan,* 1982] have been attributed to deep convective motion of ground water, but *Lachenbruch and Sass* [1977] present arguments that attribute the excess heat in continental rifts to magma rising from the asthenosphere. *Morgan* [1982] summarizes the heat flow studies for the above rifts, but the question of whether the anomalously high heat flow results from water circulation or magmatic processes remains unclear in most cases. Even though the relatively small number of active volcanoes along continental rifts [*MacDonald*, 1972] suggests that detectable amounts of magma rising into the crust from the asthenosphere may not be commonplace [*Sanford*, 1983], each of the four continental rifts listed above has some geophysical observations (e.g. low velocities, low density, high heat flow) that appear to require some degree of melting in the upper mantle [*Sanford and Einarsson,* 1982]. *Olsen* [1983] compares the P–wave velocities (Figure 1.7), and summarizes the knowledge of the crustal structure (Table 1.1) for the four Cenozoic continental rifts. Only one of these continental rifts, the Rio Grande rift (RGR), contains an area where consistent geophysical evidence provides the location and dimensions of an accumulation of mid–crustal magma. In the central Rio Grande rift, microearthquake seismograms from an array of seismographs contain strong reflected phases indicating a thin, flat lying magma body at mid crustal depth (about 19km) [*Sanford et al.,* 1973, 1977; *Ake and Sanford,* 1988] which has an areal extent of at least 2000 km^2 [*Hartse and Sanford,* 1992]. Recent studies [e.g. *Harste*, 1991] have confirmed the existence of, depth to, and crustal structure above, the magma body. However, little is known about the detailed nature of the lower crust and upper mantle beneath the magma body.

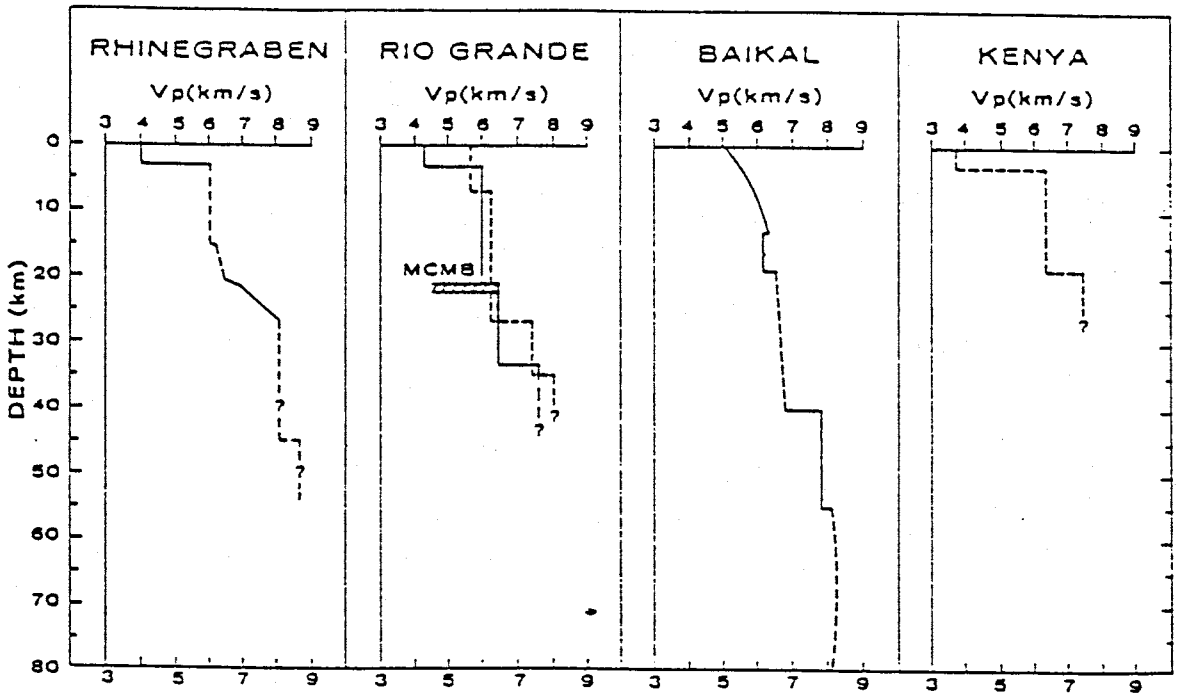

Figure 1.7. Comparison of compressional seismic velocity versus depth for the central axial region of four major Cenozoic continental rifts. The Moho (not labeled) is usually defined as a discontinuity or sharp gradient where V_p increases from about 7.4 km/s to about 8.0 km/s. V–Z functions are dashed where details of complex or show large lateral variations. ? denotes regions of uncertainty. MCMB for Rio Grande rift indicates the depth range where midcrustal magma bodies are observed in central New Mexico [from *Olsen*, 1983].

TABLE 1.1. Distinctive deep features of Cenozoic continental rifts.

Item	Structural property	Rhinegraben	Rio Grande	Baikal	Kenya (Gregory)
(1)	Moho depth (km):				
	axis	20–25 (transition zone)	34	35–38	20(?)
	flanks	30	45(W) 50(E)	40–42	unknown
(2)	Axial P_n velocity (km/s)	8.1	7.6	7.6–7.7	7.4–7.6(?)
(3)	Anomalous mantle	? (transition)	yes	yes	yes(?)
(4)	Mantle anisotropy	yes (E. flank)	insufficient data	not reported	no data
(5)	Upper crustal ductile layer	?-masked by sediment multiples	no(?), but see (6)	yes	insufficient data
(6)	Midcrustal magma ponding	no(?) but see (5)	yes	?	insufficient data

[from *Olsen*, 1983].

The Socorro Magma Body

Seismograms from microearthquakes in the Socorro area of the RGR contain distinct reflected phases from a mid–crustal discontinuity. *Sanford et al.* [1973] found that the strength and travel–times of two strongly reflected phases, S_zS and S_zP (see Figure 1.8) indicate that the mid–crustal reflector can best be represented by an extensive crustal discontinuity underlain by magma. Further studies by *Sanford et al.* [1977] and *Rinehart* [1979] of these anomalous reflections concluded that a thin, relatively flat magma body near 19 km depth was responsible for these impulsive reflection phases. *Hartse and Sanford* [1992] found that the areal extent of the magma body was at least 2000 km^2. In 1975 and 1976, P–wave reflection profiles conducted by the Consortium for Continental Reflection Profiling (COCORP) [*Brown et al.*, 1979] confirmed the existence of a strong reflector near 19 km. *Ake and Sanford* [1988] used digitally recorded S_zS and S_zP phases to study the thickness and nature of the magma body. Their preferred model consisted of a two layer structure where a layer 72 m thick of full melt (V_p = 2.5 km/s) overlies a layer 55 m thick of crystalline mush (or partially solidified magma) (V_p = 4.5km/s).

Crustal Structure Around the Magma Body

The average velocity structure of the crust above the magma body appears to be well constrained. *Rinehart and Sanford* [1981] found the average shear wave velocity to be 3.41 km/s. *Harste* [1991] combined direct and reflected phases in an inversion which allowed him to simultaneously resolve both the depth to the magma body and the average compressional (P) and shear (S) wave velocities above the magma body (Figure 1.8). He found the depth to the magma body to be 18.75 ± 0.28 km. By dividing the upper crust into two layers, he found the top 10 km to have average velocities V_p = 5.95 ±0.05 km/s and V_s = 3.41 ±0.04 km/s, and the upper crust (the layer from 10 km to the top of the magma body) to have average velocities V_p = 5.80 ± 0.08 km/s and V_s = 3.44 ± 0.07 km/s.

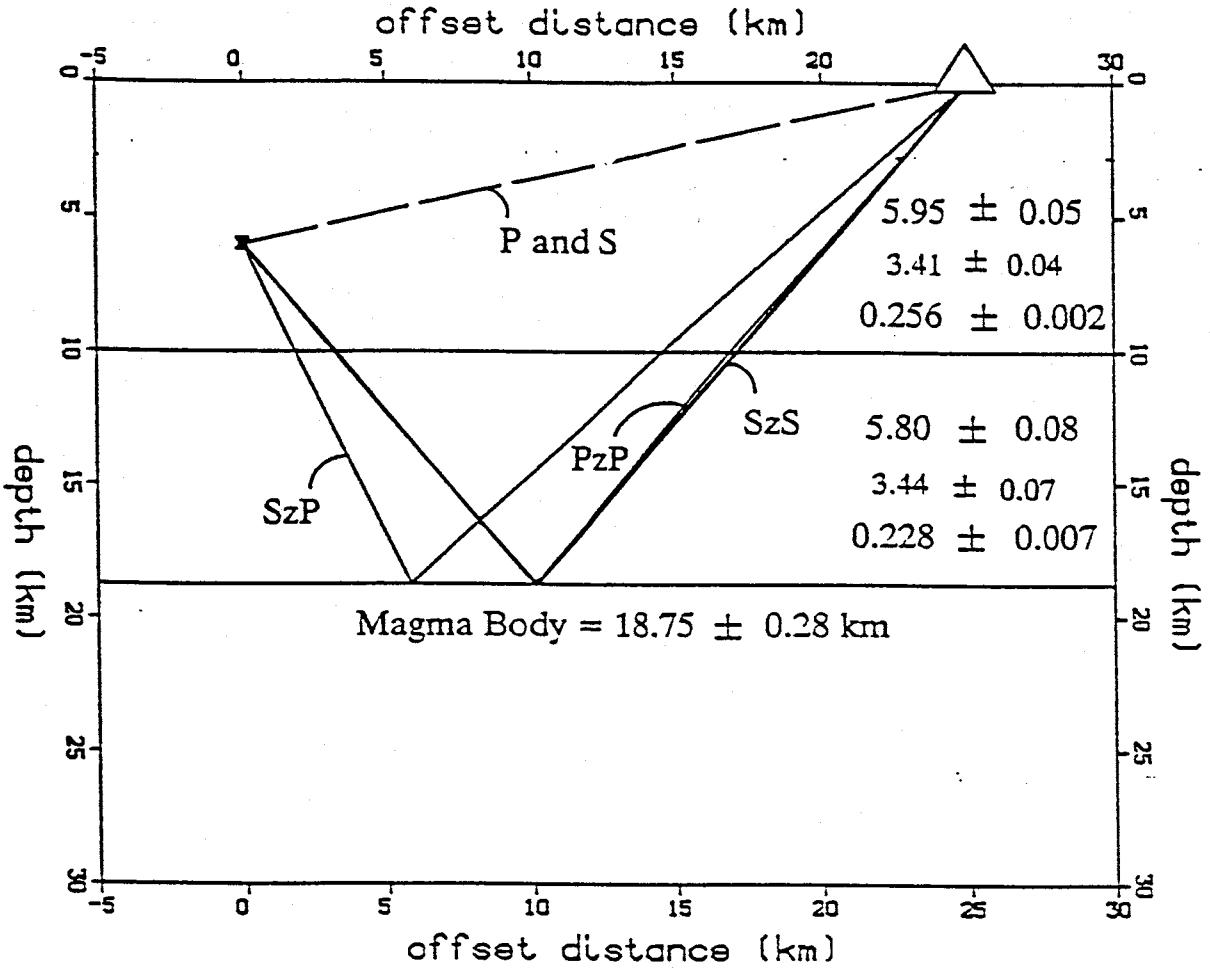

Figure 1.8. Velocity model for the Central Rio Grande rift as determined by *Hartse* [1991] from reflections off of the top of the mid–crustal magma body (sample rays that produce reflections on microearthquake coda are shown). The first layer is between 0 and 10km and the second layer is between 10km and the surface of the magma body. Within each layer, V_p is listed first, then V_s, and finally Poisson's ratio. Velocities are given in km/s. [from *Hartse*, 1991].

The nature of the crust beneath the magma body has not been as easy to determine. Magnetotelluric (MT) data [*Jiracek et al.*, 1979; *Hermance and Pederson*, 1980] and heat flow data [*Reiter et al.*, 1975, 1978, 1979] indicate elevated temperatures in the lower crust and upper mantle in the rift, while *Decker and Smithson*, [1975] present steady−state conduction models of the rift that imply considerable melting in the lower crust and upper mantle. The velocities in the lower crust have been investigated with refraction studies, but only average P−wave velocities between the magma body and the Moho were resolved. *Olsen et al.* [1979] used an unreversed refraction line in central New Mexico to obtain an average P−wave velocity of 6.4 km/s in the lower crust with a Moho depth of 33.7 km. *Singer* [1989] used time−term analysis and also obtained a 6.4 km/s average P−wave velocity in the lower crust with a Moho depth of 33.5 km. Attempts to resolve average shear wave velocities beneath the magma body have been made with surface wave studies, but available resolution at such depths is poor. *Schlue et al.* [1986] used Rayleigh wave phase velocities to determine the upper crustal shear wave structure of the Albuquerque − Belen basin, but the results for the lower crust were heavily dependant on the initial model.

Transport of Magma to the Socorro Magma Body

There is much geophysical evidence that the Socorro magma body is still active. Most of the earthquake activity in the Socorro area occurs in swarms, which is indicative of the movement of magma [*Sanford et al.*, 1979]. *Reilinger et al.* [1980] provide geodetic evidence for historical crustal doming above the magma body corresponding to an average inflation rate within the magma body on the order of $0.01-0.02$ km^3/yr. In regions with greater magma intrusion rates, the structure of the magmatic systems is much less elusive. *Eaton* [1962] was the first to model the magma ascent, storage and rift zone intrusion processes beneath the Kileaua volcano in Hawaii, and *Klein et al.* [1987] tracked earthquake swarms to show the evolutionary development of propagating fractures from magma injection beneath Kileaua. However, it can be argued that Kileaua is a unique geophysical environment. Rarely is so vigorous a magma transport process available to monitor seismically. Moreover, Hawaii is agreed to be a

"hot spot" and not part of a mid–ocean rift system. Certainly, the magmatic processes in the RGR are on a much smaller scale. *Hartse* [1991] used reflections from the magma body to better constrain earthquake focal depths and found that the seismogenic zone in the Socorro area lies between 3–10 km deep, with the deepest event just slightly over 10 km. Since no earthquakes have been located beneath the magma body [*Sanford,* personal communication, 1992] the magma transport process, apparently aseismic in nature, remains undetermined.

Olsen et al. [1987] present one interpretation of the collective data on the RGR in a cartoon of a cross section normal to the rift axis (Figure 1.9). In this figure, the crust between the magma body and the top of the upwelling asthenosphere is transected by thin magma feeder conduits and local dikes. *Olsen et al.* [1987] believe that the volumes and masses of mafic material intruded into the crust must be less than a few (possibly 10) percent, because a large intrusion of mafic material into the lower crust would increase the density and hence increase the seismic velocity, which is contrary to the observed low (6.4 – 6.5 km/s) compressional wave velocities. *Olsen et al.* [1987] do emphasize that although the features of the Socorro magma body are included in the cartoon to illustrate its importance, the Socorro area is about 100 km north of their best data.

The existence of a magma chamber in a rift environment provides an interesting opportunity to investigate the many unanswered questions concerning the migration of magma through the upper mantle and lower crust. While much research has been aimed at answering such questions for magma chambers in oceanic rifts, the Socorro magma body presents an ideal opportunity to study magma transport in continental rifts. As mentioned above, microearthquake studies [e.g., *Harste,* 1991; *Ake and Sanford,* 1988; *Rinehart and Sanford,* 1981; *Sanford et al.,* 1977] have been successful in determining the location of, and the crustal structure above the Socorro magma body. Refraction studies [e.g., *Singer et al.,* 1989; *Olsen et al.,* 1979; *Toppozada and Sanford,* 1976] have been used to determine the average P–wave velocities of the crust beneath the magma body, but have to assume a Poisson's ratio in order to estimate shear wave velocities.

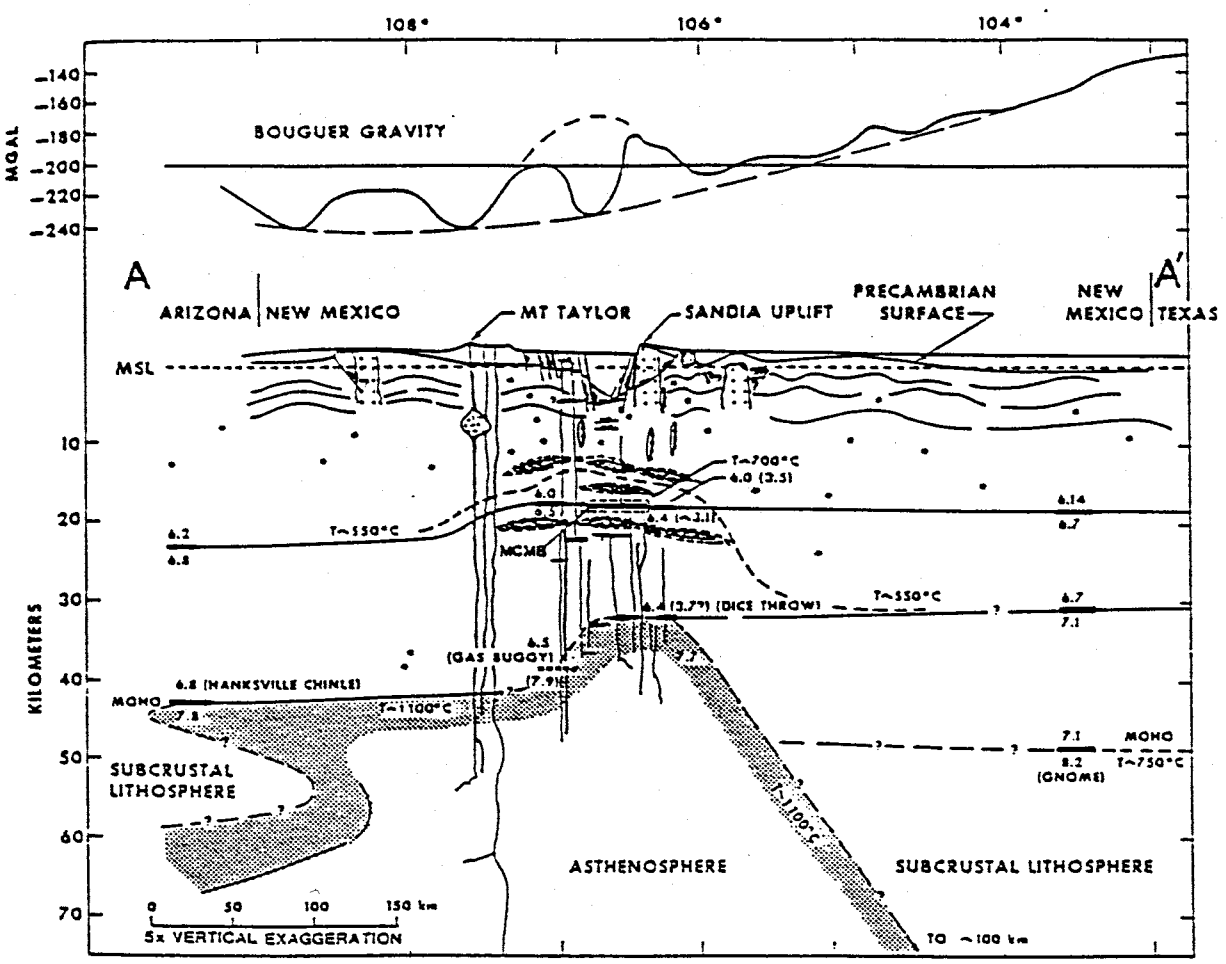

Figure 1.9. Cross-section through northern Albuquerque-Belen basin. Locations of intracrustal boundaries interpreted from travel times and record sections of correlated phases are plotted as short, heavy lines at longitudes where seismic profiles intersect the cross-section. Numbers are P-wave velocities in km/s (numbers in parentheses are S-wave velocities. Profiles are identified by locations of shotpoints (Chinle-Hanksville: *Roller*, 1965) or by code names of the main source explosions (DICE THROW: *Olsen et al.*, 1979; GASBUGGY: *Toppozada and Sanford*, 1976; Gnome: *Stewart and Pakiser*, 1962). The Chinle, GASBUGGY, and GNOME profiles were obtained at a relatively early technological state in U.S. crustal profiling efforts, when station spacing was relatively course (10-50km) and true amplitude/waveform data were inadequate to permit more than estimates of possible velocity gradients or fine structure in principal crustal layers. DICE THROW average station spacing was about 3 km, allowing better gradient estimates using modern synthetic seismogram modeling techniques. Generalized distribution of earthquake hypocenters in the upper crustal layer is shown by asterisks, as are the specific deep crustal events of 1976/1977 (*Sanford et al.*, 1979; *Wong et al.*, 1984). A Bouguer gravity anomaly profile at the latitude of the cross-section is shown at the top (*Cordell et al.*, 1982). The mid-crustal magma body (MCMB) at Socorro has been projected into the cross-section. Locations of basaltic dikes, though schematic, are based partly on heat flow data (e.g. *Clarkson and Reiter*, 1984) [from *Olsen et al.*, 1987].

Surface wave studies [e.g., *Schlue et al.*, 1976; *Keller et al.*, 1979] have been used in the Rio Grande rift to delineate the shear wave structure of the crust, but resolution is poor at lower–crustal and mantle depths. A recent study by *Aldouri et al.* [1992] found an average lower–crustal shear wave velocity of 3.7–3.8 km/s from Rayleigh wave dispersion along the propagation path between El Paso, Texas and Albuquerque, New Mexico. In this study, I present the shear wave structure of the crust and uppermost mantle beneath Socorro, New Mexico, as determined from the modeling of teleseismic receiver functions. Receiver function modeling, unlike most geophysical methods, can resolve the detailed shear wave velocity structure of the lower crust and can thus be a valuable tool for understanding the migration of magma to mid–crustal depths. The characteristics of teleseismic receiver functions which enable one to resolve features of the lower crust and upper mantle are described in the following chapter.

2. METHOD

Characteristics of the Teleseismic P Waveform

Teleseismic P waves arrive at a recording station with both a constant and relatively high phase velocity [*Ammon and Zandt*,1990]. The high phase velocity implies a steep angle of incidence, resulting in the vertical component being dominated by P waves, and the horizontal components primarily recording shear wave motion. Because the phase velocity is constant, a plane wave approximation is justified, thus simplifying the study of resulting ground motion. Under the assumption of plane waves in a homogeneous medium (layer–cake earth model), purely SV–polarized wave motion will have zero displacement in the direction normal to the plane [*Aki and Richards*, 1980]. Therefore, rotation of the horizontal components of a teleseismic P waveform into radial and tangential components will result in conversions of the P–S type being preferentially recorded on the radial component of ground motion. The existence of energy in the tangential P waveform cannot be explained with a homogeneous plane–layered earth models, since the P–SV and SH wave systems are decoupled in a layer–cake system [*Langston*, 1979].

A single–station seismogram representing the displacement of the earth's surface due to a teleseismic body wave contains information about the source time function, the earth's velocity structure near the source, the velocity structure near the turning point of the ray, and the crust and upper mantle structure under the observation point [*Langston*, 1977a]. In order to delineate the structure of the crust and upper mantle beneath a single station, the response of the structure (Figure 2.1) must be isolated from the rest of the information contained in the teleseismic P waveforms by removing the unwanted source and path effects. The resulting waveform, the receiver function, contains valuable information for modeling the structure beneath the receiver. Figure 2.2, which

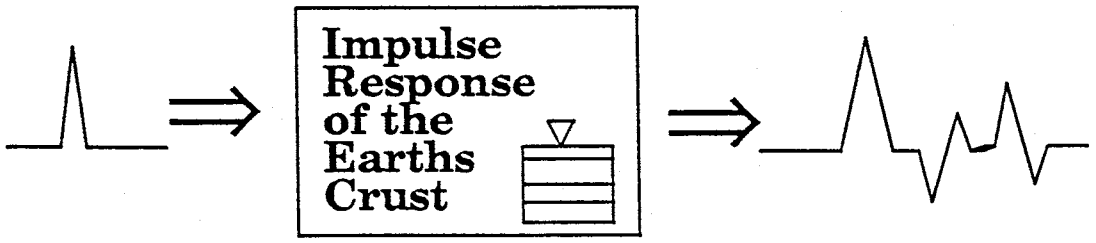

Figure 2.1. Schematic diagram illustrating the receiver function (waveform at right) as the response of a layered earth structure to an impulse function.

shows a ray diagram and corresponding synthetic radial receiver function, illustrates the near–receiver multiples and converted phases which result from an incident plane P–wave on some interface.

The Receiver Function

Source Equalization

The method of isolating the receiver function, developed by *Langston* [1979], is called source equalization. This method assumes that the response D(t) of a three component station to a teleseismic P wave can be given by

$$D_V(t) = I_V(t) * S(t) * E_V(t) \quad (1)$$

$$D_R(t) = I_R(t) * S(t) * E_R(t) \quad (2)$$

$$D_T(t) = I_T(t) * S(t) * E_T(t) \quad (3)$$

where I(t) is the impulse response of the recording instrument, S(t) is the effective source time function of the impinging wave, E(t) is the impulse response of the earth structure, * is the convolution operator, and subscripts V, R, and T denote the vertical, radial and tangential components respectively

As mentioned above, phase conversions of the P–to–S type will be recorded mainly on the horizontal components, setting them apart from the vertical component which consists of a large direct arrival followed by only minor arrivals due to crustal reverberations and phase conversions [*Owens,* 1984]. The source equalization scheme therefore assumes that the response of the vertical component to the incoming teleseismic wave will approximate the Dirac delta function, or

$$E_v(t) \approx \delta(t) \quad (4)$$

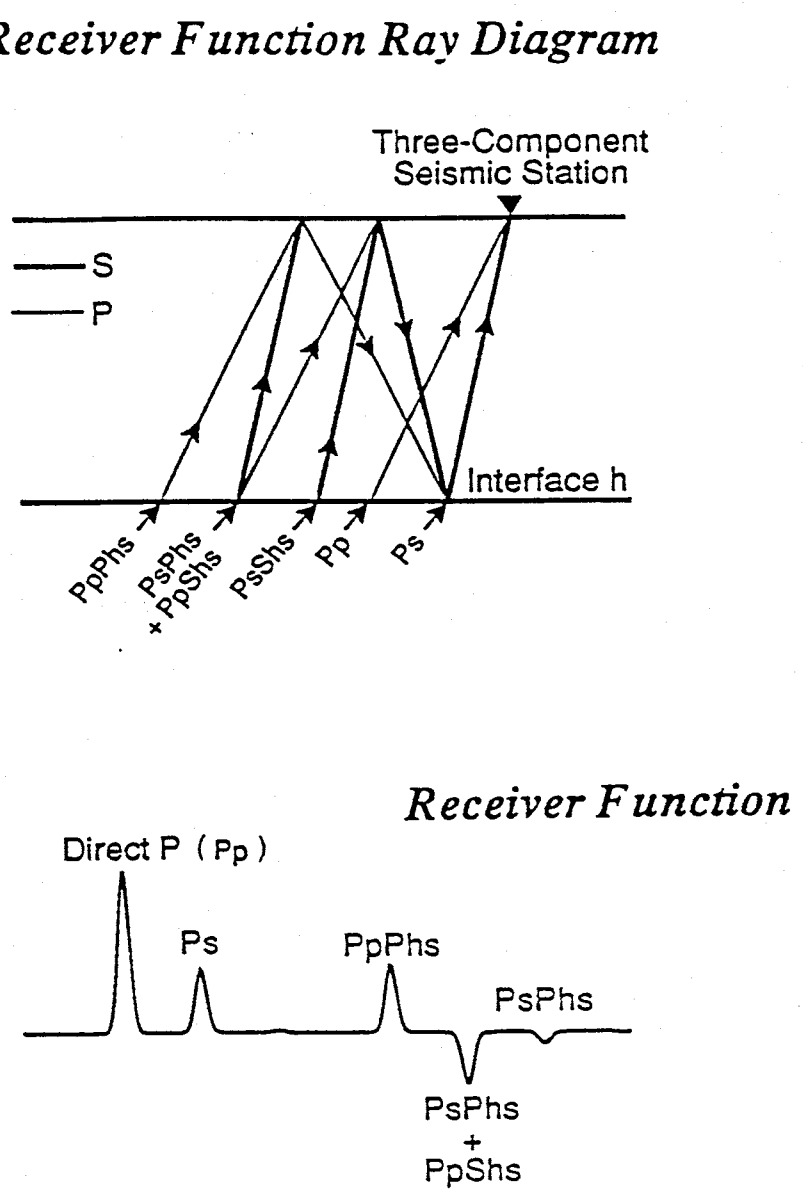

Figure 2.2. (Top) Simplified ray diagram showing the major P–to–S converted phases which comprise the radial receiver function for a single layer over a half-space. (Bottom) The waveform corresponding to the diagram above [after *Ammon,* 1991].

Equation (1) can thus be written

$$D_V(t) \approx I_V(t) * S(t) \tag{5}$$

This makes $D_V(t)$ approximately equal to just those pieces of information that need to be removed from the observed seismograms. Therefore, if the instrument responses for all three of the instruments are matched ($I_V = I_R = I_T$), the radial and tangential responses of the earth's structure, $E_R(t)$ and $E_T(t)$, can be isolated by deconvolving $D_V(t)$ from $D_R(t)$ and $D_T(t)$. This process can be written as a simple ratio in the frequency domain, i.e.,

$$E_R(\omega) \approx \frac{D_R(\omega)}{D_V(\omega)} \quad \text{and} \quad E_T(\omega) \approx \frac{D_T(\omega)}{D_V(\omega)} \tag{6}$$

Taking the Fourier transform of $E_R(\omega)$ gives the radial receiver function $[E_R(t)]$, which is simply the time series obtained from the complex spectral ratio of the radial response to the vertical response. In practice, the deconvolution is done in the frequency domain using the water–level method of *Clayton and Wiggins* [1976] where equation (6) is written as

$$E_R(\omega) = \frac{D_R(\omega)\ D_Z^*(\omega)}{\phi(\omega)}\ G(\omega) \tag{7}$$

where

$$\phi(\omega) = \max\left\{D_Z(\omega)\ D_Z^*(\omega),\ c \cdot \max\left(D_Z(\omega)\ D_Z^*(\omega)\right)\right\} \tag{8}$$

and where * denotes complex conjugation and c is the water level parameter which determines the minimum spectral amplitude allowed in the denominator. c is expressed as a fraction of the maximum spectral amplitude.

The function G(ω) is a Gaussian smoothing filter and can be written as

$$G(\omega) = \zeta \exp\left(- \frac{\omega^2}{4a^2} \right) \tag{9}$$

where the constant ζ is used to normalize the filter to unit amplitude in the time domain, and the parameter a controls the width of the Gaussian pulse that filters the receiver function.

The purpose of the water–level parameter is to keep the deconvolution from becoming unstable due to very small values (spectral holes) in the denominator of equation 7. The deconvolution codes developed by *Ammon* [1991] perform a suite of deconvolutions with varying values of c (e.g. 0.1, 0.01, 0.001, 0.0001), to find the smallest water level parameter that produces a stable deconvolution. The closer c is to zero, the closer the process becomes to an unrestricted deconvolution. Figures 2.3, 2.4 and 2.5 illustrate the need for the water–level parameter. Figure 2.3 shows sample amplitude spectra for vertical and radial components of displacement. Note the spectral holes in the vertical component at points A and B, corresponding to ~0.015 Hz and ~0.3 Hz respectively. Figure 2.4 shows the radial receiver function resulting from the deconvolution with a water–level parameter which is very close to zero. The receiver function is contaminated with excessive energy at periods of ~3 seconds and ~65 seconds, which corresponds to the two frequencies where the vertical component was underrepresented. To alleviate this problem, a water level of 0.01 can be applied so that a minimum amplitude of 0.01 multiplied by the maximum amplitude will be allowed in the denominator. In Figure 2.3, the dotted line represents this minimum amplitude that is allowed in the denominator of the spectral division. Figure 2.5 shows the radial receiver function resulting from a deconvolution with a water level of 0.01. Although there may be a hint of 0.3 Hz energy, the deconvolution is considerably more stable.

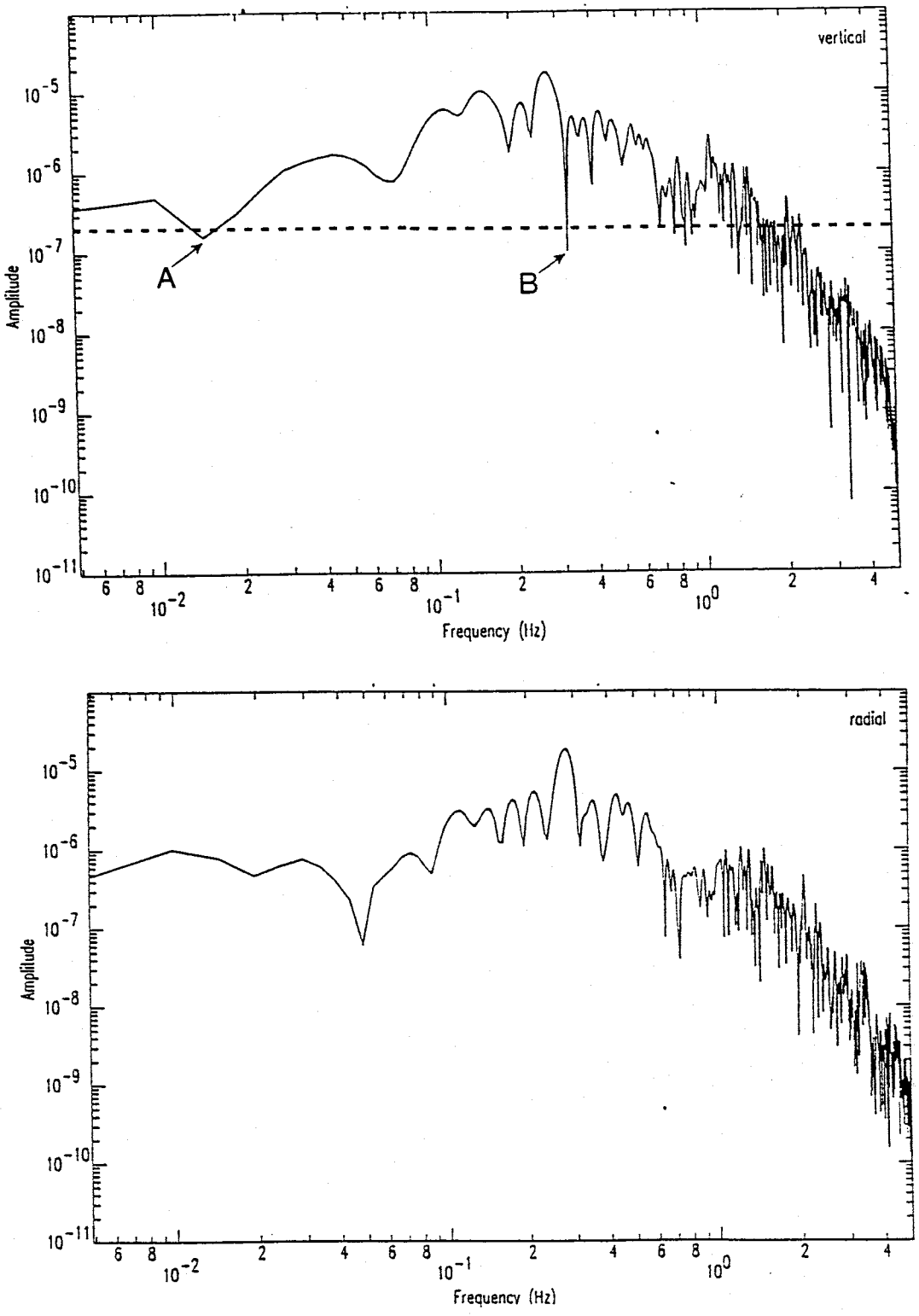

Figure 2.3. Amplitude spectra for the vertical (top) and radial (bottom) components for the first 40 seconds of a sample teleseismic P−waveform. Spectral holes in the vertical components are marked with letters A (−0.015 Hz) and B (− 0.3 Hz). The dotted line marks the minimum amplitude allowed in the deconvolution given a water−level value of 0.01.

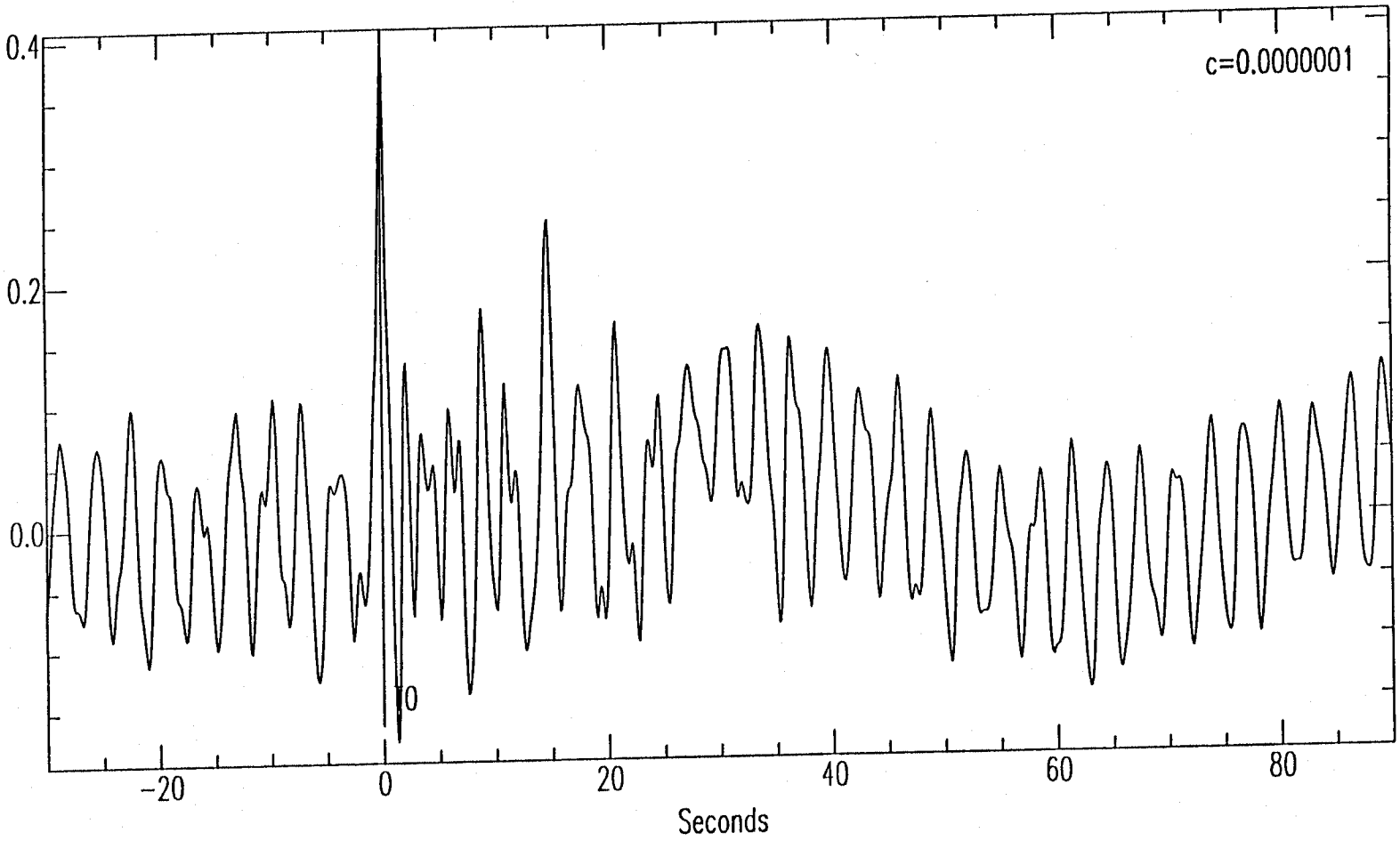

Figure 2.4. Unstable recevier function created from the deconvolution of the vertical component from the radial component for the sample signal shown if Figure 2.3. A water–level parameter near zero (c=0.0000001) was used in the deconvolution. The frequency of the contaminating energy in the receiver function corresponds to the frequencies at which the vertical component contained holes (A and B in Figure 2.3).

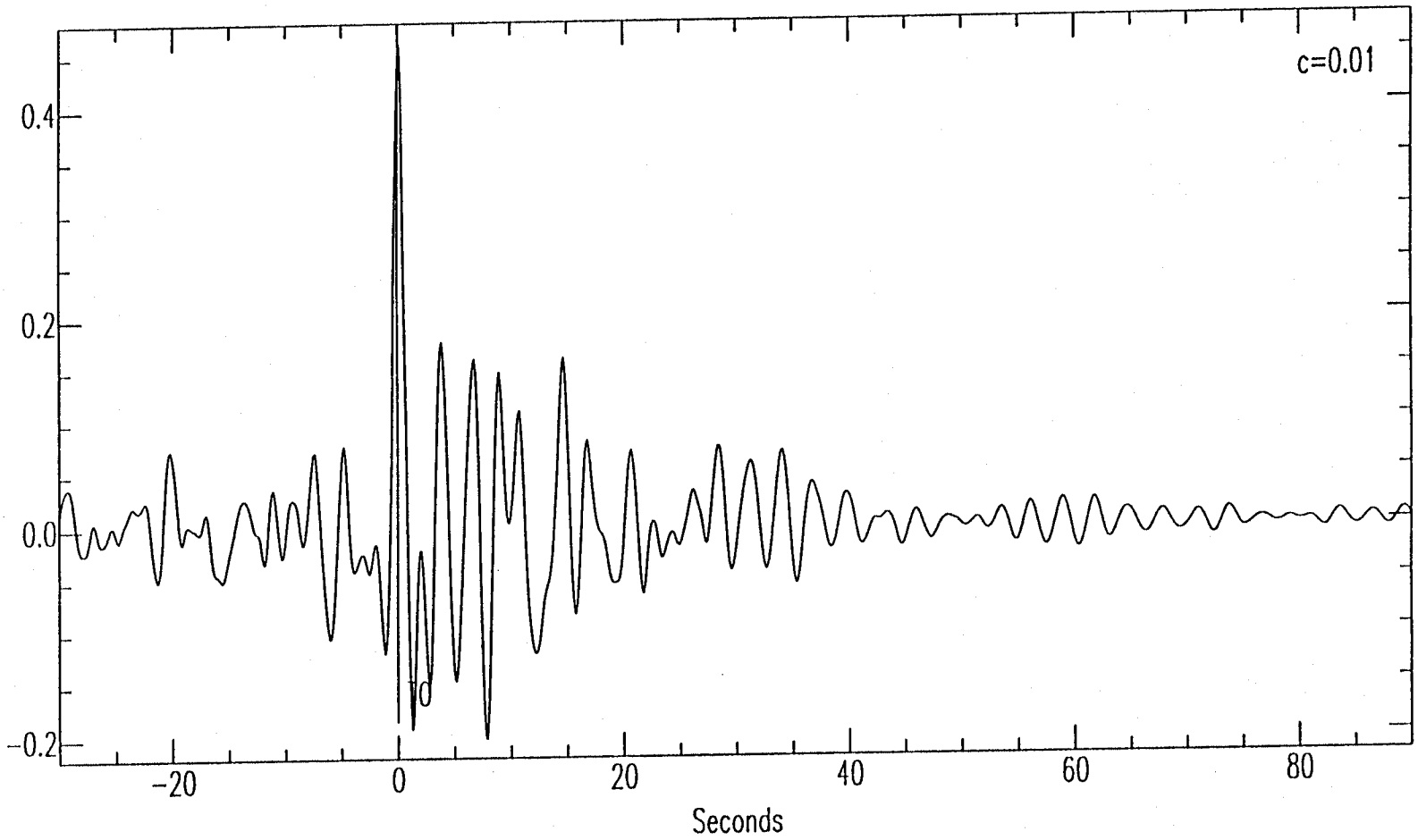

Figure 2.5. Stable receiver function created from the deconvolution of the vertical component from the radial component for the sample signal shown if Figure 2.3. A water−level parameter of 0.01 was used in the deconvolution. The minimum allowable amplitude in the vertcal component (marked by the dotted line in Figure 2.3) fills the spectral holes enough to stabalize the deconvolution and remove the contaminating energy found in Figure 2.4.

The Gaussian width value, a, is used to filter out the high frequencies that may represent noise from the deconvolution. Figure 2.6 is an example of two deconvolutions of the same data with the same water level (c=0.01) but different filter width values. Unless one is attempting to resolve very detailed structure (layers less than 2 km thick) the receiver function with the lower Gaussian filter width (a=1.0) in Figure 2.6 would probably be more desirable for modeling because much of the high frequency content, which may be noise, has been removed.

What the Receiver Function Represents

To illustrate how the individual peaks and troughs of the radial receiver function correspond to the arrivals on the original radial response to an incident plane P wave, *Ammon* [1991] provided a simple case where only three arrivals occur on the radial and vertical components – the direct P, a later arriving S representing a P–to–S conversion at some horizontal interface, and a P multiple from a horizontal interface. To begin, consider the response of a one dimensional velocity structure to an incident plane P wave:

$$D_R(t) = \sum_{k=0}^{n} R_k \, S(t - t_k) \tag{10}$$

and

$$D_Z(t) = \sum_{k=0}^{n} Z_k \, S(t - t_k) \tag{11}$$

where S(t) is the source time function, t_k is the arrival time of the k^{th} ray (k=0 is direct P), and R_k and Z_k are the amplitudes of the k^{th} arrival. The summation is over n such rays (n=3 in the simple example). In the frequency domain, equations 10 and 11 can be written as

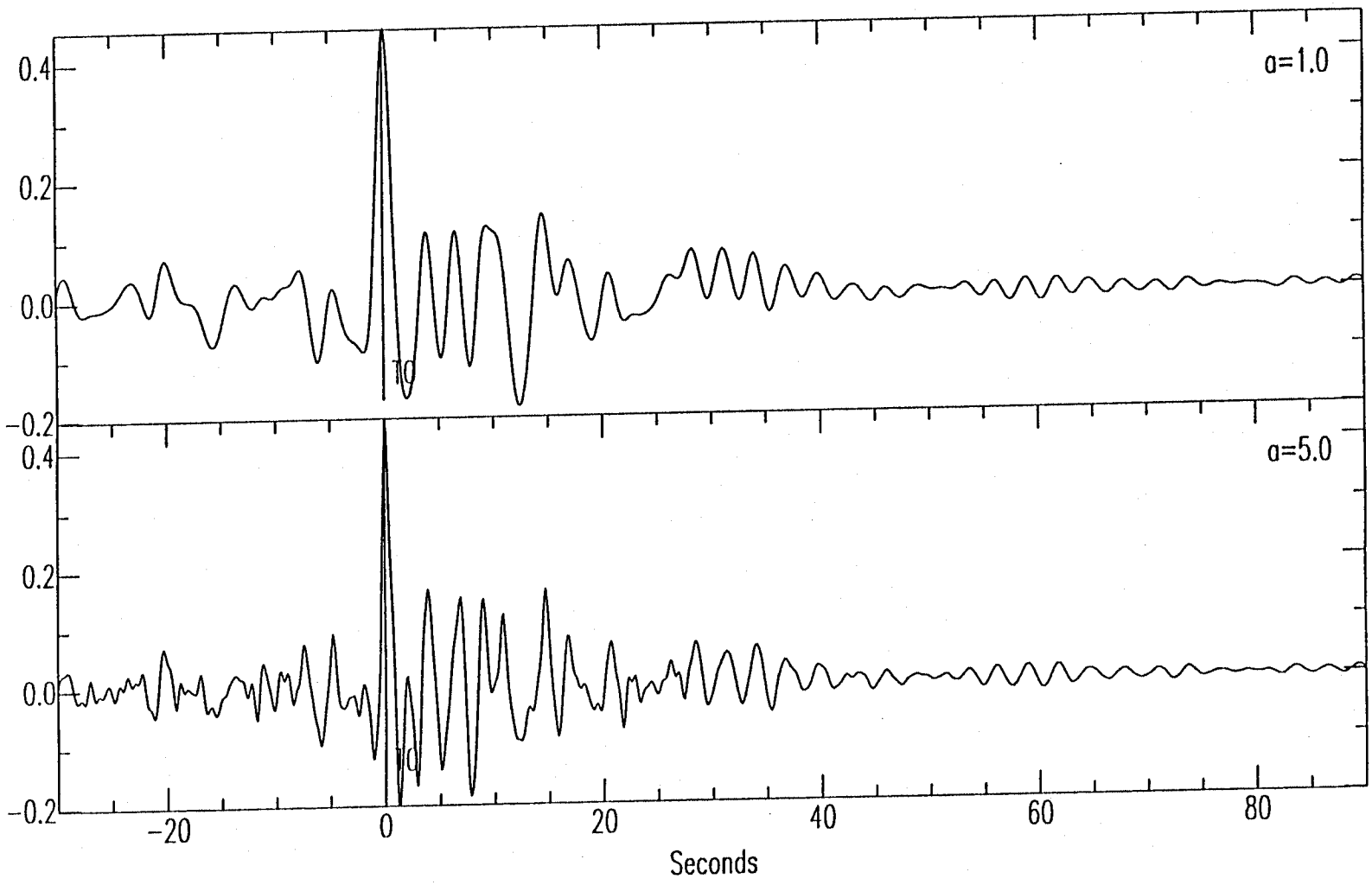

Figure 2.6. Two radial receiver functions obtained from deconvolving sample data using the same water–level parameter (c=0.01), but different Gaussian filter widths of a=1.0 (top), and a=5.0 (bottom).

$$D_R(\omega) = R_0 \sum_{k=0}^{n} \hat{R}_k \, e^{-i\omega t_k} \tag{12}$$

and

$$D_Z(\omega) = Z_0 \sum_{k=0}^{n} \hat{Z}_k \, e^{-i\omega t_k} \tag{13}$$

where,

$$\hat{Z}_k = \frac{Z_k}{Z_0} \quad \text{and} \quad \hat{R}_k = \frac{R_k}{R_0} \tag{14}$$

Z_k and R_k represent the amplitude of the k^{th} arrival normalized by the amplitude of the direct P wave. The simple problem with 3 arrivals can thus be written

$$D_R(\omega) = R_0\left[1 + \hat{R}_p e^{-i\omega t_p} + \hat{R}_s e^{-i\omega t_s}\right] \tag{15}$$

and

$$D_Z(\omega) = Z_0\left[1 + \hat{Z}_p e^{-i\omega t_p} + \hat{Z}_s e^{-i\omega t_s}\right] \tag{16}$$

where the subscripts p and s refer to P and S wave arrivals.

As mentioned above in the properties of the teleseismic P wave, the steep angle of incidence means that the P waves will be primarily recorded on the vertical component of displacement and the S waves on the horizontal. Therefore, the shear energy from the P−to−S conversion will be negligible on the vertical component. Also, in plane layered media, the arrivals generated by the plane P wave will have the same horizontal slowness. These two conditions can be expressed as

$$\hat{Z}_s \ll 1 \quad \text{and} \quad \hat{R}_p = \hat{Z}_p \tag{17}$$

Using this information, equations (6), (15) and (16) can be combined to find that to first order in the amplitudes of the secondary waves

$$E_R(\omega) = \frac{R_0}{Z_0} \frac{1 + \hat{R}_s e^{-i\omega t_s} + 2\hat{Z}_p \cos(\omega t_p)}{1 + 2\hat{Z}_p \cos(\omega t_p)} \tag{18}$$

The denominator can be expanded with a truncation of the expansion

$$(1 + X)^{-1} = 1 - X + X^2 - X^3 + \ldots \tag{19}$$

leaving

$$E_R(\omega) = \frac{R_0}{Z_0} \left[1 + \hat{R}_s e^{-i\omega t_s}\right] \tag{20}$$

or in the time domain,

$$E_R(t) = \frac{R_0}{Z_0} \left[\delta(t) + \hat{R}_s \delta(t - t_s)\right] \tag{21}$$

From the above analysis, it can be seen, by comparing equations (15) and (20), that the radial receiver function is simply a scaled version of the the radial component of displacement with the P multiple removed (Figure 2.7). It is for this reason that receiver functions are referred to with terms like "arrival" and "multiple" which are used to describe actual seismograms. Early investigations (e.g. *Owens,* 1984) normalized all receiver functions to unit amplitude, but *Ammon* [1991] applied a simple modification to the original procedure of *Langston* [1979] that allows for an estimation of the true receiver function amplitude. Doing this requires that the deconvolution of the vertical component from itself, using the same water–level parameter as in the horizontal component equalizations, produce a time series with a maximum amplitude of one. In practice, this is done by deconvolving the vertical component from itself and dividing the horizontal receiver functions by the maximum amplitude of the "vertical"

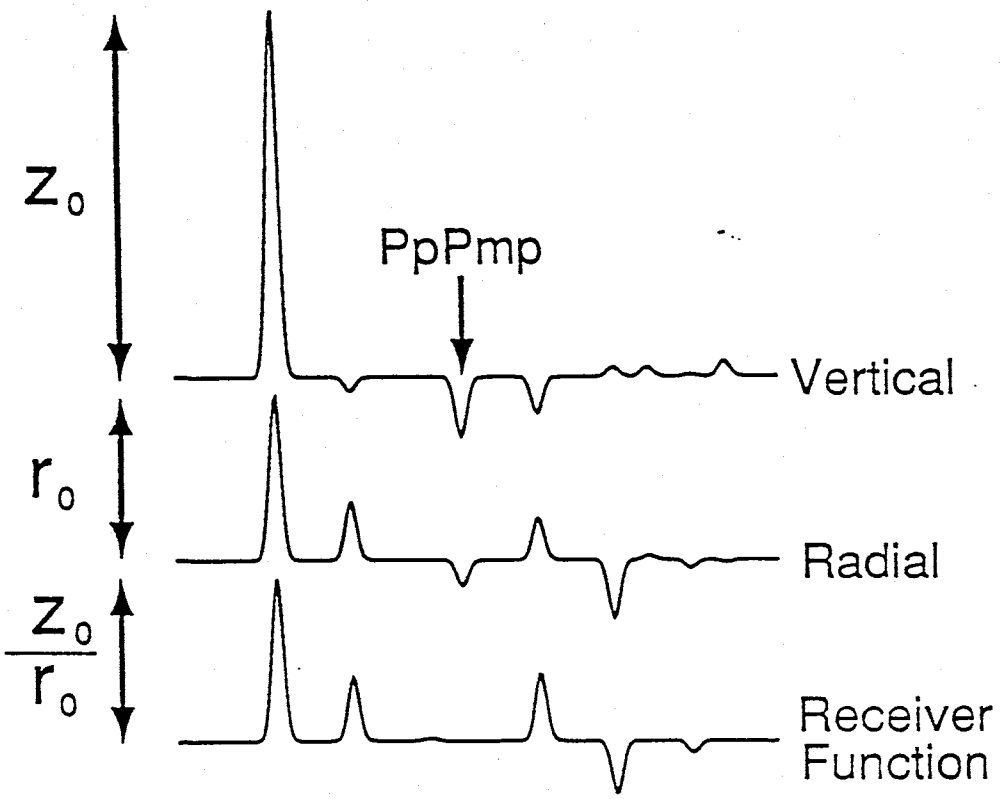

Figure 2.7. Vertical and radial response and the receiver function calculated for a single layer above a half–space. The amplitude relationship between the synthetic response and the receiver function is indicated to the left of the traces [from *Ammon,* 1991].

deconvolution [*Ammon*, 1991]. This provides information on the ratio R_0/Z_0 which is dependent on the near−surface velocity. Such information is useful when modeling receiver functions.

Stacking and Modeling Radial Receiver Functions

The deconvolution process produces radial receiver functions that are quite similar for events that have different source functions (Figure 2.8). However, receiver functions from considerably different backazimuths can vary significantly, depending on the degree of lateral heterogeneity under the station. In order to estimate the mean receiver function for each backazimuth, events that cluster in both distance and backazimuth are stacked. The vertical velocity structure can be modeled for each individual stack by modeling the one dimensional velocity response with standard propagator matrix synthetic seismograms [*Kennett*, 1986]. Once a velocity structure has been obtained for each stack, differences in the structures as a function of backazimuth can be used to discern gross lateral heterogeneities.

Inverting Radial Receiver Functions

To automate the modeling procedure, *Ammon et al.* [1990] present a linearized time−domain waveform inversion scheme based upon the inversion method of *Owens et al.* [1984]. The objective is to obtain a simplified model of the subsurface structure from the information contained in the first 20−30 seconds of stacked radial receiver functions (the details for the inversion technique can be found in *Ammon et al.*, 1990). One aspect of the inversion procedure is the implementation of a smoothness constraint that minimizes a roughness norm in the inversions. This became necessary because solutions often had rapid variations in the velocity structure with depth due to an underdamping of the inversion. The smoothness parameter limits the number of free parameters in the inversion, thus controlling the trade−off between waveform fit and model smoothness. Figures 2.9 an 2.10 illustrate this trade−off. Synthetic receiver functions were used as data and 12 inversions with different smoothness constraints were used to

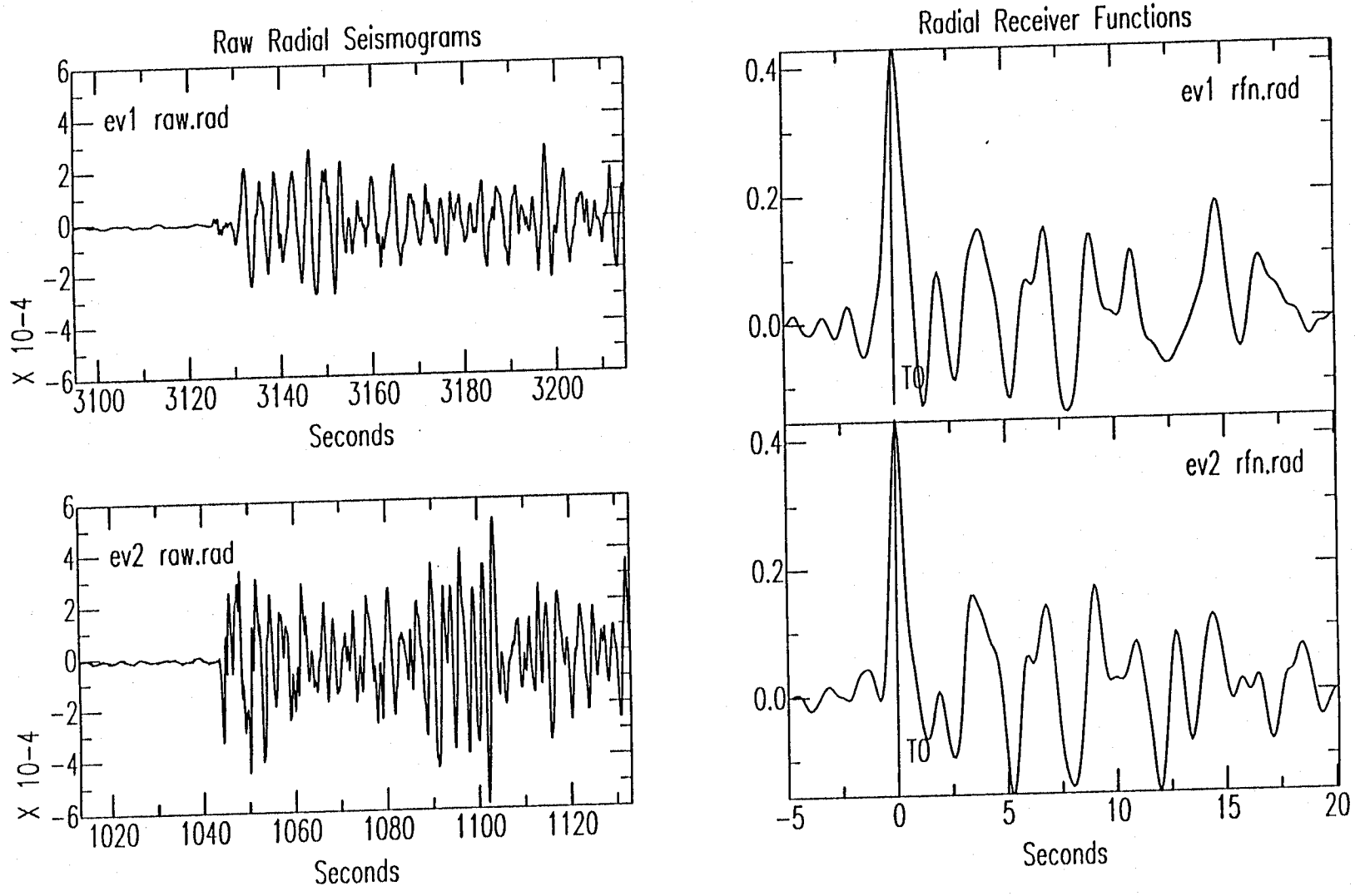

Figure 2.8. (Left) Raw radial seismograms (120 seconds each) for two events with similar distances and backazimuths from the recording station, but different source functions. (Right) The first 20 seconds of the radial receiver functions corresponding to the events on the left. Note the similarity of the receiver functions.

match these "data". Figure 2.9 shows the suite of inversions to illustrate how increasing the smoothness constraint eventually eliminates rapid variations over small depth intervals, such as the thin low velocity layer near 20 km depth. Note, however, that the more gradual velocity increase at the crust–mantle boundary region is much less affected by increasing smoothness. This is apparent in Figure 2.10, which shows the structures obtained using the two extreme smoothness parameters., Note how the arrival immediately following the direct P (a P–to–S conversion off of the crust–mantle transition region) is preserved in both cases, but the conversions and multiples caused by the thin low velocity zone are eliminated and the overall waveform fit to the data is degraded.

Upon testing the inversion routines with synthetic data, *Ammon et al.* [1990] found a trade–off exists between the average shear wave velocity above the perturbation and the depth to the perturbation. This nonuniqueness arises from the fact that the receiver function is sensitive to arrival times from converted phases relative to the arrival time of the direct P wave, but not to the absolute velocity of the model. Figures 2.11 shows a velocity model and its corresponding synthetic receiver function. Using 48 initial models (obtained by slightly perturbing a given starting model), 48 inversions were performed in an attempt to match the synthetic "data". Figure 2.12 shows the results, which have been grouped into three families with different average upper crustal velocities. Note how the thin low velocity zone near 20 km changes depth in the three families to maintain a constant travel time for a conversion off of the discontinuity. The LVZ deepens as the average velocity above the LVZ increases, so that the total travel–time remains constant. The synthetic receiver functions from the 48 models all fit the data to the degree required by the inversion routines. To help constrain this nonuniqueness problem, *Ammon et al.* [1990] developed a routine that generates a number of starting models (usually 24) by slightly perturbing the original initial model. In most cases, each inversion will produce an acceptable fit to the data within three or four iterations. The inversion results can usually be placed into three or four "families" of solutions like those shown in Figure 2.12.

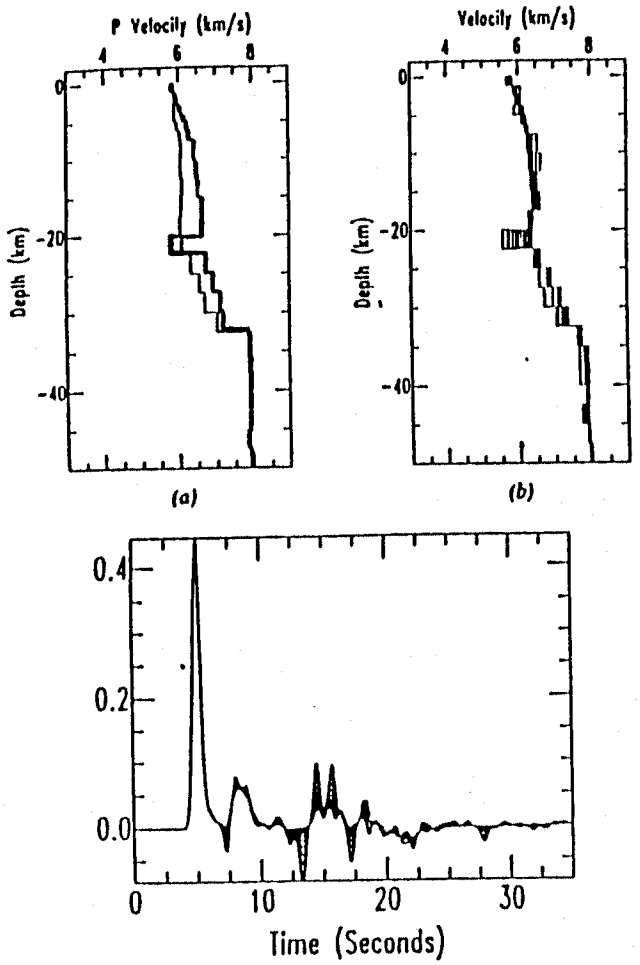

Figure 2.9. (a) The "true" solution (thick line) and the starting model (thin line) for 12 inversions performed with different levels of smoothness constraint. (b) The resulting velocity models after three iterations for the inversion suite. Note the gradual elimination of the low–velocity perturbation in the resulting models as the model smoothness increases. (c) The "true" waveform and the waveforms corresponding to the models shown in Figure 2.9b [from *Ammon and Zandt*, 1990].

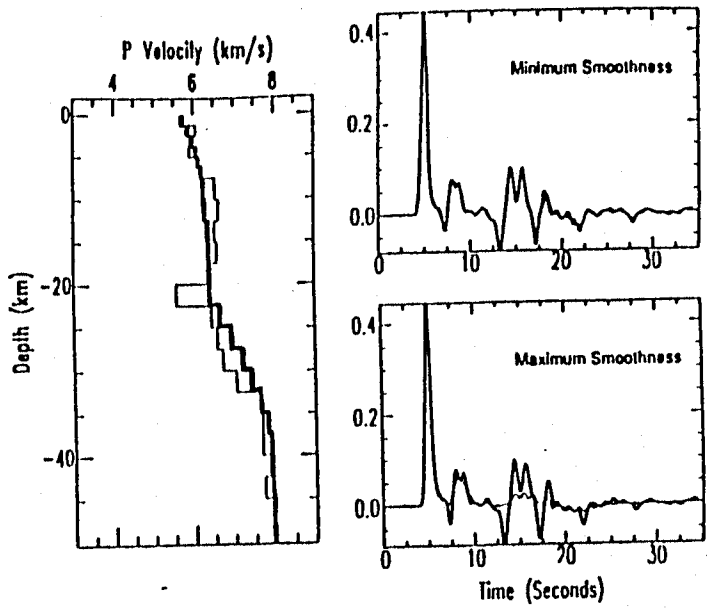

Figure 2.10. Velocity models (left) and receiver function matches (right) for the extreme roughness models resulting from the inversion sweep with a varying smoothness parameter. The smooth velocity model is identified by the thick line, the rough velocity model is identified by the thin line. In the receiver function diagrams, the the thick line identifies the waveform inverted during the tests, and the thin lines identify the receiver functions corresponding to the models shown on the left [from *Ammon and Zandt*, 1990].

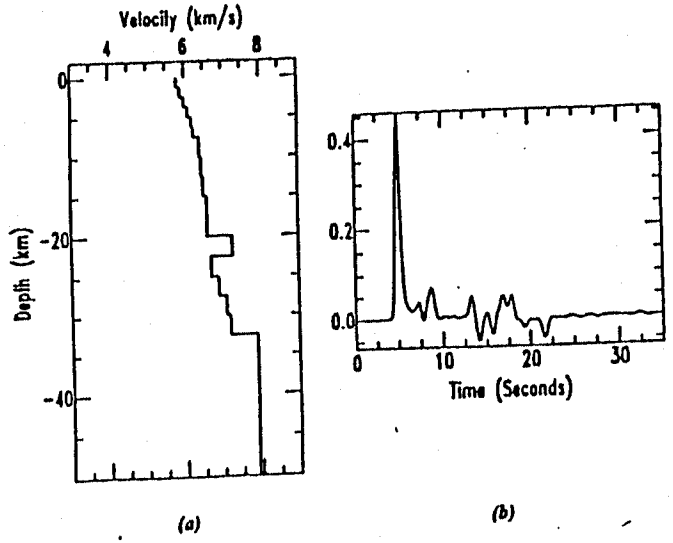

Figure 2.11. (a) P velocity profile of the "true" model used in the synthetic inversion test. (b) The receiver function corresponding to the velocity structure of Figure 2.11a. The incident P wave had a ray parameter of 0.06 s/km, which corresponds to a surface source at approximately 60° distance [from *Ammon and Zandt*, 1990].

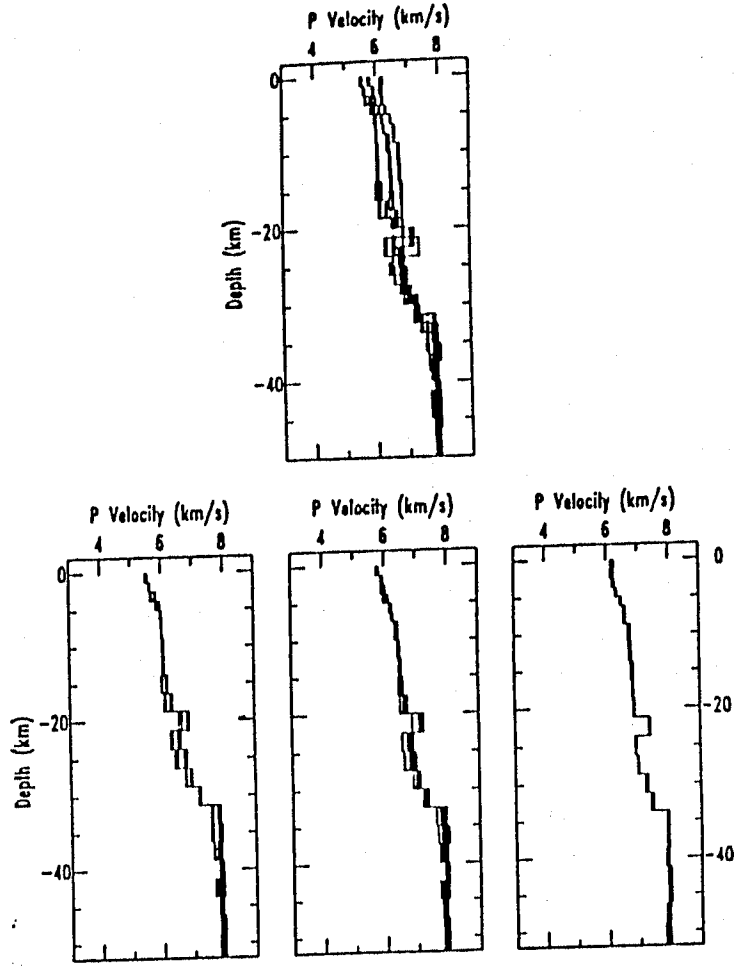

Figure 2.12. (Top) The acceptable solution models obtained from the 48 inversions of the waveform presented in Figure 2.11. (Bottom) Separation of the models into groups based on average upper crustal velocity [from *Ammon and Zandt*, 1990].

It then becomes necessary to have some information from previous investigations (e.g. reflection or refraction profiles of the upper crust) that can be used to eliminate those solutions that do not fit the *a priori* constraints.

Implementation of Methods for this Study

For this study, I used routines developed by *Ammon* [1991] to perform the deconvolutions. Using the deconvolution procedure described above, these codes perform a suite of deconvolutions using numerous combinations of Gaussian filter widths and water–level parameters. Details concerning the use of these codes can be found in Appendix C. Once obtained, the receiver functions were used both as a target for forward modeling using synthetic seismograms obtained from standard propagator matrix techniques [*Kennett*, 1986], and as data to invert, using the latest techniques of *Ammon et al.* [1991] mentioned above. Instructions on the use of the forward modeling and inversion codes can be found in Appendix C.

3. DATA

Teleseismic Earthquake Data

The teleseismic events used for this study were recorded by three intermediate period seismometers (Kinemetrics SV−1 and SH−1's) at station WTX in Socorro, NM (Figure 1.1). A Refraction Technologies Inc. (Reftek) recorder, operating in continuous mode, was used to record the data at 20 samples per second. This instrumentation was effective for recording signals with frequency ranges typical of teleseismic earthquakes (0.1−2.0 Hz). Since the station began operation in April 1990 I have collected well recorded teleseismic waveforms (i.e. those with a high S/N) from events with epicentral ranges of 30° to 90°. This distance range is used to ensure a steep angle of incidence (> 30°) and to avoid core phases that can complicate interpretation (< 90°) [*Langston*,1979]. In most cases, events with a body−wave magnitude of 5.8 or greater are necessary to provide high−quality waveforms, although occasionally, events with magnitudes of 5.6 or 5.7 can also provide suitable waveforms.

Table 3.1 lists the fourteen events used for this study. The raw vertical, radial and tangential traces can be found in Appendix A (pages noted in the first column of Table 3.1). These events form four groups that cluster in both backazimuth and distance from station WTX (see Figure 3.1). The clusters consist of four events to the northwest (Aleutian Island region), three events to the south (Canary Island region), and two clusters of events to the southeast (Chile−Argentina). Cluster 1 consists of three events and cluster 2 consists of four events. The data from the southeast have been divided into two clusters because of the wide range of distances. As shown in Figure 3.1, the azimuthal distribution of events is far from complete. Nearly 180° of azimuthal coverage from the northwest cluster clockwise to the southeast clusters is unrepresented in this study. Although smaller, another gap in the azimuthal distribution is to the west−southwest. Most earthquakes from these backazimuths occur beyond the distance limit

Table 3.1. Teleseismic Event Parameters[a]

Event / page[b]	Date yy/mm/dd	Latitude (deg)	Longitude (deg)	M_b	Depth (km)	Δ (deg)	Baz (deg)
Southeast data *Cluster 1*							
15090 / A3	90/05/30	6.0 S	77.2 W	6.1	24	48.8	139.2
32790 / A4	90/11/23	4.7 N	75.6 W	5.7	145	41.2	128.2
09591 / A5	91/04/05	6.0 S	77.1 W	6.5	20	48.8	138.8
Cluster 2							
28390 / A6	90/10/10	19.5 S	66.6 W	5.8	266	65.5	137.8
14491 / A7	91/05/24	16.5 S	70.7 W	6.3	128	60.9	139.7
17491 / A8	91/06/23	26.8 S	63.3 W	6.4	558	73.3	140.1
18791 / A9	91/07/06	13.1 S	72.2 W	6.2	105	57.5	139.3
South data							
23390 / A11	90/08/21	27.5 S	104.3 W	6.0	11	61.4	177.2
24691a / A12	91/09/03	17.9 S	116.0 W	6.0	9	52.4	191.1
24691b / A13	91/09/03	17.9 S	116.0 W	5.8	11	52.3	190.9
Northwest data							
32590 / A15	90/11/21	51.6 N	171.3 W	5.8	33	48.7	311.5
05291 / A16	91/02/21	58.4 N	175.4 W	6.2	20	50.6	320.7
06791 / A17	91/03/08	60.9 N	167.0 E	6.4	13	59.0	325.2
15091 / A18	91/05/30	54.6 N	161.6 W	6.3	28	42.8	315.6

[a] Individual event parameter information taken from the U.S. Geological Survey Preliminary Determination of Epicenter Listings.

[b] Page of Appendix A on which event seismograms can be found.

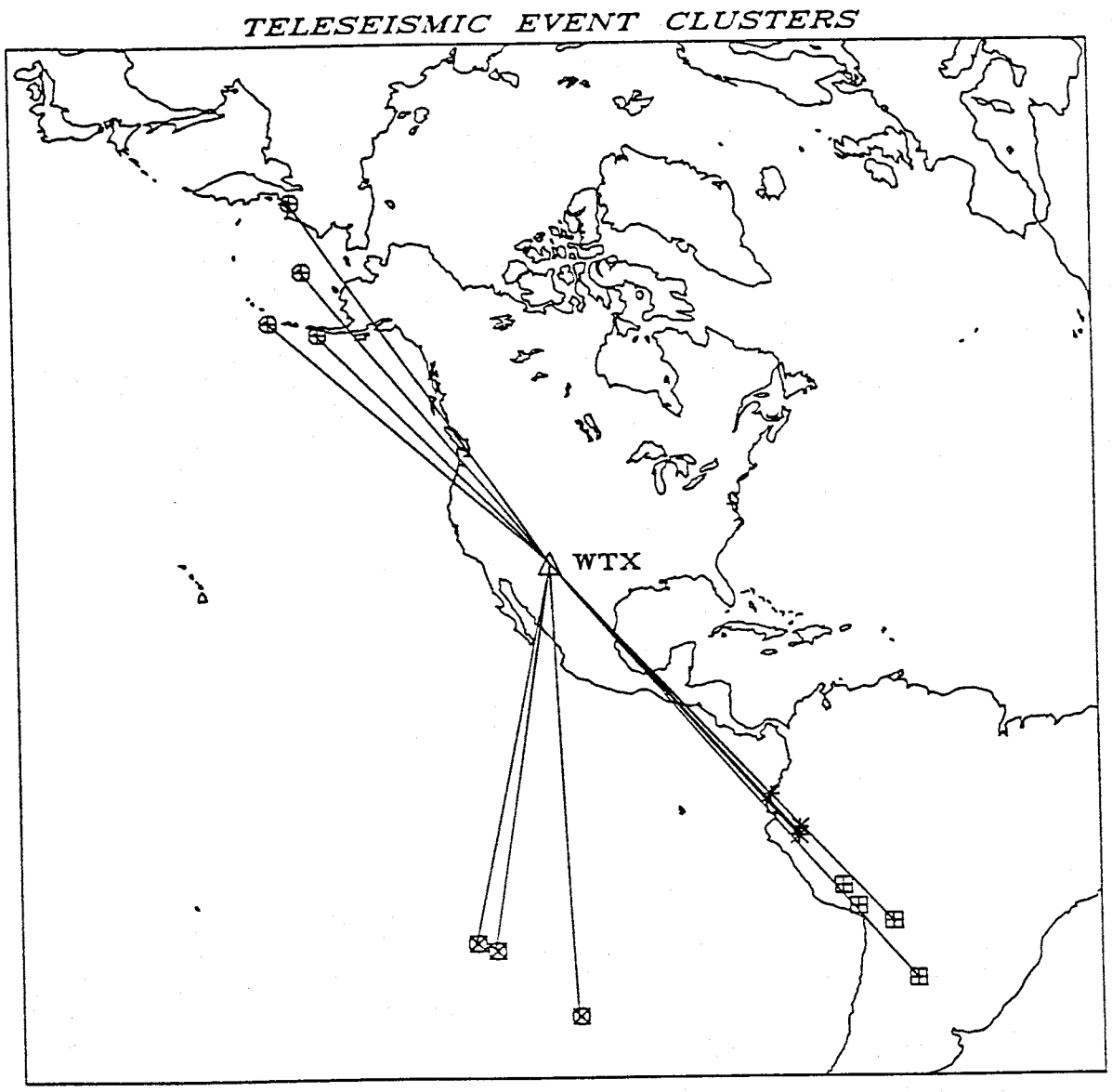

Figure 3.1. Map showing the locations of the four events in the northwest cluster, the three events in the south cluster and the two groups of three and four events in the southeast cluster. Map projection is azimuthal; dark lines represent great circle paths from the events to station WTX.

discussed above, and the signal–to–noise ratio is often poor. While a few high–quality events from these azimuthal gaps have been recorded, they are scattered in distance and backazimuth and do not form event clusters.

Receiver Functions

A source equalization was performed using the first 40 seconds of data following the direct P–wave arrival for all events in Table 3.1 using the deconvolution programs described in Appendix C. Ultimately, only 20 seconds of each receiver function will be inverted, but 40 seconds of the P–waveform is deconvolved so that any effects of truncating the time series prior to deconvolution will be outside the 20 second window. In each case, a Gaussian filter width of 2.5 and the smallest water–level parameter that produced a stable deconvolution were used in the source equalization process. For this data set, the value of 2.5 for the Gaussian filter width was found to be the optimum value for reducing the very high frequency noise while preserving enough of the short period content of the waveform to perform detailed modeling. Because the instruments at station WTX are not matched, a technique described by *Zandt* [personal communication, 1991] was used to normalize the instrument response so that the effects of the instruments would be removed in the deconvolution (see Appendix C for the normalization technique). The resulting radial and tangential receiver functions for each event can be found in Appendix B. Because the two event clusters from the southeast produced strikingly similar radial receiver functions despite the distance range, the two clusters were merged to form one large event cluster from the southeast. Figures 3.2, 3.3, and 3.4 show the stacked radial (top) and tangential (bottom) receiver functions (± 1 standard deviation) for the southeast, south and northwest data clusters respectively. Two features of this data set are immediately apparent. First, the stacked radial receiver functions are considerably different for each backazimuth, indicating some degree of azimuthal heterogeneity. Secondly, it is clear that coherent tangential energy exists for all three

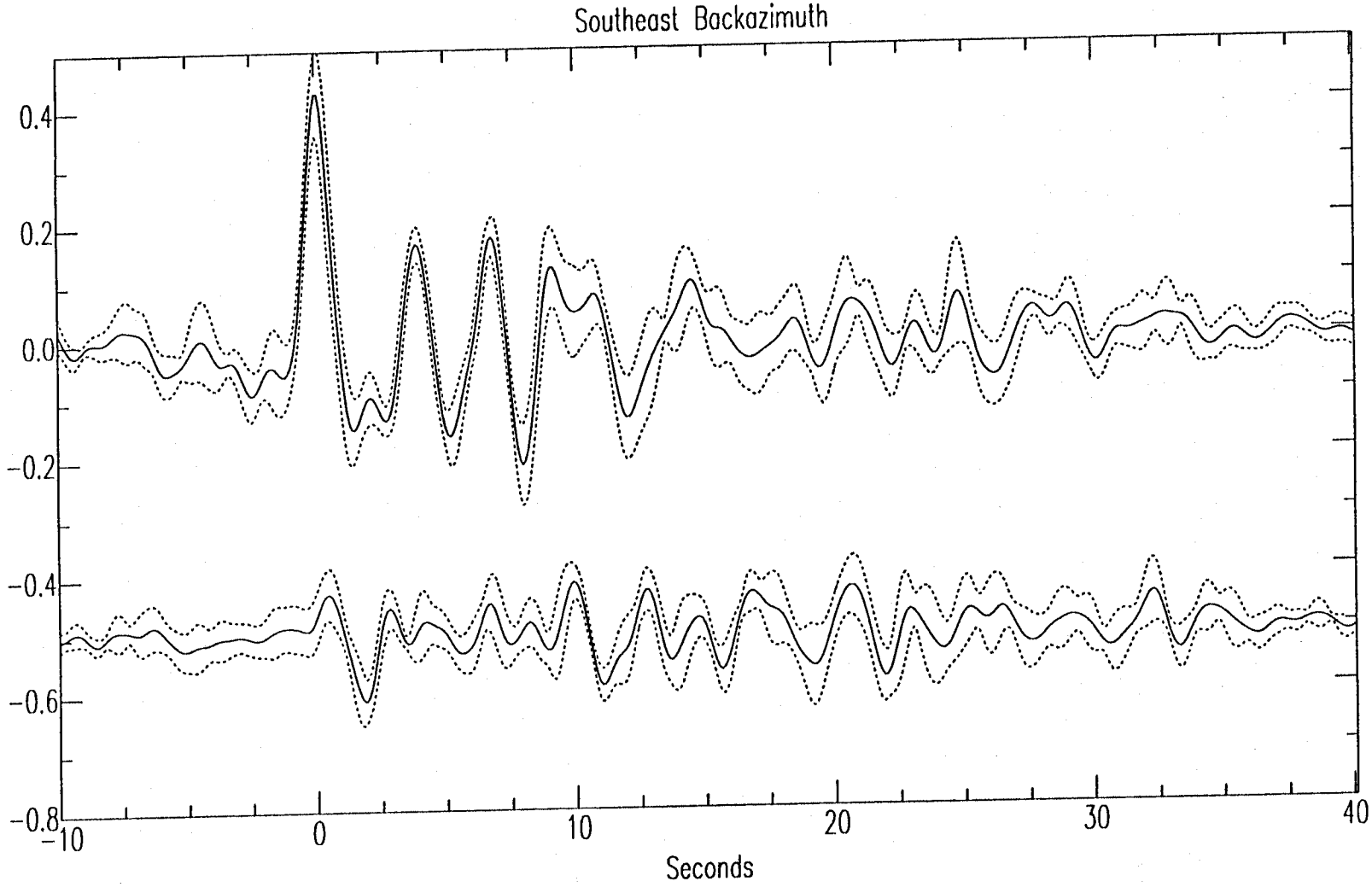

Figure 3.2. Stacked radial (top) and tangential (bottom) receiver functions (solid lines) ±1 standard deviation (dotted lines) for the southeast event cluster.

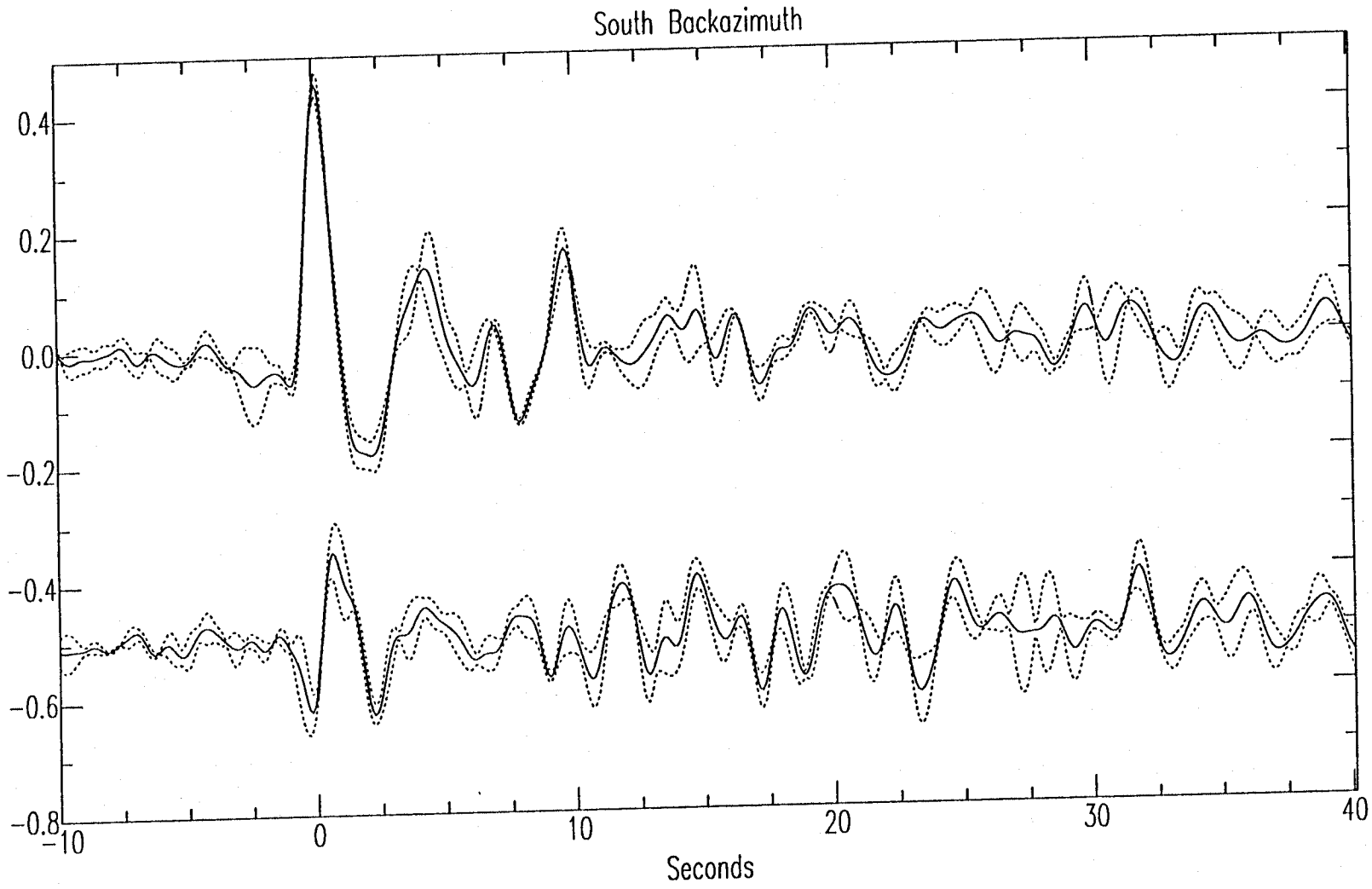

Figure 3.3. Stacked radial (top) and tangential (bottom) receiver functions (solid lines) ± 1 standard deviation (dotted lines) for the south event cluster.

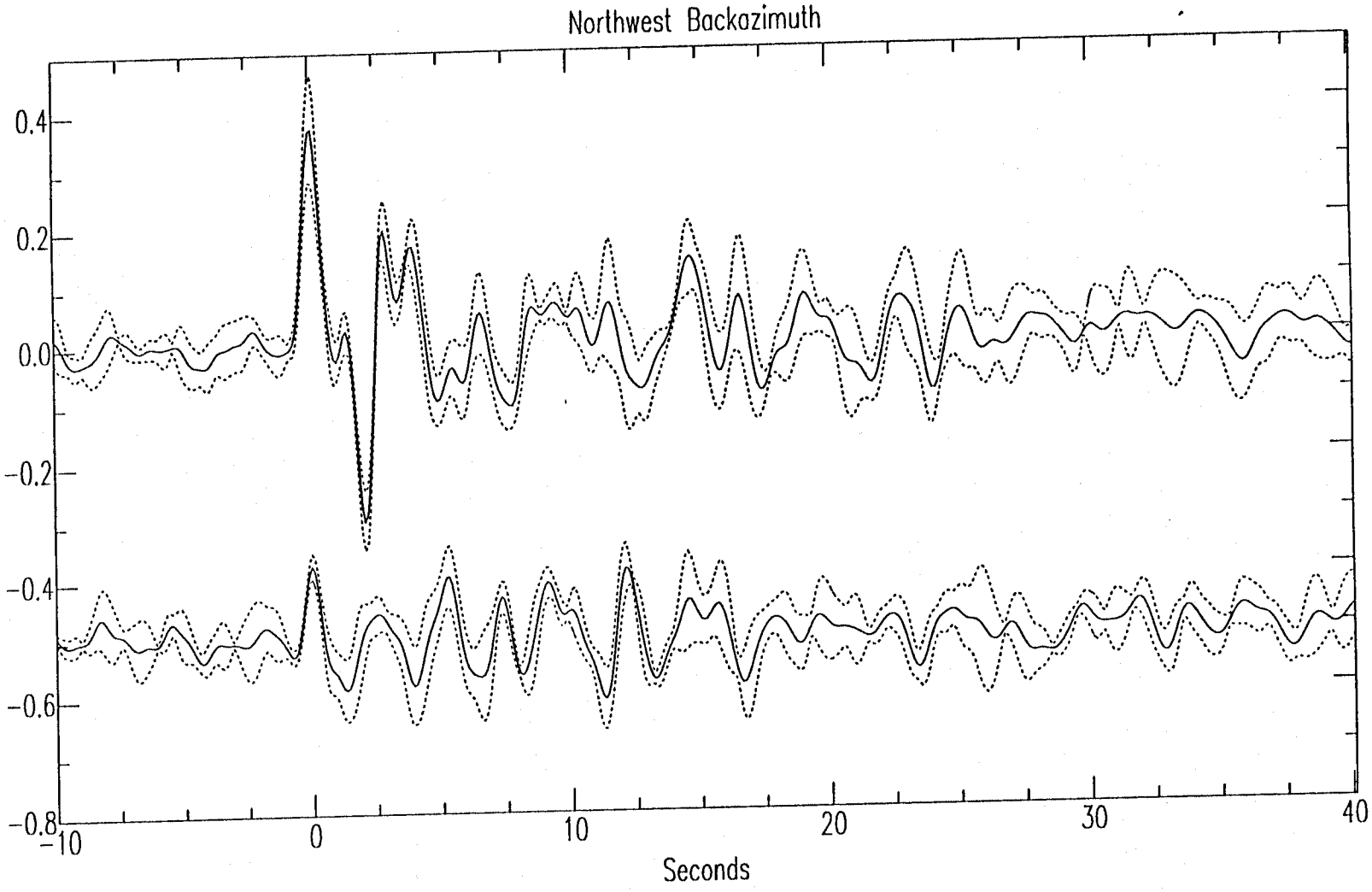

Figure 3.4. Stacked radial (top) and tangential (bottom) receiver functions (solid lines) ±1 standard deviation (dotted lines) for the northwest event cluster.

backazimuths. Theoretically impossible in a vertically stratified, laterally homogeneous crust, the existence of tangential energy violates the assumption that the receiver functions are dominated by the response of homogeneous, horizontal layers. *Langston* [1977b] studied the effects of a planar dipping structure on receiver functions, but determining strike directions and dip angles requires an extensive data set with nearly complete azimuthal coverage so that a statistical analysis of the coherence between radial and tangential arrivals as a function of ray parameter can be perfomed. In this study, the number of events in each cluster is small, and the azimuthal coverage is limited, so any interpretation of tangential arrivals is unwarranted. The existence of tangential energies is thus noted, but the modeling results of the following sections are based on a horizontally stratified, laterally homogeneous earth model.

4. RESULTS AND DISCUSSION

The first 20 seconds of the stacked radial receiver functions shown in Figures 3.2, 3.3 and 3.4 were inverted for structure using the inversion scheme of *Ammon and Zandt* [1990] described in Chapter 2. The length of data to invert (20 seconds) was chosen as that length which was both long enough to include conversions and multiples from deep interfaces, but short enough that the arrivals on the individual receiver functions within the stack were still relatively coherent. The initial model used for the inversions is shown in Figure 4.1. The upper–crustal velocities of the initial model correspond to the average upper–crustal velocities of the central RGR determined by *Hartse* [1991]. Included in the initial model is a thin (250 m) layer representing the mid–crustal magma body. The velocities and density (V_p = 3.25 km/sec ; V_s = 1.00 km/sec ; ρ = 2.60 g/cm^3) of this thin layer were obtained by averaging the multi–layered magma body values proposed by *Ake and Sanford* [1988]. The lower–crustal velocities correspond to the average velocities obtained by *Singer* [1989] from his time–term analysis of P_g and P_n phases. The layered model extends to a depth of 51 km, with layers 2 km thick for most of the first 35 km and layers 4 km thick from 35 km to 51 km (Table 4.1). As discussed in Chapter 2, the inversion scheme generates 24 different solutions that fit each data stack, and some *a priori* information is necessary to be able to identify "good" solutions and eliminate others. For this study, the average shear wave velocity (V_s = 3.41 km/s) obtained by *Hartse* [1991] for the top 10 km was used as a constraint. Only those solutions whose average shear wave velocity for the upper 10 km are within 0.20 km/s of the constraint were accepted. The lower–crustal shear–wave velocities of the initial model were not used as a constraint because they were derived from a compressional wave study with an assumed Poisson's ratio, whereas the upper–crustal shear wave velocities were solved for directly. In the following three sections, the results of inverting the stacked data, as well as forward modeling results are discussed for the data from each of the clusters. The last section discusses the features common to the solutions from all clusters

Table 4.1. Initial Model for Inversions

layers: 25
depth to half-space: 51 km

layer #	V_p (km/s)	V_s (km/s)	density (g/cm^3)	thickness (km)
1	5.95	3.41	2.70	0.50
2	5.95	3.41	2.70	0.50
3	5.95	3.41	2.70	1.00
4	5.95	3.41	2.70	2.00
5	5.95	3.41	2.70	2.00
6	5.95	3.41	2.70	2.00
7	5.95	3.41	2.70	2.00
8	5.80	3.44	2.75	2.00
9	5.80	3.44	2.75	2.00
10	5.80	3.44	2.75	2.00
11	5.80	3.44	2.75	2.75
12	3.25	1.00	2.60	0.25
13	6.40	3.65	2.90	2.00
14	6.40	3.65	2.90	2.00
15	6.40	3.65	2.90	2.00
16	6.40	3.65	2.90	2.00
17	6.40	3.65	2.90	2.00
18	6.40	3.65	2.90	2.00
19	6.40	3.65	2.90	2.00
20	8.10	4.35	3.30	2.00
21	8.10	4.35	3.30	4.00
22	8.10	4.35	3.30	4.00
23	8.10	4.35	3.30	4.00
24	8.10	4.35	3.30	4.00
25	8.10	4.35	3.30	∞

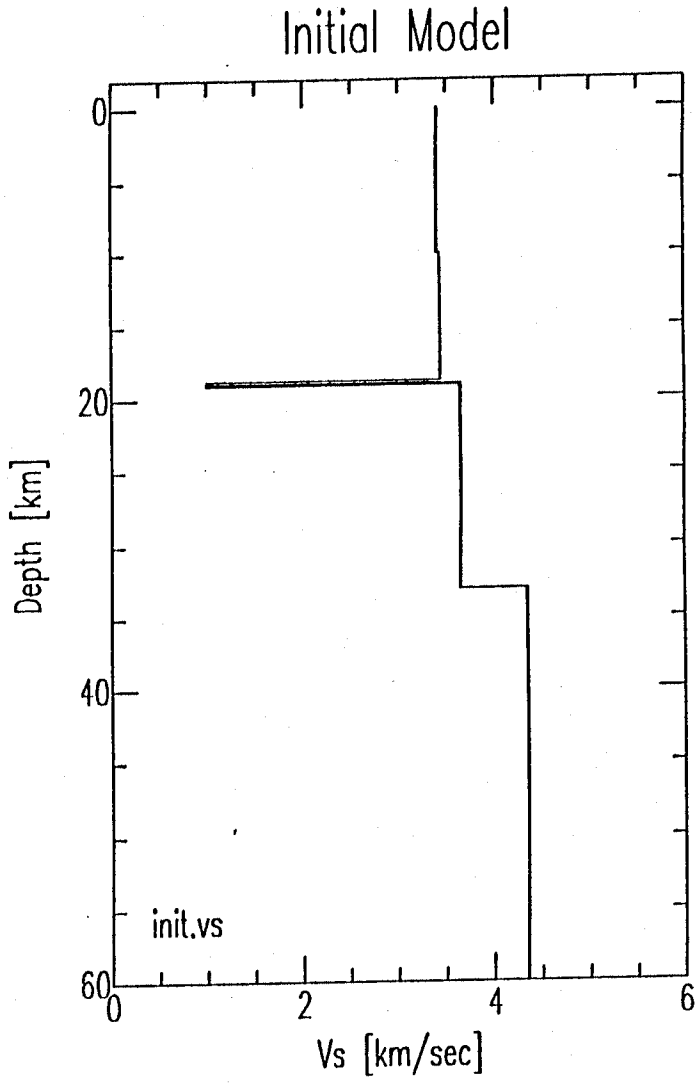

Figure 4.1. Shear wave velocity profile corresponding to the initial model in Table 4.1.

Southeast Data Cluster

The family of solutions that most closely fit the average upper–crustal velocity constraints is shown in Figure 4.2. The plot on the left shows the shear wave velocity profiles and the plot on the right compares the corresponding synthetic receiver functions with the data, where the number at the end of each filename is the correlation coefficient between the first 12 seconds of the synthetic receiver function and the data. Robust features of the solutions include a low–velocity layer near 7 km, a high velocity–layer near 11 km and another low velocity–layer near 20 km. The solutions also have rather slow ($V_s \approx 3.25$ km/sec) lower–crustal velocities down to a depth of 30 km. Between 30 km and 35 km there is a steady increase in velocities which appears to be a transitional crust–mantle boundary. Figure 4.3 displays the velocity models and the synthetic receiver functions with letters to indicate which features of the model cause which arrivals on the synthetic receiver functions. In the case where two features contribute to the same arrival (e.g. b and e for the arrival near 7 sec), the first letter corresponds to the feature that is most responsible for the arrival. Note the wide range of velocities represented by the family of solutions between the base of the high–velocity layer near 11 km (marked by the letter b) and the top of the low–velocity layer near 20 km (c). The inability to constrain the velocity in this region is reflected by the differing amplitudes of the arrivals marked b and c on the synthetic seismograms.

The low–velocity layer near 20 km (c) corresponds nicely to the depth of the Socorro magma body (Figure 1.8). Because of the smoothness constraint applied to the inversion, a thin layer of extremely low velocity will be expressed as a "smeared out" feature over a larger depth interval with a less extreme velocity contrast. Although the low–velocity layer (a) and the high–velocity layer (b) in the upper crust average together to maintain a close match to the velocity constraints, these features have not been detected by any previous geophysical investigations of the central RGR. However, the base of the high velocity layer near 11 km (c) marks a sharp decrease in velocity and may correspond to

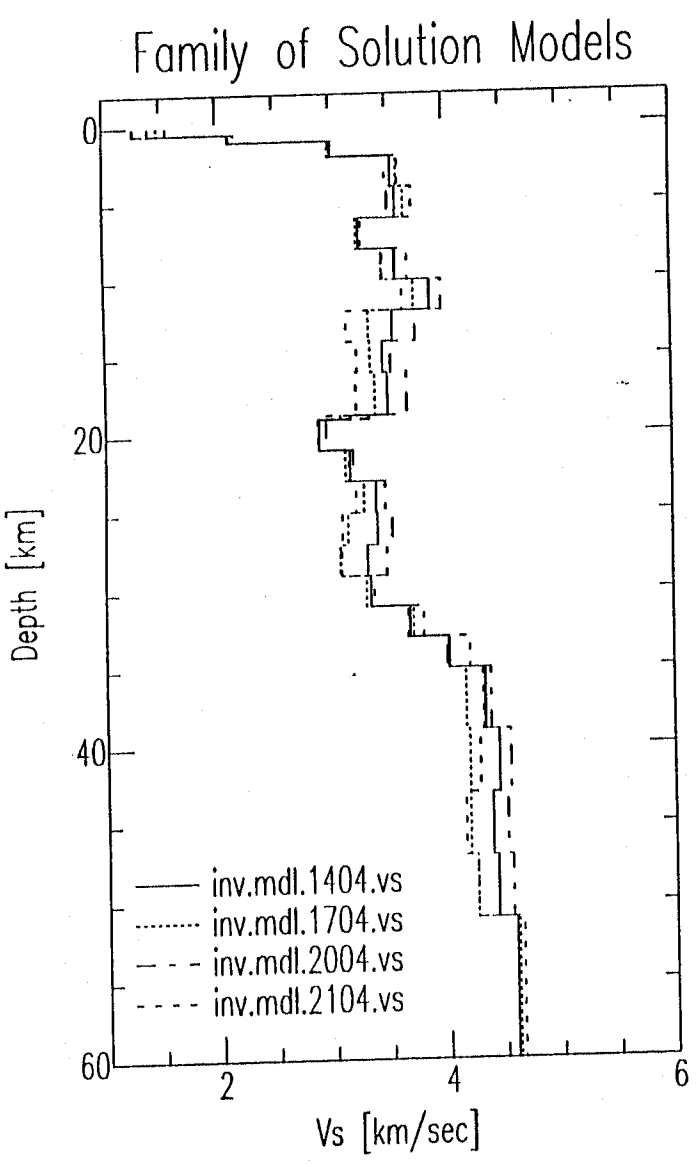

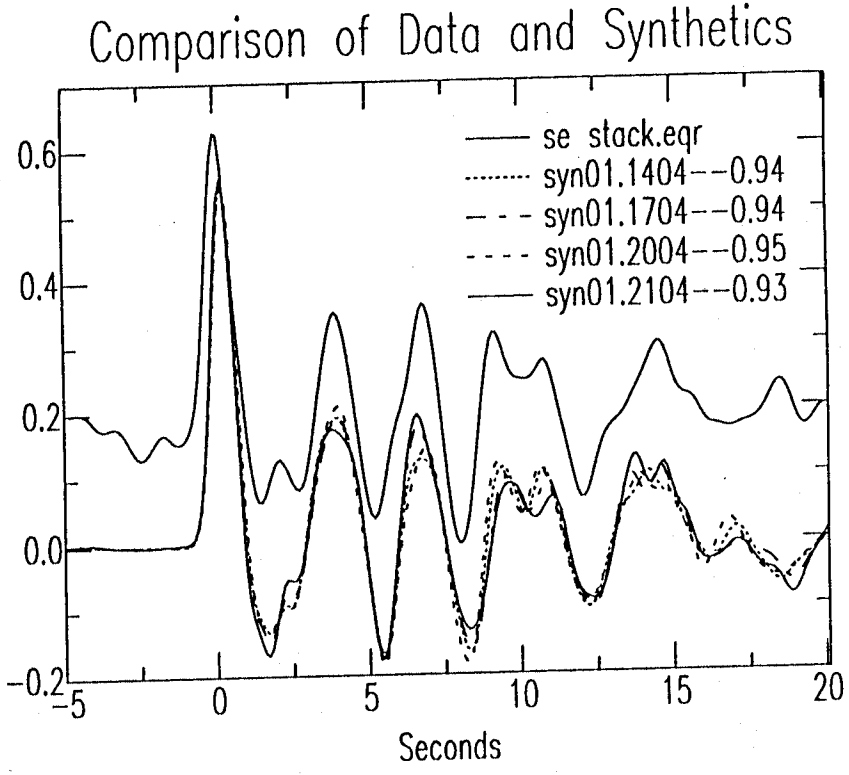

Figure 4.2. (Left) Family of solution models from the inversion of the southeast data. (Above) Comparison of the stacked receiver function (top trace) and the synthetic receiver functions corresponding to the models on the left (overlain below data). The number following the synthetic labels is the correlation coefficient between the data and the first 12 seconds of the synthetic.

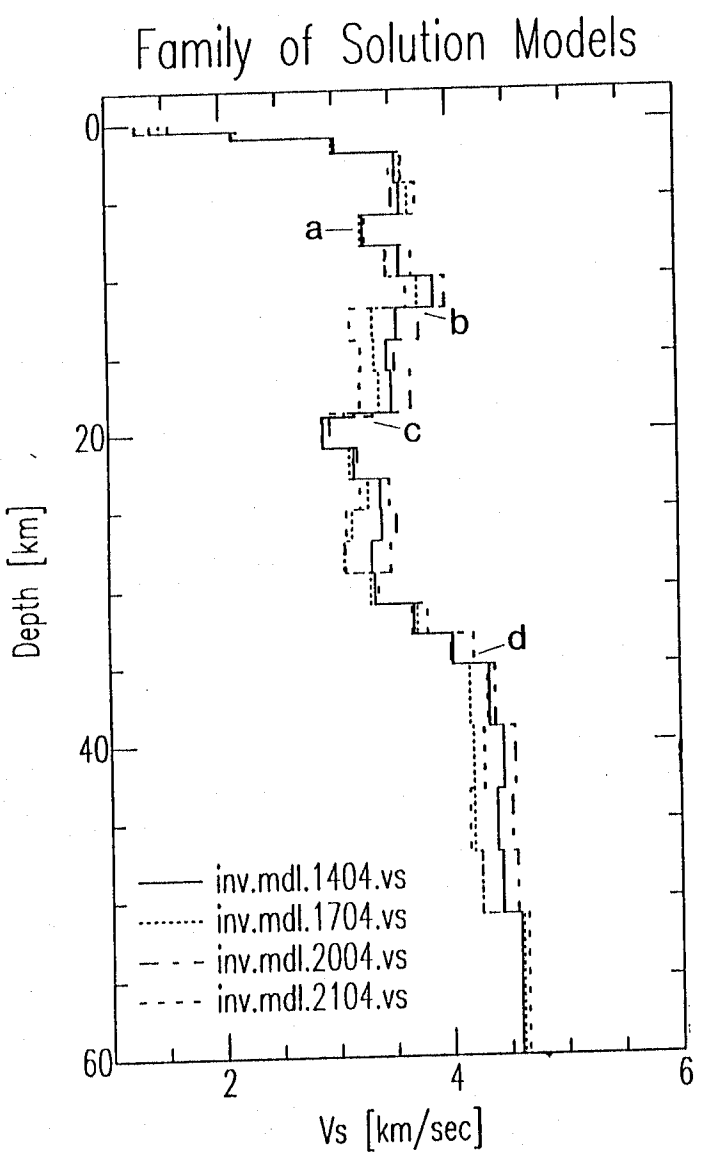

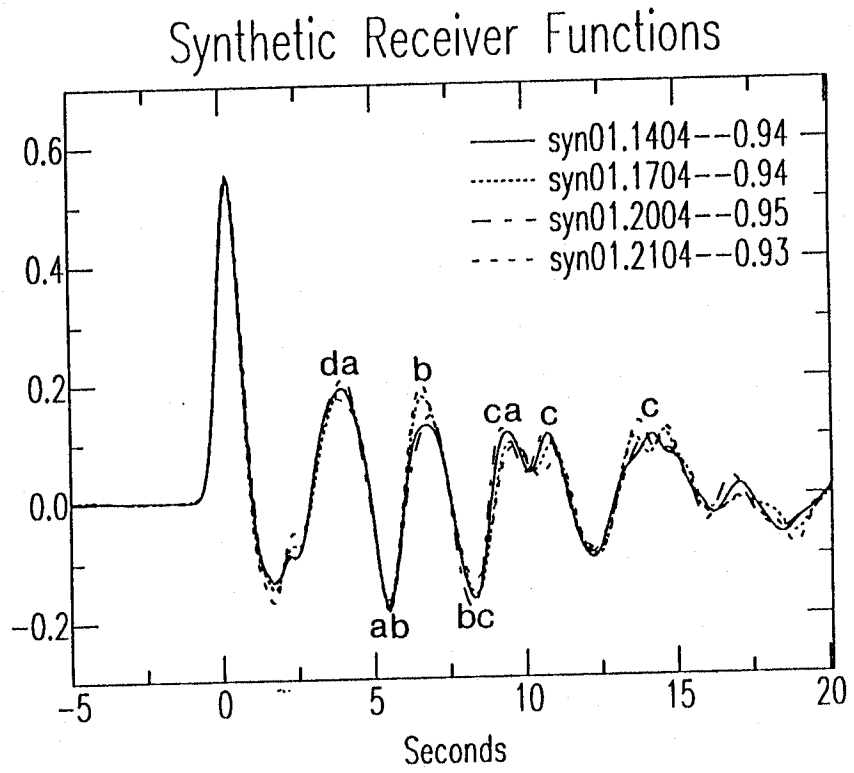

Figure 4.3. (Left) Family of solution models from the inversion of the southeast data. (Above) Overlay of synthetic receiver functions corresponding to the models on the left. Lower case letters are used to associate arrivals on the synthetics with robust features on the solution models.

the base of the seismogenic zone at 12 km depth where there is believed to be a transition from the brittle seismic region to a ductile aseismic zone. [*Hartse*, 1991].

Figure 4.4 shows one of the inversion solutions with the complicated upper crustal structure removed (left), and the resulting fit between the corresponding synthetic receiver function and the data (right). It is clear that for the given family of solutions, the complicated upper crustal structure is essential for a reasonable fit to the data, indicating that perhaps the upper crustal features (a and b in Figure 4.3) represent a complicated structure that is localized to the vicinity station WTX and is thus undetected by the larger–scale central RGR studies [e.g. *Hartse*, 1991; *Singer*, 1989; *Schlue et al.*, 1986]. However, another plausible explanation can be provided by the nonuniquness property of the inversion process. It may be possible to remove the upper crustal structure and introduce more structure into the lower crust and upper mantle to regain a good fit to the data, although none of the 24 solutions for the inversion were able to do so without sacrificing a close match to the upper–crustal velocity constraints.

South Data Cluster

The family of solutions for the south cluster is shown in Figure 4.5. The solutions contain a broad low–velocity zone between 16 and 19 km, but are otherwise have a much less complicated structure than the results from the southeast. The shear wave velocities increase rather uniformly from the base of the low–velocity zone to 35 km, which appears to mark the crust–mantle interface. Like the southeast solutions, the shear–wave velocities remain quite slow (< 3.5 km/s) to a depth of 30 km. Figure 4.6 displays the solutions with letters to match the synthetic receiver function arrivals with velocity model features (cf. Figure 4.3). The arrival near 7 seconds is predominantly created by the drop in velocity

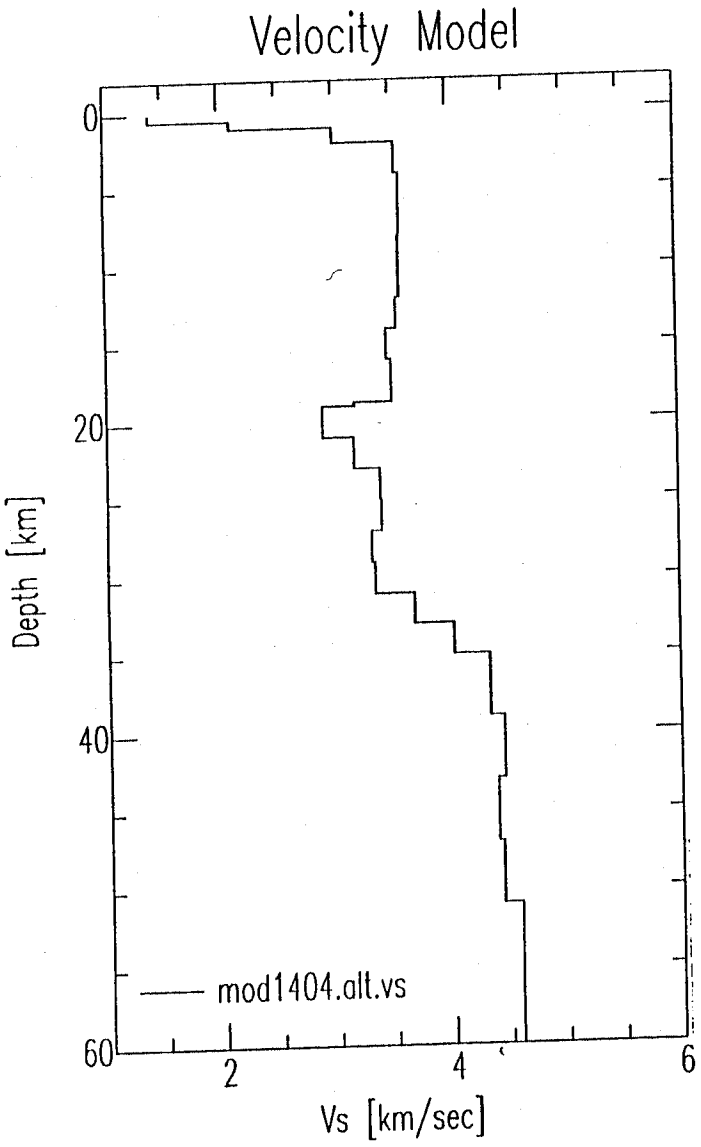

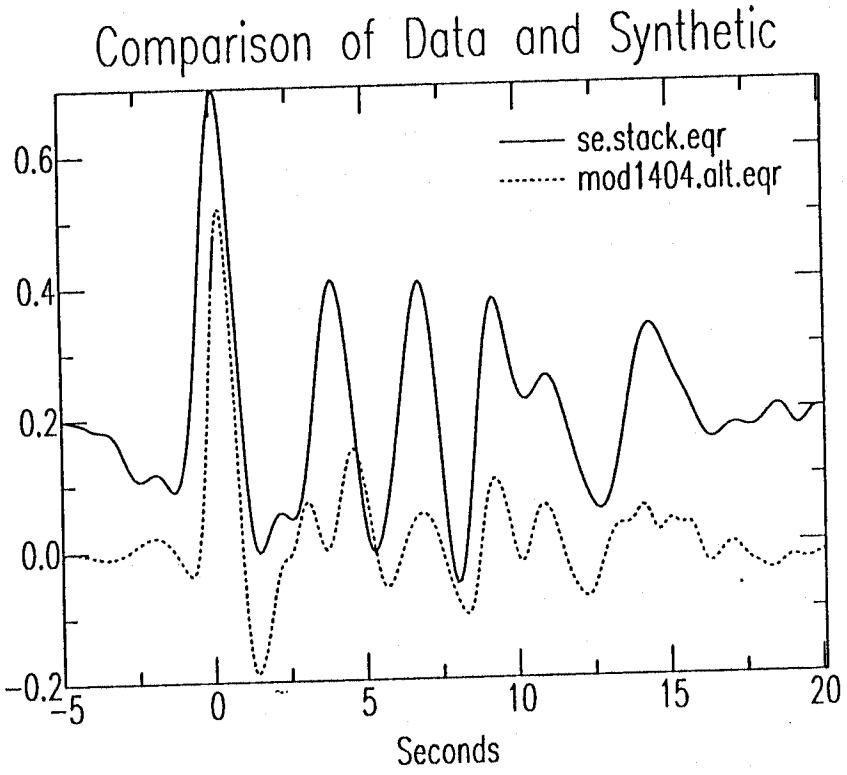

Figure 4.4. (Left) One of the southeast solution models from Figure 4.3 (model 1404) with features **a** and **b** removed from the upper crust. (Above) Comparison of the data and the synthetic receiver function corresponding to the model on the left.

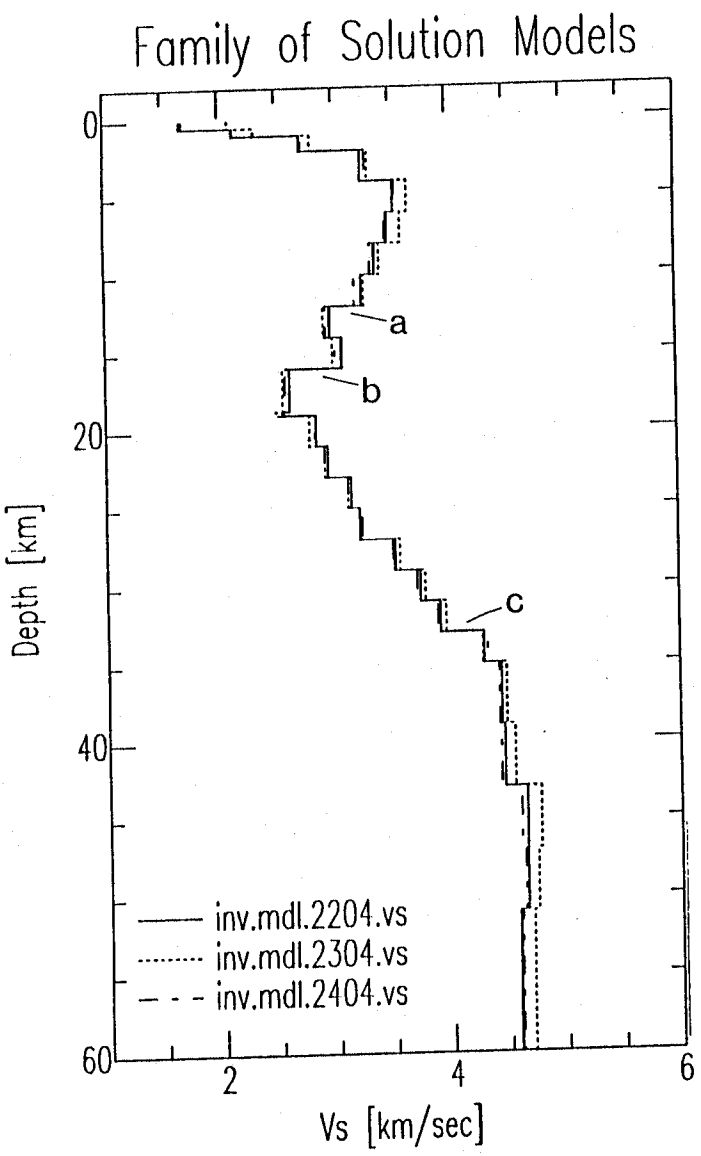

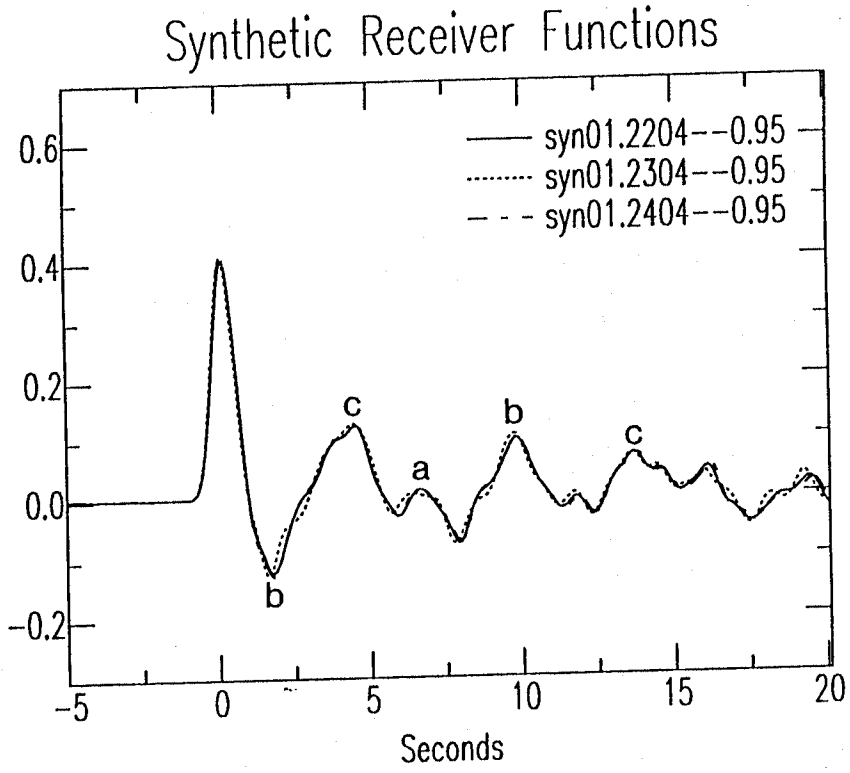

Figure 4.6. (Left) Family of solution models from the inversion of the south data. (Above) Overlay of synthetic receiver functions corresponding to the models on the left. Lower case letters are used to associate arrivals on the synthetics with robust features on the solution models.

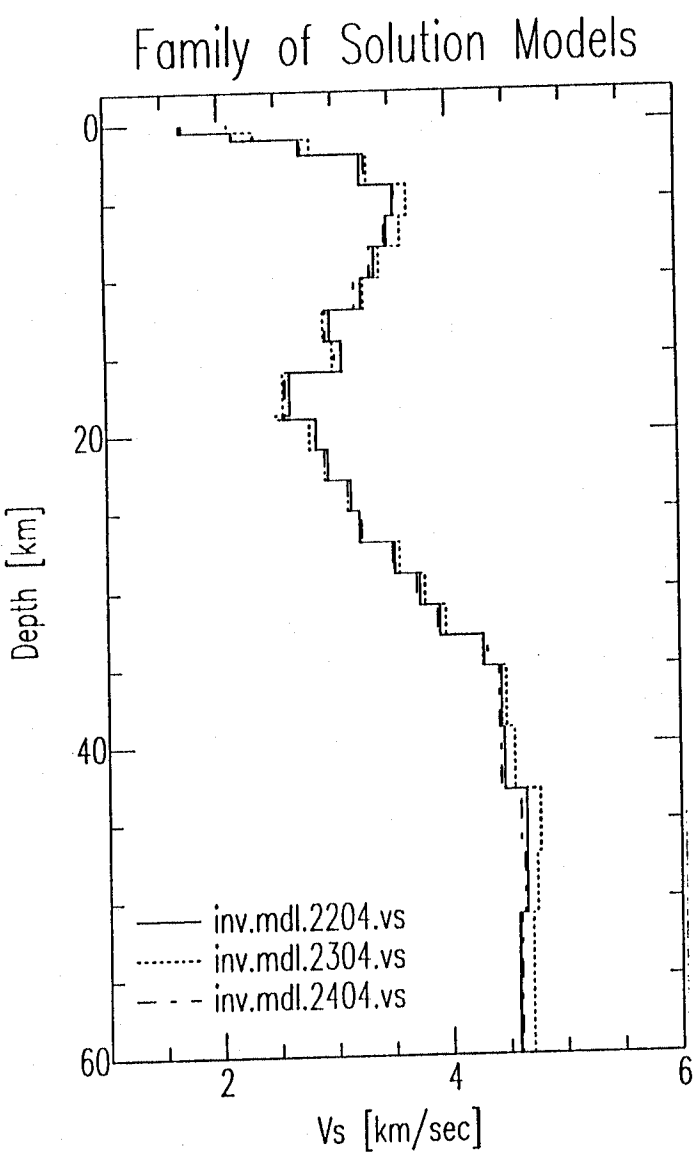

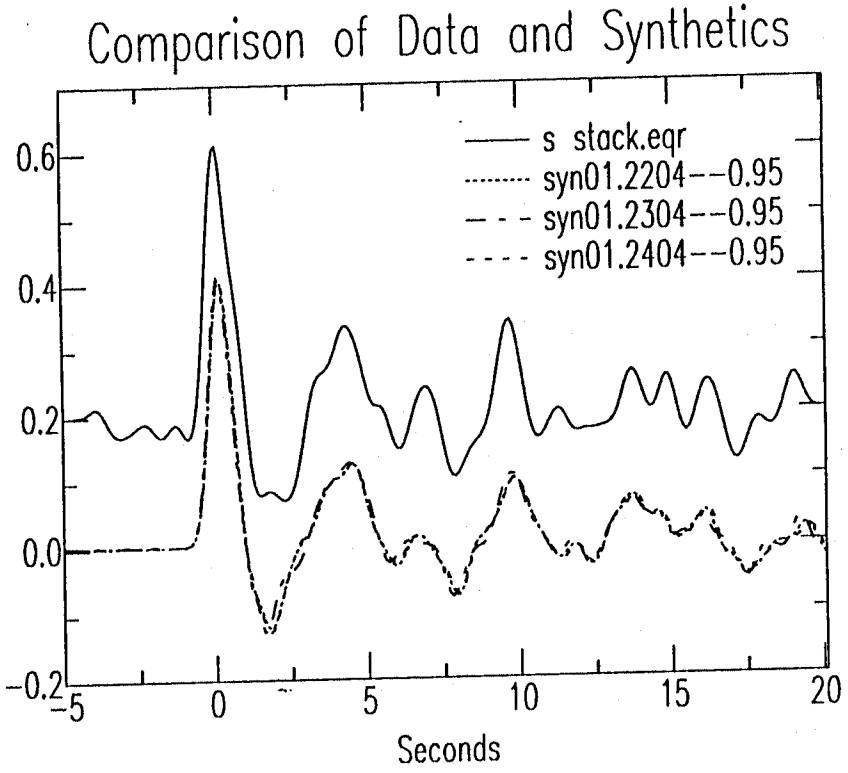

Figure 4.5. (Left) Family of solution models from the inversion of the south data. (Above) Comparison of the stacked receiver function (top trace) and the synthetic receiver functions corresponding to the models on the left (overlain below data). The number following the synthetic labels is the correlation coefficient between the data and the first 12 seconds of the synthetic.

near 12 km (a) which, like the southeast solutions, may possibly correspond to the base of the seismogenic zone. Although feature (a) does not appear to be extremely robust in the family of solutions, removing it leaves the 7 second arrival in the data very poorly fit (Figure 4.7).

Northwest Data Cluster

The family of solutions for the northwest cluster is shown in figure 4.8. Robust features of the solutions include broad low−velocity zones at depths of 4−7 km and 16−18 km. Similar to the southeast and south data, the lower−crustal shear velocities are fairly slow ($\approx$ 3.4 km/sec) to a depth of 30 km. A steady increase in velocities between 30 and 33 km suggests a transitional crust−mantle boundary. Figure 4.9 shows which of the arrivals on the synthetic receiver functions result from each of these robust features. Although the upper−crustal LVZ (a and b) may represent complicated structure localized to the vicinity of station WTX, the arrivals on the receiver function that result from the structure are relatively small and may reflect noise in the deconvolutions process. Removing the 4−7 km low and recomputing the synthetic receiver function does not significantly degrade the fit to the data (Figure 4.10). The strong arrivals on the receiver function are caused primarily by the mid−crustal low (at 16−18 km) and the crust−mantle boundary.

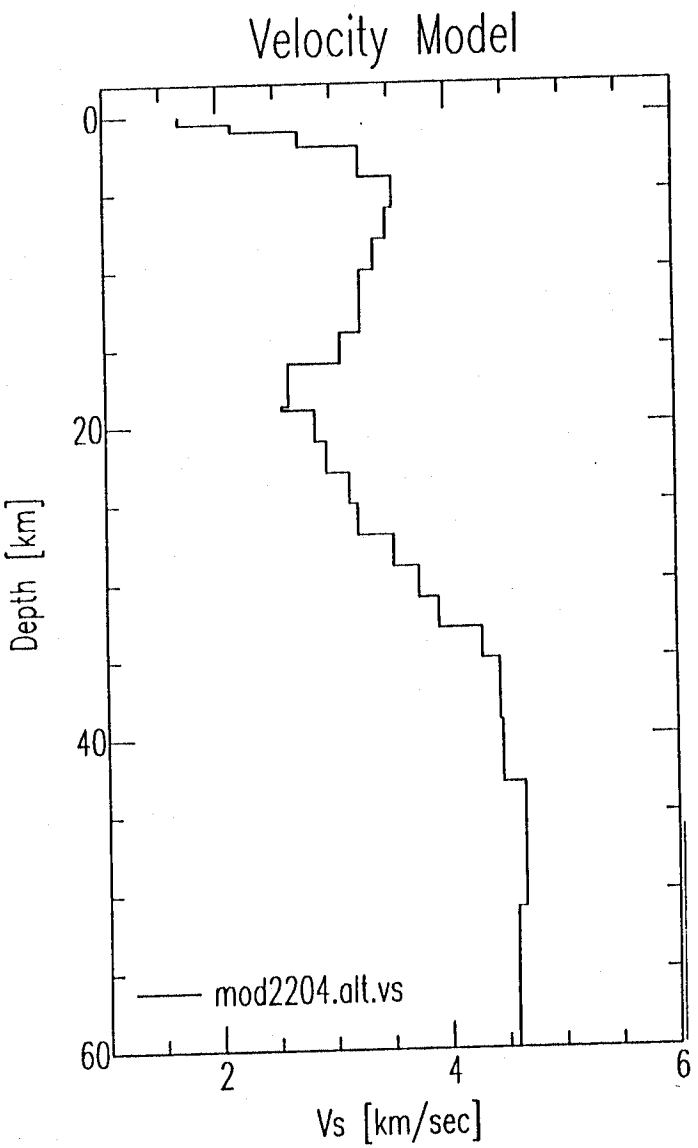

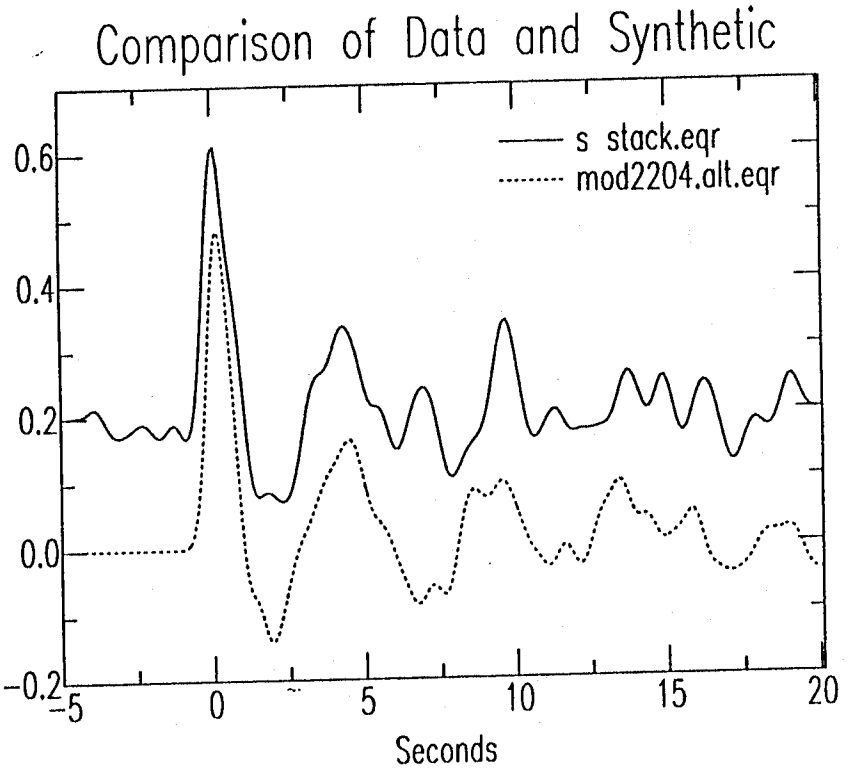

Figure 4.7. (Left) One of the south solution models from Figure 4.6 (model 2204) with feature a removed from the upper crust. (Above) Comparison of the data and the synthetic receiver function corresponding to the model on the left.

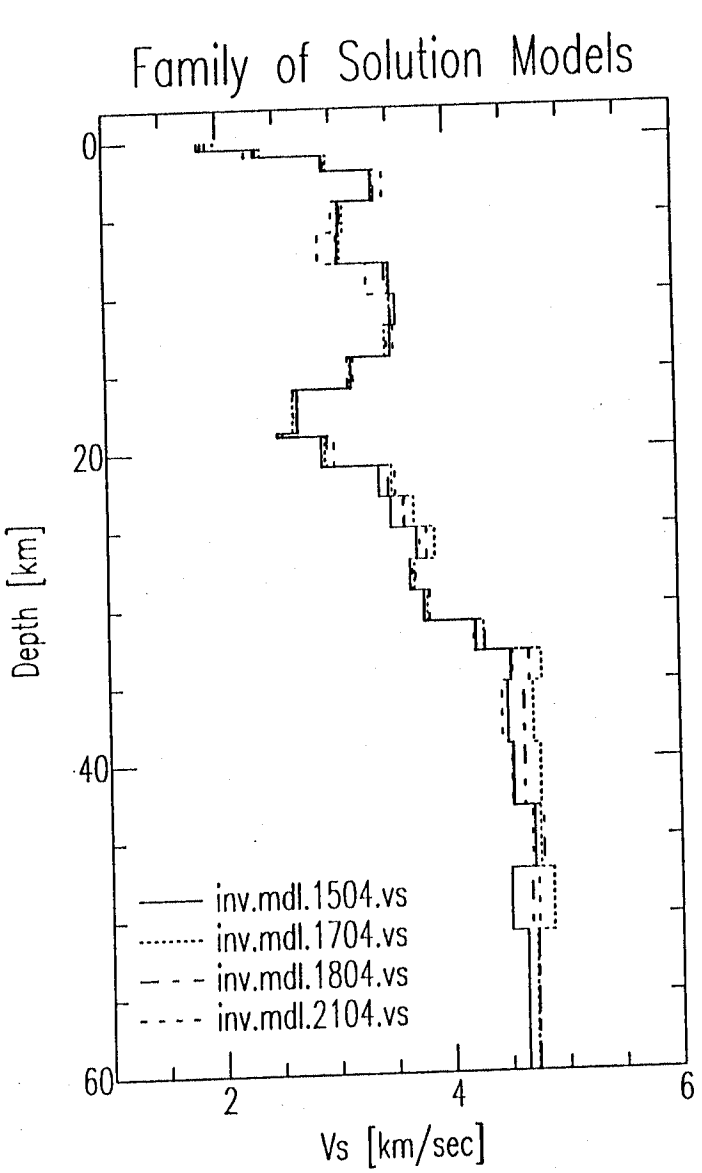

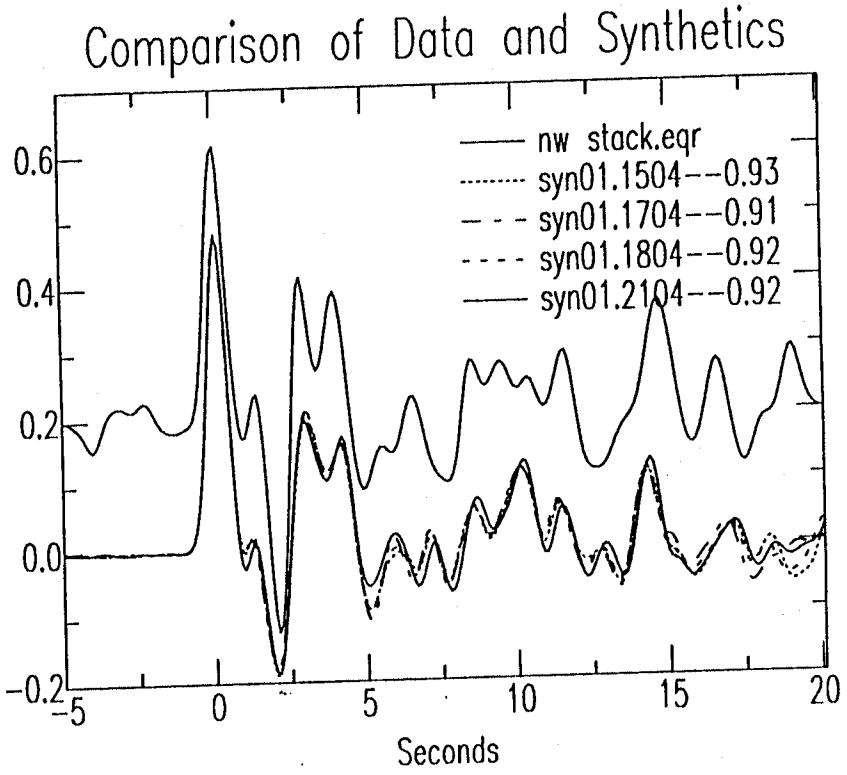

Figure 4.8. (Left) Family of solution models from the inversion of the northwest data. (Above) Comparison of the stacked receiver function (top trace) and the synthetic receiver functions corresponding to the models on the left (overlain below data). The number following the synthetic labels is the correlation coefficient between the data and the first 12 seconds of the synthetic.

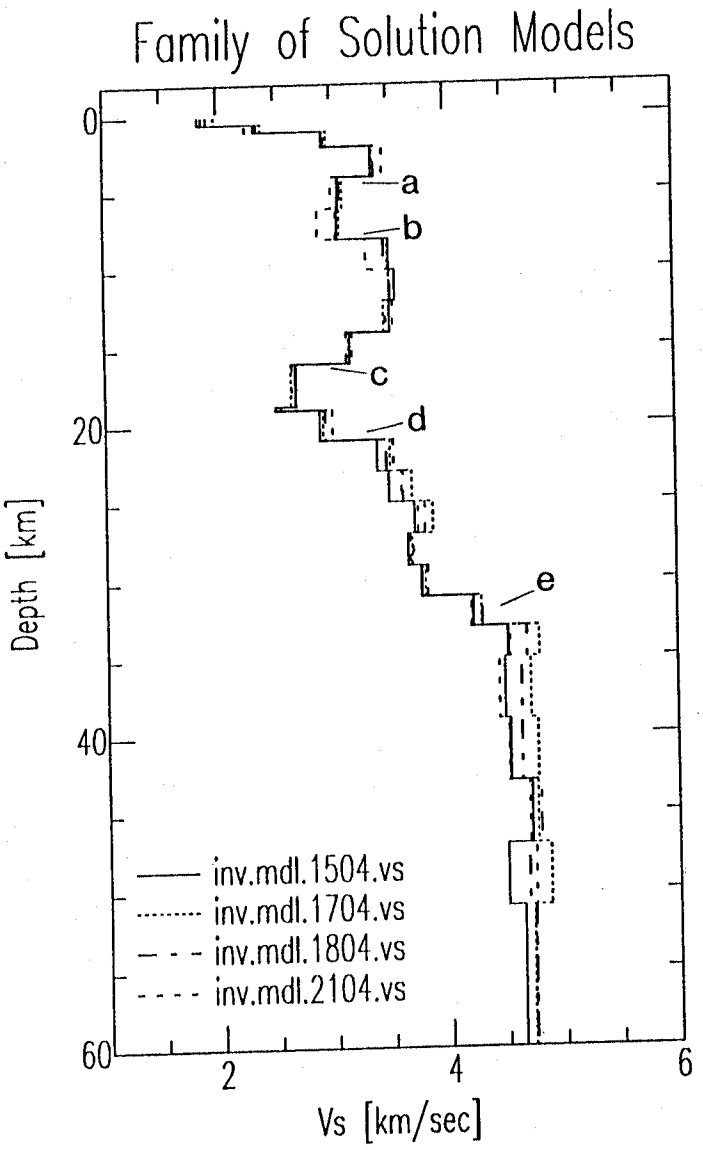

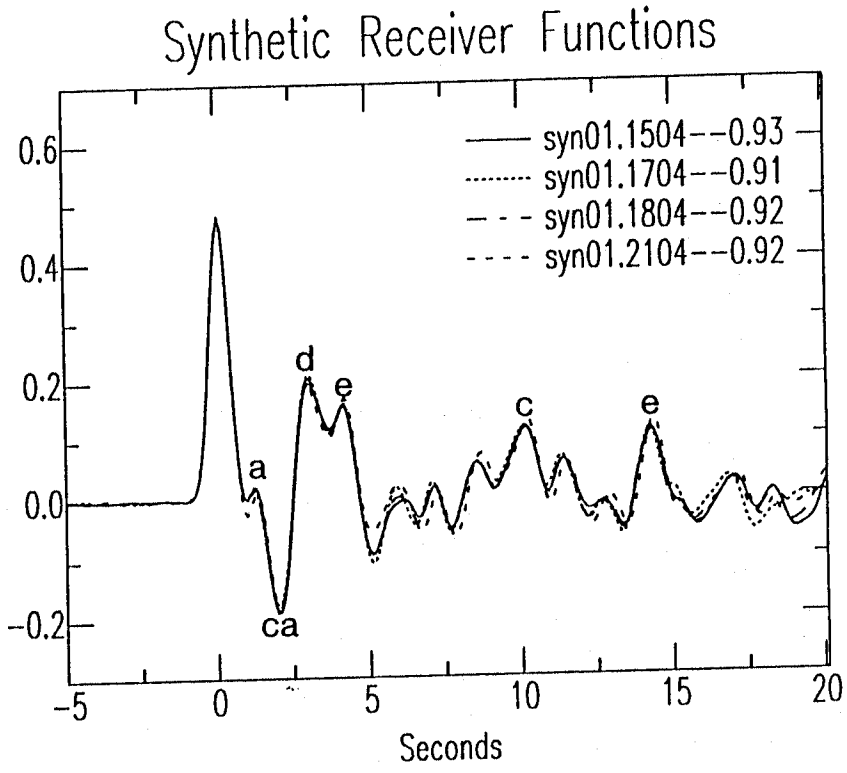

Figure 4.9. (Left) Family of solution models from the inversion of the northwest data. (Above) Overlay of synthetic receiver functions corresponding to the models on the left. Lower case letters are used to associate arrivals on the synthetics with robust features on the solution models.

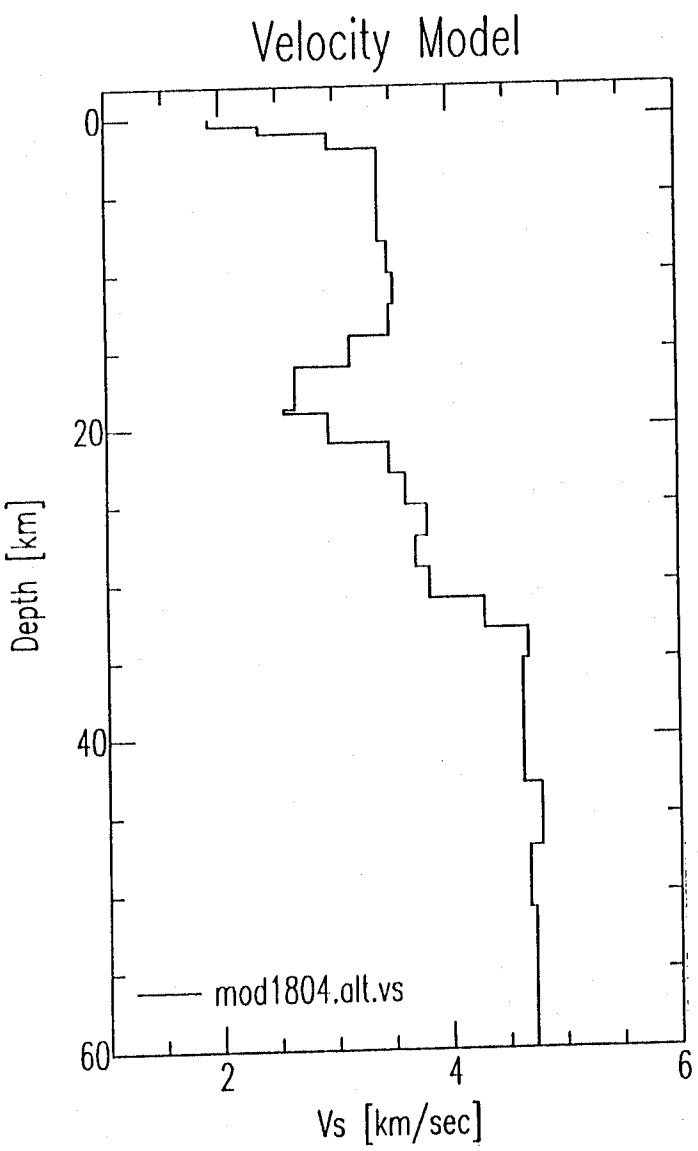

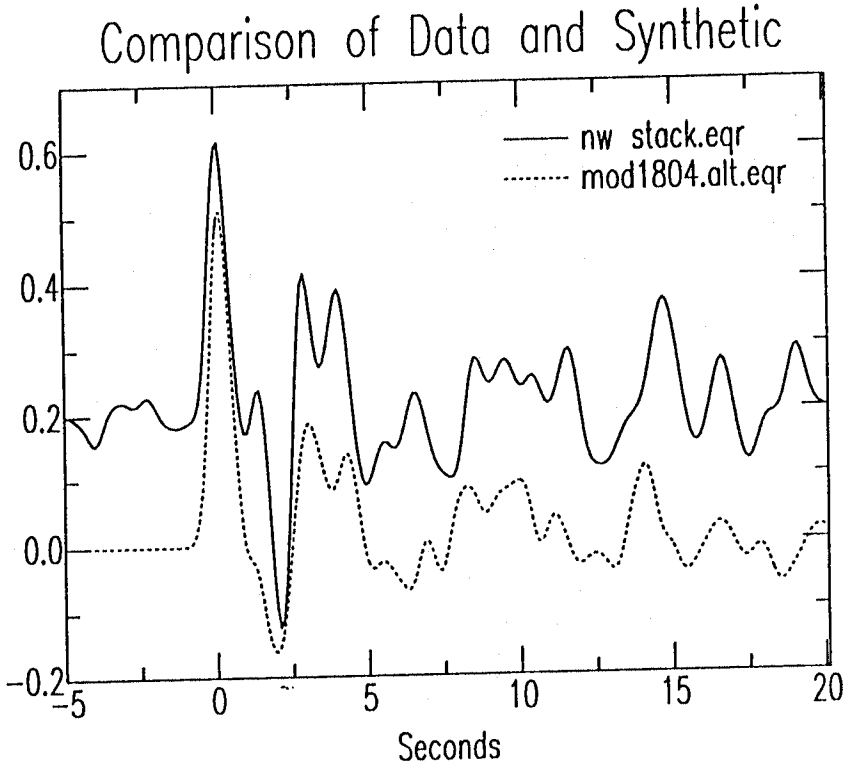

Figure 4.10. (Left) One of the south solution models from Figure 4.9 (model 1804) with features **a** and **b** removed from the upper crust. (Above) Comparison of the data and the synthetic receiver function corresponding to the model on the left.

Common Features of the Three Backazimuth Groups

Although the stacked radial receiver functions from the three different backazimuths are fairly dissimilar and thus invert to different velocity structures, there are three distinct features which are common to the solutions from all three data clusters.

1. A mid–crustal LVZ corresponding to the depth of the Socorro magma body.
2. Anomalously low shear–wave velocities in the lower crust.
3. A crust–mantle boundary between 33 and 35 km.

Mid–Crustal LVZ

Inversion results from each of the data clusters contain a mid–crustal low–velocity zone at a depth that closely corresponds to the depth of the Socorro magma body. To ensure that this feature was not dependent on the existence of the thin magma body in the initial model, inversions were run with the magma body removed from the initial model, and the solutions still contained the robust mid–crustal LVZ. As mentioned above, the smoothness constraint applied to the inversion prevents the solutions from resolving a very thin layer with an extreme velocity contrast like that of the thin magma body in the initial model (Figure 4.4). To examine the effects of such an extreme mid–crustal LVZ, synthetic receiver functions were obtained through forward modeling of the initial model with the thin magma body (hereafter called WMB) and without the thin magma body (hereafter called WOMB). Figure 4.11 shows the models WMB and WOMB and the corresponding synthetic receiver functions. The initial velocity models are exactly the same with the exception of the thin low–velocity layer (shown with a dotted line) representing the 250 meter thick magma body. The synthetic receiver function for WMB is compared to the data from each cluster in Figure 4.12. Note the remarkable similarity between the first five seconds of the

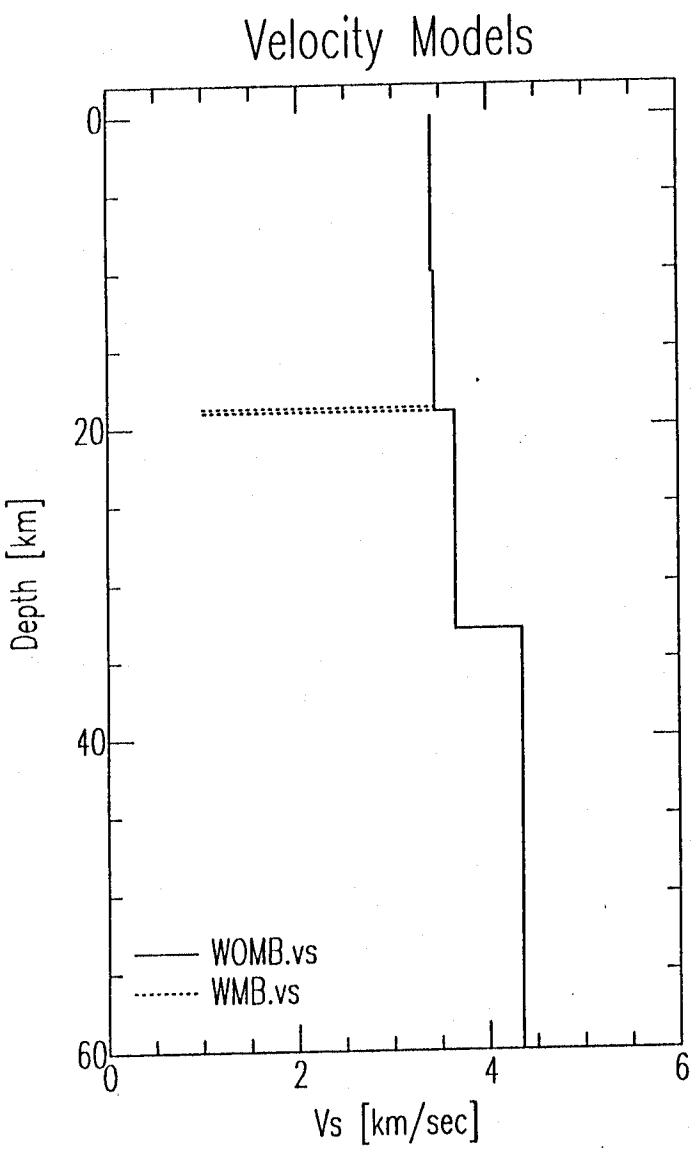

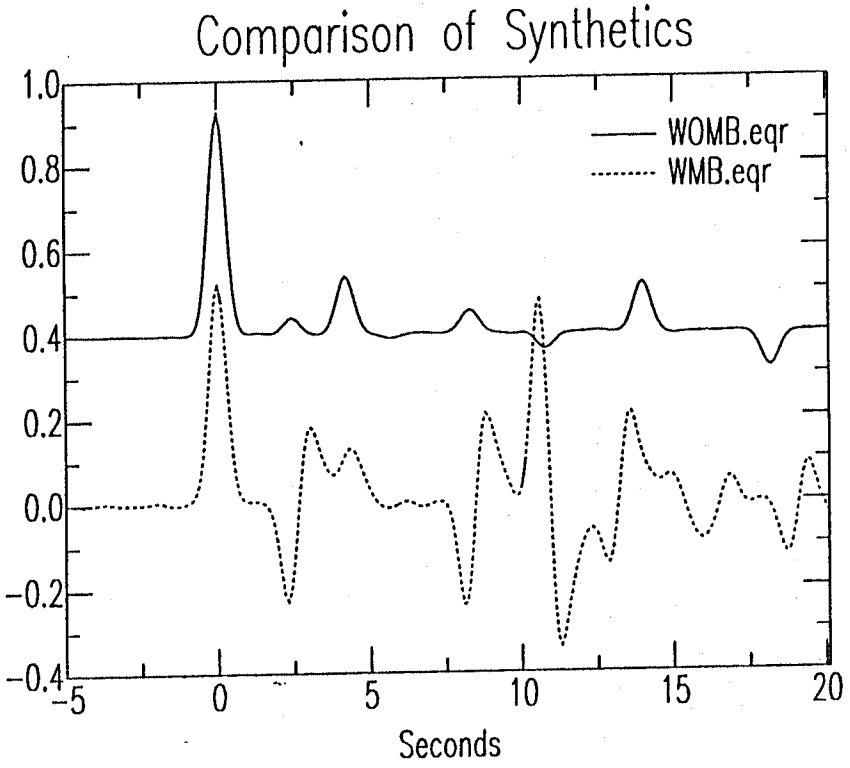

Figure 4.11. (Left) Velocity profiles of the initial model (shown in Figure 4.1) with the magma body (WMB) and without the magma body (WOMB). (Above) Synthetic receiver functions corresponding to the models on the left.

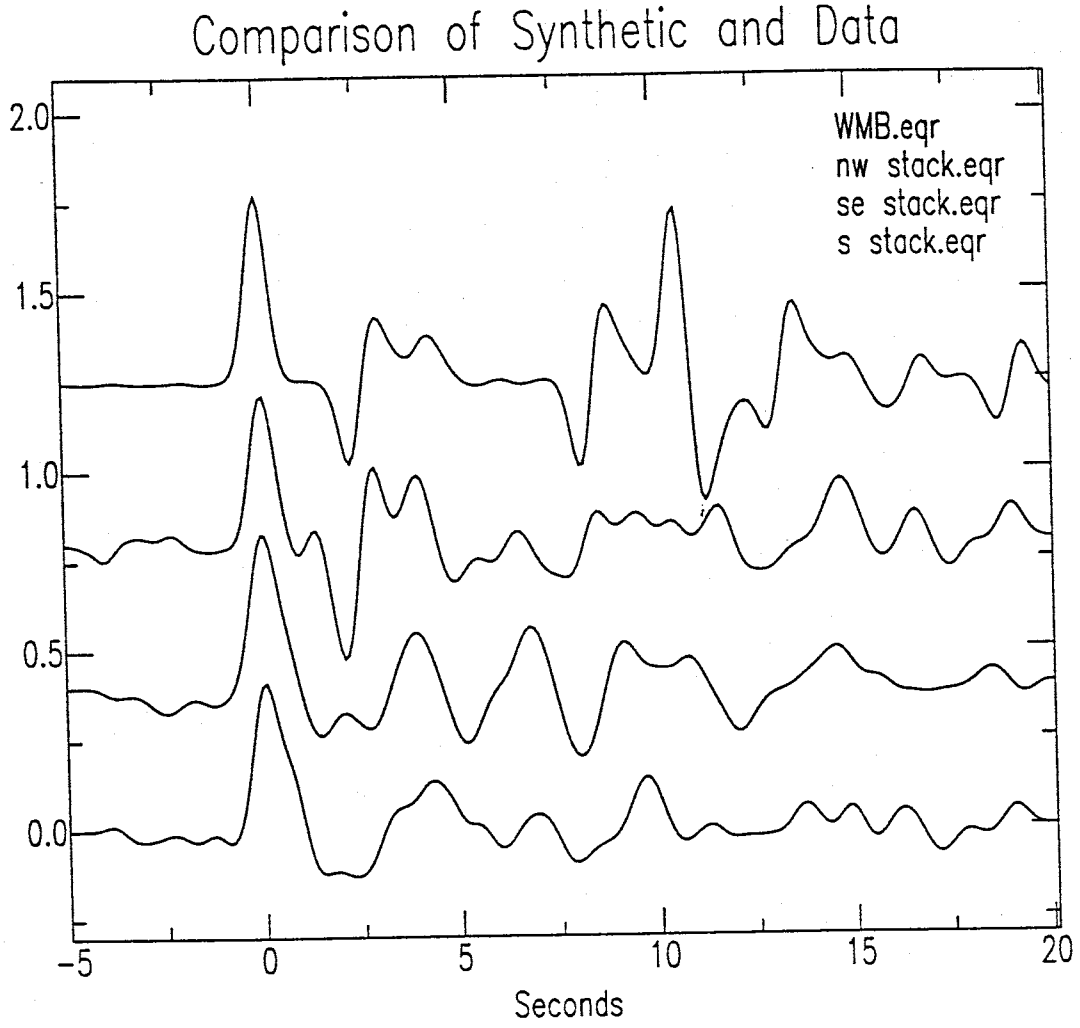

Figure 4.12. Comparison of the synthetic receiver function for model WMB (top trace) and the stacked receiver functions from the northwest, southeast and south (bottom three traces).

WMB synthetic and the data from the northwest. Figure 4.13 shows the WMB synthetic and a ray diagram to illustrate the origin of the prominent arrivals. For simplicity, the diagram contains only three layers: the upper crust, the magma body, and the lower crust. The labels on the rays correspond to the labels on the synthetic receiver function. The arrivals at 2.5 and 2.8 seconds, which match nicely with those on the northwest receiver function, correspond to a P–to–S conversion from of the top of the magma body (ray b) and a reflected shear wave within the magma body (ray c). However, neither of these two phases show up strongly in the southeast or south receiver functions. The arrivals that fall between 8 and 12 seconds (arrivals d – g in Figure 4.13) correspond to multiples that travel to the free surface as P waves before being trapped between the magma body and the surface. The receiver functions from each backazimuth do show some energy between 8 and 12 seconds after the direct P_s (Figure 4.12) but the amplitudes are far less than those on the WMB synthetic.

The forward modeling using WMB indicates that the first five seconds of the northwest receiver function is dominated by the effects of a thin, extremely low velocity layer at a depth corresponding to the Socorro magma body. The southeast and south receiver functions, however, do not appear to be affected by the magma body to the same degree. Figure 4.14 is a map of the lateral extent of the Socorro magma body as determined by *Hartse* [1991]. The magma body extends much further to the north and west of station WTX than to the south and east, and hence may be having a greater effect on the data coming from the northwest. Figure 4.15 shows a cross–section along line AB to illustrate the location of the edges of the magma body with respect to station WTX for energy arriving from the northwest and southeast. The dotted extension of the magma body marks the location of the edge of the magma body for energy arriving from the south. The cross–section shows the raypaths that produce some of the arrivals in the WMB synthetic (arrivals b, d, and f in Figure 4.13). Note that the P to S conversion from the top of the magma body (ray a) occurs near the center of the magma body for the ray from the northwest, and near the edge of the magma body

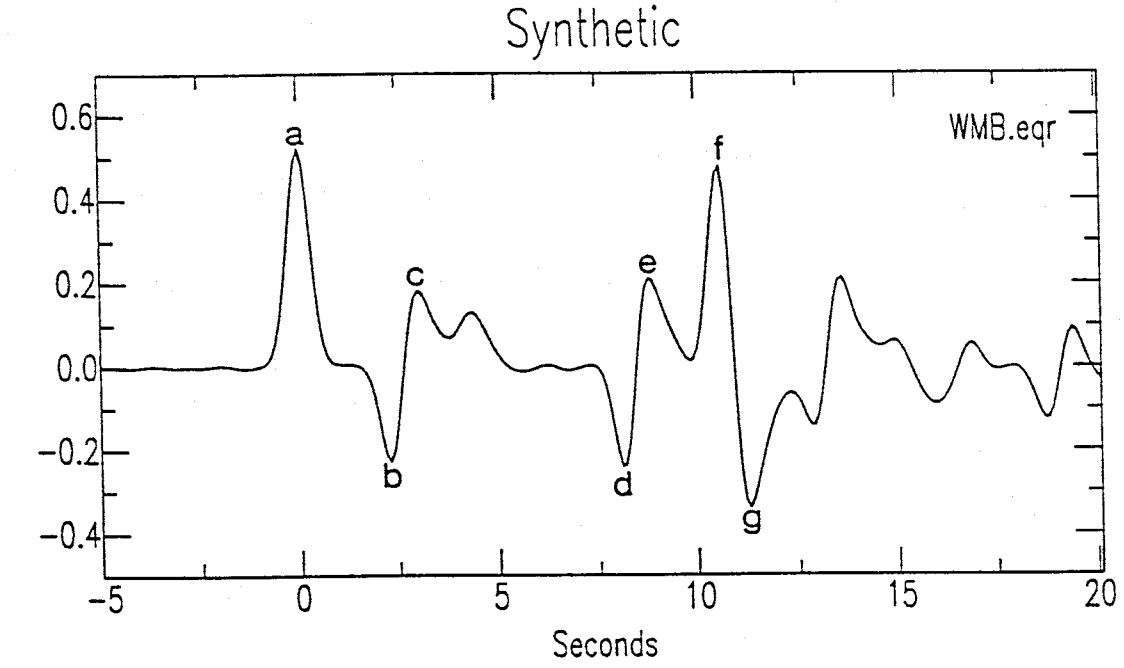

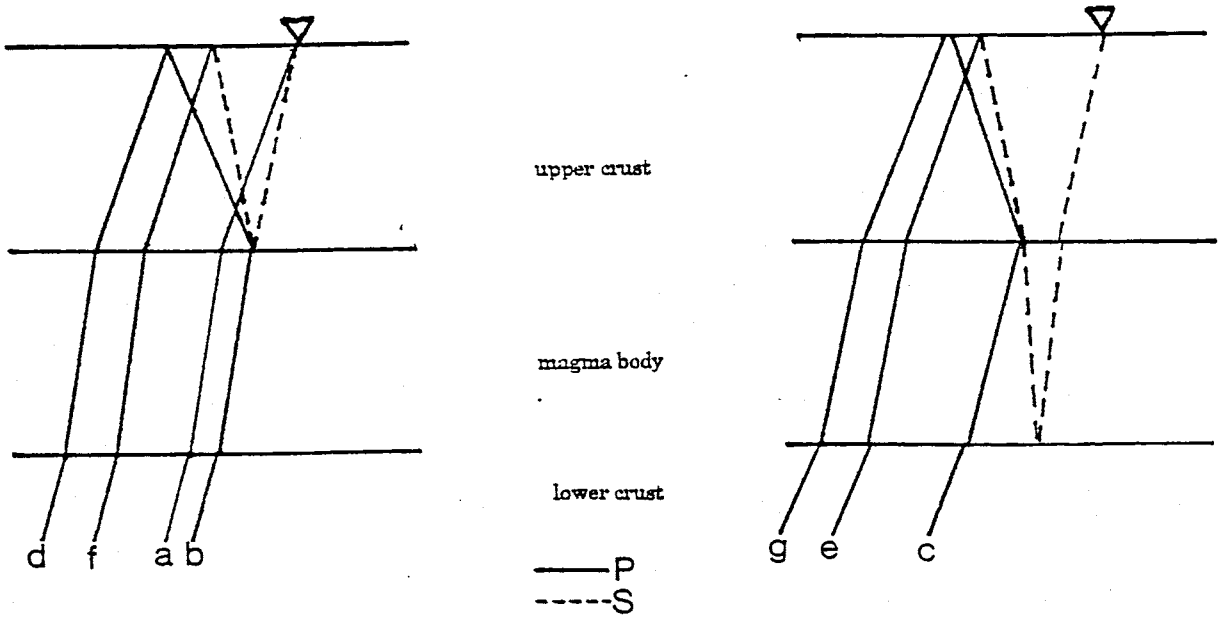

Figure 4.13. (Top) Synthetic receiver function for model WMB. (Bottom) Schematic diagrams showing raypaths through the lower crust, magma body, and average upper crust of model WMB. The thickness of the magma body is vertically exaggerated to view raypaths within the layer. The lower–case letters identify which rays are producing the arrivals on the synthetic that are associated with the magma body.

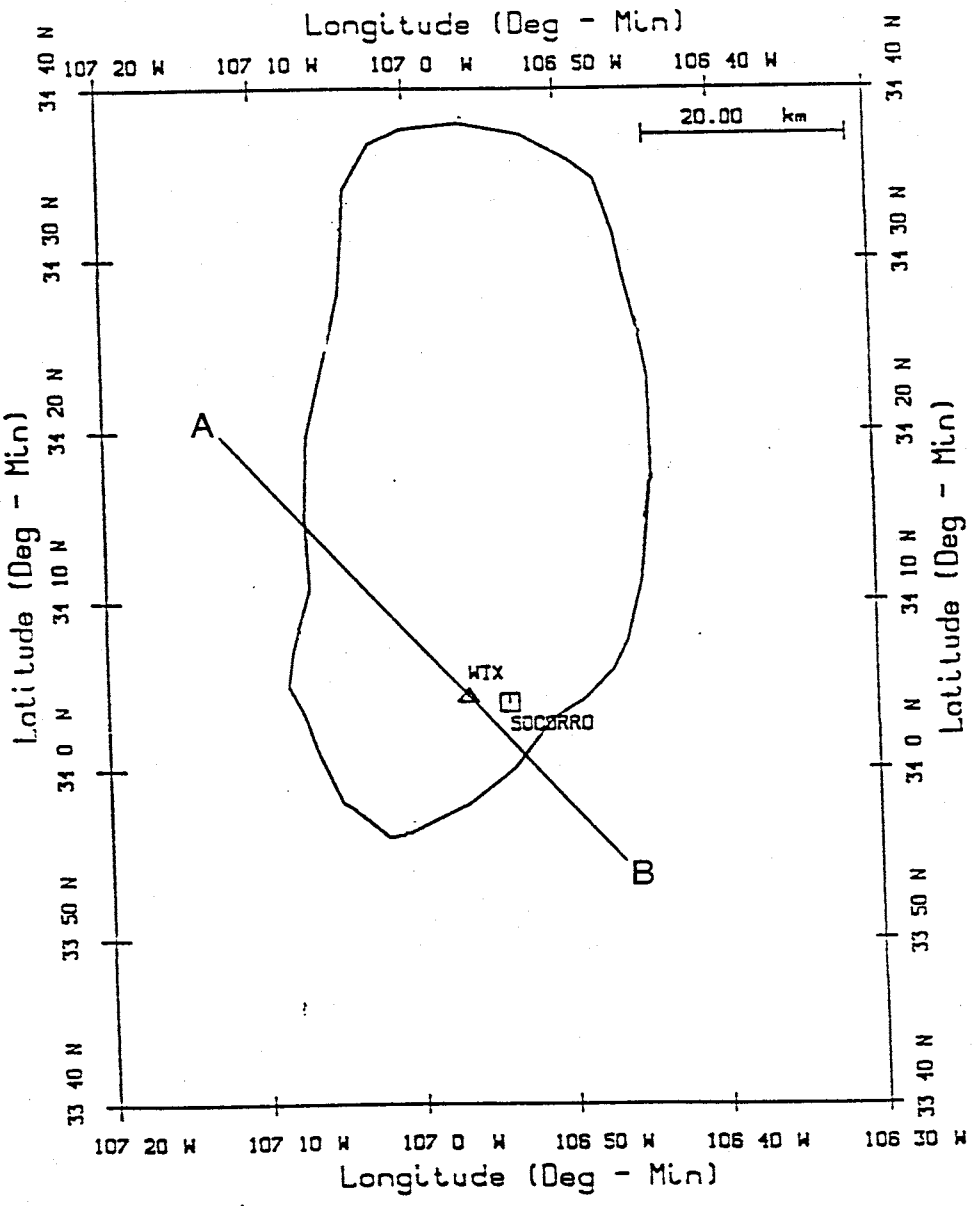

Figure 4.14. Map showing the lateral extent of the Socorro magma body as determined by *Hartse* [1991]. Note that the magma body is much more extensive to the north and west of Socorro than to the south and east. A profile along line AB is shown in Figure 4.15 [after *Hartse*, 1991].

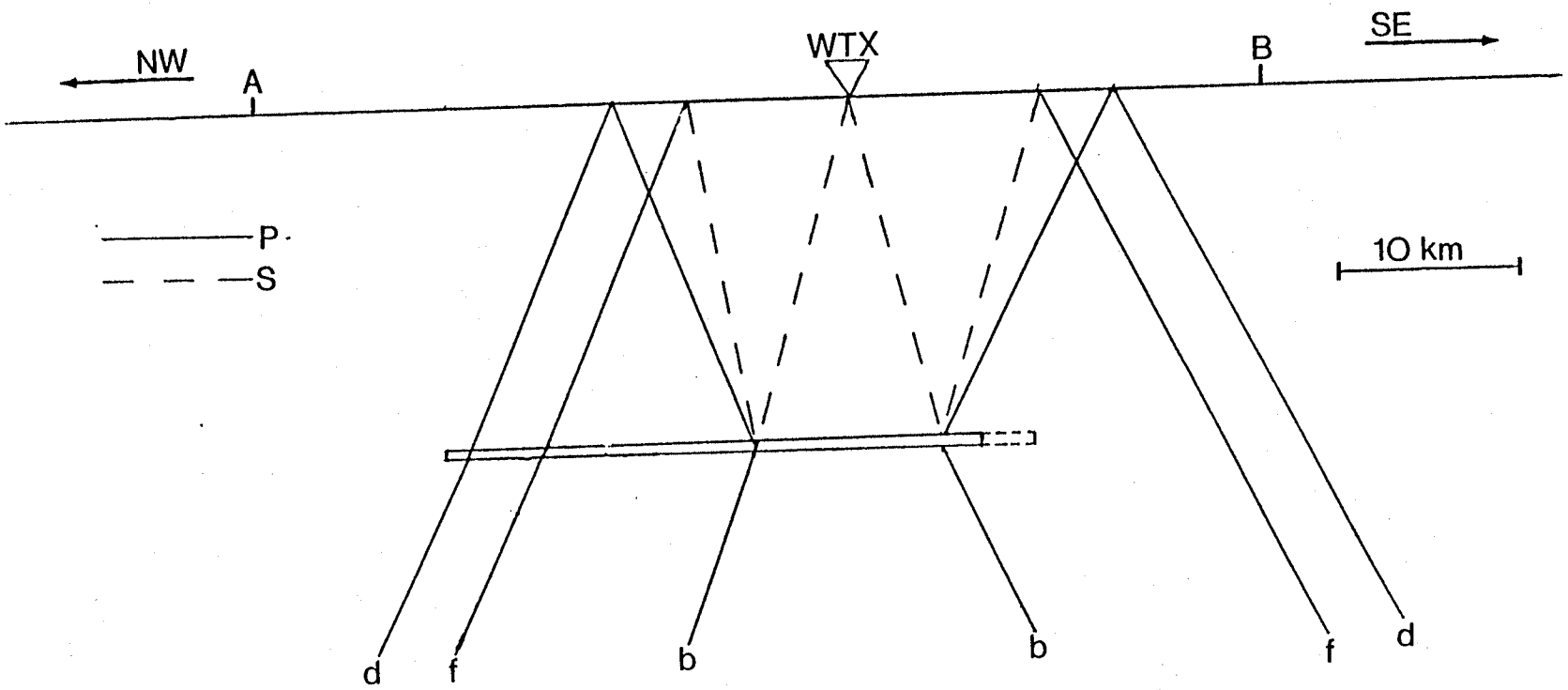

Figure 4.15. Cross–section along line AB of Figure 4.14 to illustrate the location of the edges of the magma body with respect to station WTX for energy arriving from the northwest and southeast. The dotted extension of the magma body marks the location of the edge of the magma body for energy arriving from the south. Raypaths are drawn to illustrate the interaction of the teleseismic energy with the magma body. Labels on the raypaths correspond with the labeled arrivals on the WMB receiver function in Figure 4.13.

from the south and southeast. A possible explanation for the missing P–to–S arrival in the south and southeast receiver functions could thus be that the magma body thins out near the edges, and while still producing reflections in the high frequency microearthquake coda [*Hartse*, 1991], may no longer be detected by the lower frequency (about 1 Hz) teleseismic energy. However, it is important to note that the forward modeling programs assume flat–lying, laterally infinite layers, so the edge effects of a laterally finite, possibly discontinuous magma body have not been included in the modeling of WMB. Until a better understanding of the effects of a thin, laterally finite, thin body on teleseismic P–waveforms is reached, it will be difficult to explain both the differing effects of the magma body on the receiver functions from each cluster, and the absence of the predicted high amplitude multiples.

The first 5 seconds of the northwest data, which is well modeled by the simple velocity model with the magma body, contains arrivals affected by both the top and the bottom of the magma body (arrivals b and c in Figure 4.13). Assuming that these mode conversions from near the center of the magma body are not distorted by edge effects, the data can provide information on the thickness and shear wave velocity of the mid–crustal magma chamber. In an attempt to resolve these parameters, 32 velocity models were created, each having a different combination of shear wave velocity and thickness for the magma body. Eight different thicknesses for the magma body, ranging from 25 meters to 200 meters in increments of 25 meters, each having a shear wave velocity of 0.4, 0.6,, 0.8 and 1.0 km/s were used to construct the 32 models. The P–wave velocities and densities remained the same as those used in the original initial model (see Figure 4.4). A synthetic radial receiver function was calculated for each model and the first 5 seconds of each such synthetic was cross–correlated with the first 5 seconds of the data. Figure 4.16 shows a contour plot of the correlation coefficients as a function of thickness and shear–wave velocity. The orientation of the 0.93 contour illustrates the trade–off between thickness and velocity for the magma body. The model with a 50 m thick magma body and a shear wave velocity of 0.5 km/s matches the first 5 seconds of the data as well as the model with a 150 m thick magma body and a velocity of 0.9 km/s. The trade–off between thickness and

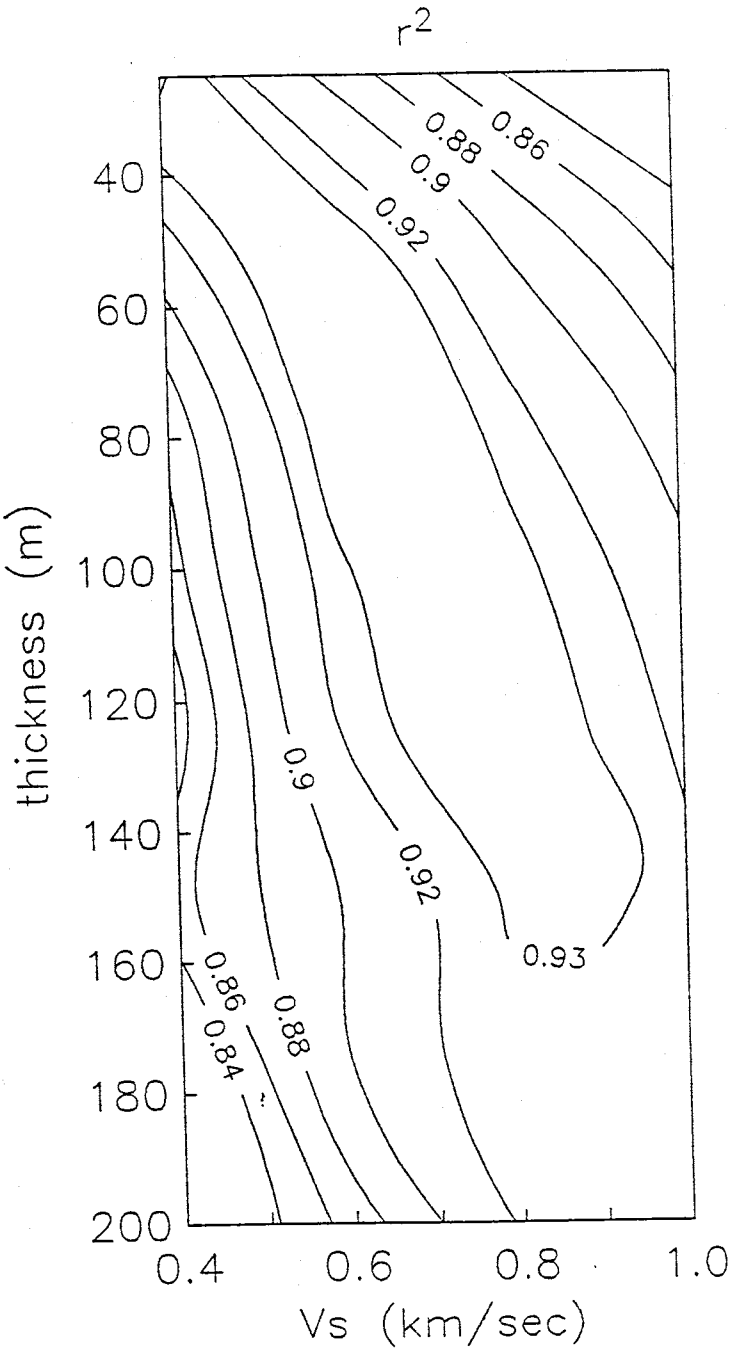

Figure 4.16. Contour plot the correlation coefficients between the stacked receiver function from the northwest and 32 synthetic receiver functions obtained by varying the thickness and shear–wave velocity of the magma body in model WMB. Eight different thicknesses, ranging from 25 to 200 meters in increments of 25 meters, each having a shear–wave velocity of 0.4, 0.6, 0.8,and 1.0 km/sec were used to construct the 32 models. The open–ended contour at the upper–left corner of the plot could not be closed because the forward modeling and deconvolution programs became unstable when extremely thin, low–velocity layers are used.

shear–wave velocity indicates that the arrivals in the 5 second window of data cannot alone constrain the best fitting model. However, the contour plot does suggest a maximum thickness/velocity combination of about 160m and 0.95km/s for models that fit the data well. The open–ended contour at the upper left corner of the plot could not be closed because the forward modeling and deconvolution codes became unstable when extremely thin, low–velocity layer are used.

Low Shear Wave Velocities in the Lower Crust

The second common feature in all solutions is the anomalously low shear–wave velocities from the base of the mid–crustal LVZ to a depth of about 30 km. Velocities in this region are between 3.0 and 3.5 km/s (see Figures 4.2, 4.5 and 4.8). In comparison with the velocities of the neighboring provinces, and the southern Rio Grande rift, these velocities are quite slow. From refraction surveys in the Great Plains [*Roller,* 1965; *Gish et al.,* 1981], and in the Basin and Range [*Steward and Pakiser,* 1962], the P–wave velocity of the lower crust at the east and west flanks of the rift is 6.7–6.8 km/s. In an overview of the crustal structure of the Rio Grande rift, *Olsen et al.* [1987] state that the compressional velocity of the lower crust beneath the rift, inferred from refraction surveys, is 6.4–6.5 km/s. *Sinno and Keller* [1986] combined surface wave and refraction data to determine a Poisson's ratio of 0.27 for the southern Rio Grande rift. Using this value, the P–wave velocities from *Olsen et al.* [1987] for the Rio Grande rift correspond to an S–wave velocity range of 3.60–3.65 km/s, considerably higher than those found in this study. Given the P–wave velocity of 6.4–6.5 km/s [*Olsen et al.,* 1987], and an S–wave velocity of 3.0–3.5 km/s [this study], Poisson's ratio in the lower crust could range from 0.29–0.36 (0.33 using average velocities). These high values for Poisson's ratio in the crust underlying the magma body beneath station WTX are indicative of elevated temperatures, and the upper bound (0.36) suggests some degree of partial melting. However, with this data set alone, it is difficult to estimate the quantities of melt that could exist in the lower crust. In an interesting study by *Sato et al.* [1988], laboratory measurements of seismic velocities in upper mantle peridotite were used to determine the thermal state of a low velocity zone beneath the Iceland Plateau. By using the ratio of the anoma-

lously low velocity of the asthenospheric LVZ to the lithospheric velocity, they were able to estimate the percent of partial melt. The ratio they obtained was 0.87, which corresponds to a melt fraction of 7%. The ratio of the average lower-crustal velocity beneath station WTX to the average lithospheric velocity of the surrounding regions also happens to be 0.87. Although this is an interesting coincidence, *Sato et al.* [1988] based their relationship between velocity and melt fraction on empirical data for mantle materials, and such relationships cannot necessarily be applied to the lower crust beneath the Socorro magma body. Another interesting result of the study by *Sato et al.* [1988] is that a velocity drop of up to 6% in the asthenosphere relative to the velocity of the lithosphere can be accounted for with subsolidus heating and does not require the existence of partial melt. Again, the exact numbers from their study may not be applicable to this study, but it is important to realize that velocities can decrease substantially in a given region without extensive partial melting.

If the region beneath the Socorro magma body is dominated by pervasive melting, very low Q values would be expected in the lower crust. *Solomon* [1973] studied shear wave attenuation from a very low Q zone beneath the Mid-Atlantic ridge. He found the low Q values (10 or less) to be explained by extensive partial melting due to convective upwelling beneath the ridge axis. Figure 4.17 shows synthetic receiver functions for the model WOMB (shown in Figure 4.11). The solid trace shows the receiver function calculated with standard crustal Q values of $Q_p = 600$ and $Q_s = 300$ for all layers. The dotted trace shows the receiver function calculated with the Q of the lower crust (20-33 km) reduced to $Q_p = 10$ and $Q_s = 5$. The arrival near 4.5 seconds, which represents the P-to-S conversion from the Moho and has traversed the lower crust once as an S wave, is attenuated by nearly 50% in the synthetic calculated with the low-Q lower crust. The arrival near 19 seconds, which represents a multiple that traverses the lower crust twice as a P wave and once as an S wave, is attenuated by over 50% in the synthetic calculated with the low-Q lower crust. Figure 4.18 shows the receiver functions for each azimuthal cluster with dots above the arrivals corresponding to the direct P-to-S conversion from the Moho and the later arriving Moho multiple. All three receiver functions have a strong P-to-S conversion

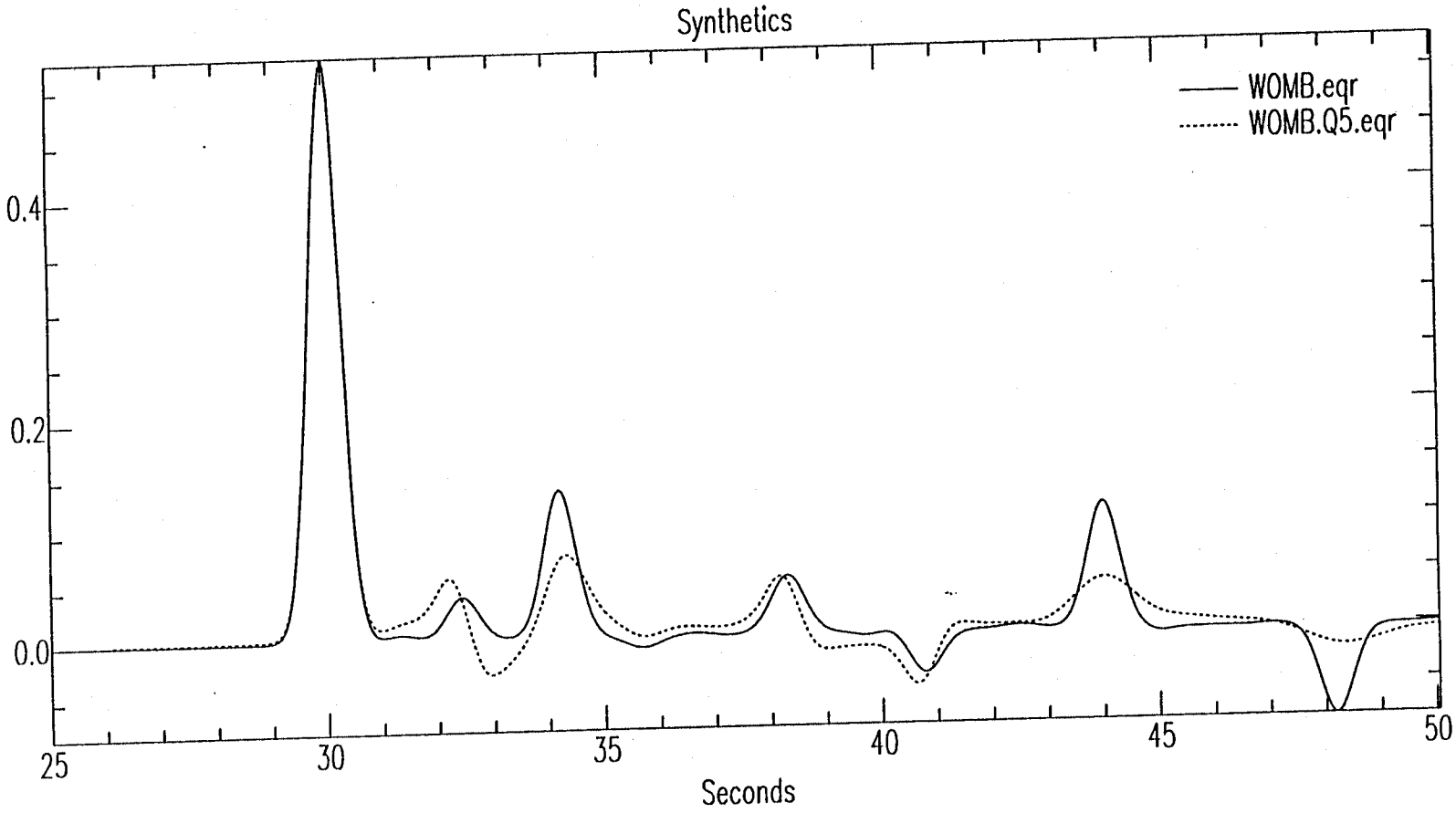

Figure 4.17. Synthetic receiver functions for model WOMB (shown in Figure 4.11). The solid trace shows the receiver function calculated with standard crustal Q values of $Q_p = 600$ and $Q_s = 300$ for every layer. The dotted trace shows the receiver function calculated with the Q values of the lower crust (20–33 km) reduced to $Q_p = 10$ and $Q_s = 5$.

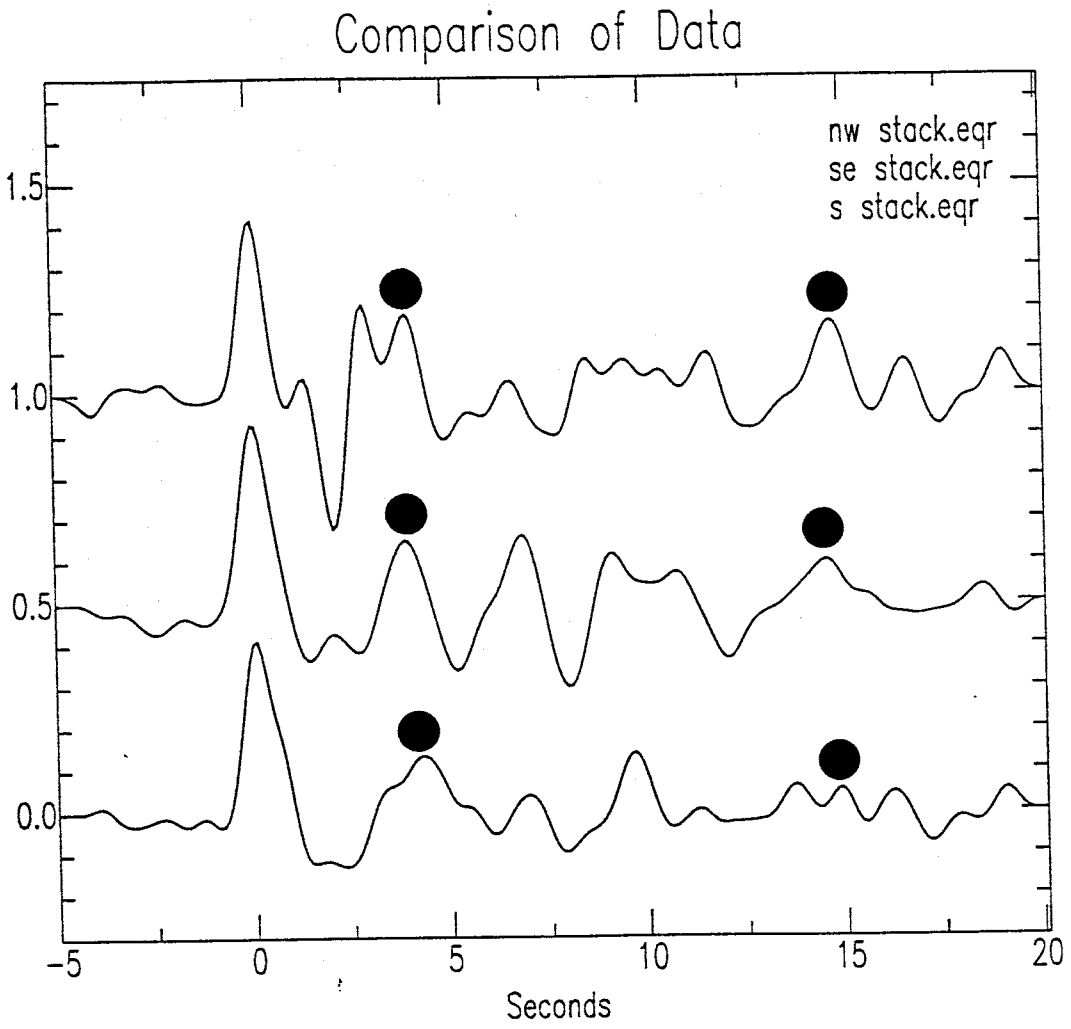

Figure 4.18. Stacked receiver functions from the northwest, southeast, and south clusters. The dots indicate the P−to−S conversion from the Moho (first dot) and the later−arriving Moho multiple (second dot) on each trace.

from the Moho, and the northwest and southeast receiver functions have the Moho multiple with amplitudes on the order of the direct P–to–S. The presence of these high amplitude arrivals associated with the Moho suggests that the lower crust beneath the magma body is not an extremely attenuative region of pervasive melt.

The very low shear wave velocities [this study] and the inferred high heat flow values [*Clarkson and Reiter*, 1974] in the lower crust, along with the evidence for an active magma supply to the Socorro magma body [*Reilinger et al.*, 1980] suggests that the crust beneath the magma body is somehow supporting magma transport to mid–crustal depths. If the arrivals on the receiver functions do not indicate that the lower crust is dominated by extensive partial melting, then perhaps the magma reaches mid–crustal depths through conduits in a very hot but solid lower crust with a Poisson's ratio that is closer to the lower bound (0.29) discussed above. Such conditions would allow for heated pathways through which magma could migrate while maintaining fairly normal overall Q values in the lower crust.

Crust–Mantle Boundary

The third feature common to the solutions from all three clusters is a Moho depth of 33–35 km. As mentioned in the above section, the arrival corresponding to the P–to–S conversion from the Moho is quite pronounced in all three stacked receiver functions (Figure 4.18). The conversion arrives at 3.9, 4.0, and 3.9 seconds for the southeast, south and northwest data respectively. The velocity of the upper mantle, however, is not well constrained. The shear wave velocities range from 4.3 – 4.7 km/s.

Many of the previous refraction surveys in the Rio Grande rift have also obtained Moho depths between 33 and 35 km, but the mantle velocities differ considerably among the individual studies. *Olsen et al.* [1979] obtained a Moho depth of 33.7 km and a mantle P–wave velocity of 7.6 km/s from an unreversed refraction survey in the central and northern Rio Grande rift. *Jaksha* [1982] obtained a Moho depth of 34 km and a mantle P–wave velocity of 8.0 km/s from a

reversed refraction survey in the Rio Grande rift and southwestern New Mexico. *Singer* [1989] , using time−term analysis of P_n phases in the Socorro area, found a Moho depth of 33.5 km and a mantle P−wave velocity of 8.1 km/s. Like the families of solutions from this study, these refraction studies are in good agreement concerning the depth of the crust−mantle interface, but consist of a wide range of mantle velocities. Unfortunately, this makes estimating Poisson's ratio in the upper mantle impossible. Given the range of S−wave velocities from this study (4.3 − 4.7 km/s) and the range of P−wave velocities from the above refraction studies (7.6 − 8.1 km/s), Poisson's ratio could range from 0.19 to 0.30. The upper limit of 0.30 is surprisingly lower than the average value of 0.33 estimated from this study for the lower crust, however, in light of the difficulty constraining the shear−wave velocity beneath the Moho in this study, little can be concluded about the upper mantle conditions beneath station WTX.

5. CONCLUSIONS

The stacked receiver functions from each of the backazimuths used in this study have distinct characteristics that set them apart from one another. The strong dependence of receiver function features on azimuth is indicative of lateral heterogeneity in the vicinity of station WTX. One prominent source of such lateral heterogeneity is the Socorro magma body. Forward modeling results show the effects of the magma body dominating the first three seconds of the receiver functions from the northwest, while having subtle effects on the receiver functions from the south and southeast. This difference in the receiver functions is believed to be a result of the lateral extent of the magma body which is much greater to the north and west of station WTX than to the south and east. Accordingly, the teleseismic energy approaching station WTX from the northwest will encounter the magma body near its center, while the energy approaching from the south and southeast will encounter the magma body near the edges where the body may be thin or discontinuous.

The first three seconds of the northwest receiver function contain arrivals from the top and the bottom of the magma body. Trial–and–error forward modeling provides an upper limit of about 160 meters for the thickness of the magma body. Computational limitations prevent an estimate of the minimum thickness for the magma body.

Despite the differences in the receiver functions from the three backazimuths, the solutions resulting from their inversion, which differ primarily in the upper crust, all have anomalously slow shear wave velocities in the 10 km directly beneath the magma body. Ranging from 3.0 to 3.5 km/sec, these shear wave velocities suggest elevated temperatures and the possible existence of partial melt in the lower crust. Based on shear wave velocities alone, it is difficult to determine whether the lower crust is undergoing extensive in–situ heating from an upwelled asthenosphere, with a magma body that is underlain by a zone of pervasive melting like that of the model for fast spreading oceanic ridges (Figure

1.3), or whether the lower crust is a region of hot but still solidified rock transected by dikes which act as conduits to supply the magma body from an asthenospheric source, as suggested by the model in Figure 1.9. However, forward modeling results indicate that extremely low Q values (10 or less) in a lower crust associated with extensive partial melting would cause the P–to–S conversions and associated multiples from the crust–mantle boundary on the receiver function to be attenuated by 50% or more relative to a receiver function calculated with standard Q values in the lower crust. The receiver functions calculated from the data arriving at station WTX from the northwest and southeast have strong P–to–S conversions and multiples from a crust–mantle boundary at depths between 33 and 35 km. It is thus believed that the receiver functions obtained for station WTX do not show signs of a highly attenuative lower crust, and thus the mechanism for transporting magma from the source region to the mid–crustal magma chamber is more likely to be a network of feeder dikes that elevate the temperatures of the lower crust, rather than a vast partially solidified crystal mush zone.

6. REFERENCES

Ake, J.P. and A.R. Sanford (1988). New evidence for the existence and internal structure of a thin layer of magma at mid−crustal depths near Socorro, New Mexico, *Bull. Seismol. Soc. Am., 78,* 1335−1359.

Aki, K. and P.G. Richards (1980). *Quantitative Seismology: Theory and Methods, Vol. 1,* W.H. Freeman, San Francisco.

Aldouri, R, D. Doser, R. Keller, and E. Dean (1992). Shear wave velocity and crustal structure of the Rio Grande rift and the Basin and Range, *Seismological Research Letters, 63,* 69.

Ammon, C.J. (1991). The isolation of receiver effects from teleseismic P waveforms, *Bull. Seismol. Soc. Am., 81,* 2504−2510.

Ammon, C.J., G.E. Randall, and G. Zandt (1990). On the nonuniqueness of receiver function inversions, *J. Geophys. Res., 95,* 15303−15318.

Baker, B.H. and P. Morgan (1981). Continental rifting: progress and outlook, *EOS, Trans. Am. Geophys. Un., 62,* 585−586.

Bloomer, S.H., J.H. Natland, and R.L. Fisher (1989). Mineral relationships in gabbroic rocks from fracture zones of Indian Ocean ridges: evidence for extensive fractionation, parental diversity and boundary−layer recrystalization, in *Magmatism in the Ocean Basins,* edited by A.D. Saunders and M.J. Norry, Geol. Soc. London Spec. Publ., 42, 107−124.

Braile, L.W., R.B. Smith, G.R. Keller, R.M. Welch, and R.P. Meyer (1974). Crustal structure across the Wasatch Front from detailed seismic refraction studies, *J. Geophys. Res., 79,* 2669−2677.

Brown, L.D., P.A. Krumhansl, C.E. Chapin, A.R. Sanford, F.A. Cook, S. Kaufman, J. Oliver, and F.S. Schilt (1979). COCORP seismic reflection studies of the Rio Grande rift, in *Rio Grande Rift: Tectonics and Magmatism,* edited by R.E. Riecker, AGU, Washington, D.C., 169−184.

Cann, J.R. (1974). A model for oceanic crustal structure developed, *Geophys. J. R. Astr. Soc., 39,* 169−187.

Chapin, C.E., and W.R. Seager (1975). Evolution of the Rio Grande rift in the Socorro and Las Cruces areas, *New Mexico Geological Society, Guidebook 26*, 297–321.

Clarkson, G. and M. Reiter (1984). Analysis of terrestial heat–flow profiles across the Rio Grande rift and southern Rocky Mountains in northern New Mexico, *New Mexico Geol. Soc. Guidebook, 26*, 39–44.

Clayton, R.W. and R.A. Wiggins (1976). Source shape estimation and deconvolution of teleseismic body waves, *Geophys. J. Royal Astron. Soc., 47*, 151–177.

Cordell, L., G.R. Keller, and T.G. Hildenbrand (1982). Bouguer gravity map of the Rio Grande rift, Colorado, New Mexico, and Texas, *U.S. Geol. Surv.*, Map GP–949.

Decker, E.R., G.R. Keller, and J.N. Stewart (1979). Crustal structure along the Rio Grande rift from seismic refraction profiles, in *Rio Grande Rift: Tectonics and Magmatism,* edited by R.E. Riecker, AGU, Washington, D.C., 127–144.

Detrick, R.S., P. Buhl, E. Vera, J. Mutter, J. Orcutt, J. Madsen, and T. Brocher (1987). Multichannel seismic imaging of a crustal magma chamber along the East Pacific Rise, *Nature, 326*, 35–41.

Duffield, W.A., C.R. Bacon, and G.B. Dalryple (1980). Late Cenozoic volcanism, geocronology and structure of the Coso range, Inyo County, California, *J. Geophys. Res., 85*, 2381–2404.

Eaton, J.R. (1962). Crustal structure and volcanism in Hawaii, in *The Crust of the Pacific Basin, Geophys. Monogr. 6*, edited by G.A. MacDonald and H. Kuno, AGU, Washington, D.C., 13–29.

Eaton, J.R. and K.J. Murita (1960). How volcanoes grow, *Science, 132*, 925–938.

Fowler, C.M.R. (1976). Crustal structure of the Mid–Atlantic ridge crest at 37°N, *Geophys. J. R. Astron. Soc., 47*, 459–491.

Gish, D.W., G.R. Keller, and M.L. Sbar (1981). A refraction study of deep crustal structure in the Basin and Range: Colorado Plateau of eastern Arizona, *J. Geophys. Res., 86*, 6029–6038.

Hall, J.M. and P.T. Robinson (1979). Deep crustal drilling in the North Atlantic Ocean, *Science, 204*, 573–586.

Hartse, H.E. (1991). Simultaneous hypocenter and velocity model estimation using direct and reflected phases from microearthquakes recorded within the central Rio Grande rift, New Mexico, *Ph.D. Dissertation*, New Mexico Tech, Socorro, New Mexico, 252pp.

Hartse, H.E. and A.R. Sanford (1992) A new map of the Socorro magma body, *Seismological Research Letters, 63*, 69.

Hermance, J.F. and J. Pedersen (1980). Deep structure of the Rio Grande rift: A magnetotelluric interpretation, *J. Geophys. Res., 85*, 3899–3912.

Jaksha, L.H. (1982). Reconnnaissance seismic refraction–reflection surveys in southwestern New Mexico, *Geol. Soc. Am. Bull., 93*, 1030–1037.

Jiracek, G.R., M.E. Ander, and H.T. Holcombe (1979). Magnetotelluric soundings of crustal conductive zones in major continental rifts, in *Rio Grande Rift: Tectonics and Magmatism,* edited by R.E. Riecker, AGU, Washington, D.C., 209–222.

Keller, G.R., R.B. Smith, and L.W. Braile (1975). Crustal structure along the Great Basin–Colorado Plateau transition from seismic refraction studies, *J. Geophys. Res., 80*, 1093–1098.

Keller, G.R., L.W. Braile, and J.W. Schlue (1979). Regional crustal structure of the Rio Grande rift from surface wave dispersion measurements, in *Rio Grande Rift: Tectonics and Magmatism,* edited by R.E. Riecker, AGU, Washington, D.C., 115–126.

Kennet, B.L.N. (1983). *Seismic Wave Propagation in Stratified Media*, Cambridge University Press, Cambridge England, 342pp.

Kent, G.M., A.J. Harding and J.A. Orcutt (1990). Evidence for a smaller magma chamber beneath the East Pacific Rise at 9°30'N, *Nature, 344*, 650–653.

Klein, F.W., R.Y. Koyanagi, J.S. Nataka, and W.R. Tanigawa (1987). The seismicity of Kilauea's magma system, *U.S. Geol. Surv. Prof. Pap., 1350*, 1019–1186.

Lachenbruch, A.H. and J.H. Sass (1977). Heat flow in the United States and thermal regime of the crust, in *The Earth's Crust, Geophys. Mono. 20*, edited by J.G. Heacock, AGU, Washington, D.C., 626–675.

Langston, C.A. (1977a). Corvallis, Oregon, crustal and upper mantle receiver structure from teleseismic P and S waves, *Bull. Seismol. Soc. Am., 67,* 713–724.

Langston, C.A. (1977b). The effect of planar dipping structure on source and receiver responses for constant ray parameter, *Bull. Seismol. Soc. Am., 67,* 1029–1050.

Langston, C.A. (1979). Structure under Mount Rainier, Washington, inferred from teleseismic body waves, *J. Geophys Res., 84,* 4749–4762.

Louden, K.E., R.S. White, C.G. Potts, and D.W. Forsyth (1986). Structure and seismotectonics of the Vema Fracture Zone, Atlantic Ocean, *J. Geol. Soc. London, 143,* 795–806.

MacDonald, G.A. (1972). *Volcanoes,* Prentice–Hall, Englewood Cliffs, New Jersey, 510pp.

Machado, F. (1974). The search for magmatic reservoirs, in *Physical Volcanology,* edited by L. Civetta, P. Gasparini, G. Luongo and A. Rapolla, Developments in Solid Earth Geophysics, 6, Elsevier Scientific Publ. Co., Amsterdam, 255–273.

Mevel, C. (1987). Evolution of oceanic gabbros from DSDP leg 82: Influence of the fluid phase on metamorphic crystallizations, *Earth Planet Sci. Lett., 83,* 67–79.

Morgan P. (1982). Heat flow in rift zones, in *Continental and Oceanic Rifts, Geodynamics Series, Vol. 8,* AGU, Washington, D.C., 107–122.

Olsen, K.H. (1983). The role of seismic refraction data for studies of the origin and evolution of continental rifts, *Tectonophysics, 94,* 349–370.

Olsen, K.H., G.R. Keller and J.N. Stewart (1979). Crustal Structure along the Rio Grande rift from seismic refraction profiles, in *Rio Grande Rift: Tectonics and Magmatism,* edited by R.E. Riecker, AGU, Washington, D.C., 127–144.

Olsen, K.H., W.S. Baldridge, and J.F. Callender (1987). Rio Grande rift: an overview, *Tectonophysics, 143,* 119–139.

Owens, T.J. (1984). Determination of crustal and upper mantle structure from analysis of broadband teleseismic P waveforms, *Ph.D. Dissertation,* University of Utah, Salt Lake City, Utah, 146pp.

Owens, T.J., G. Zandt, and S.R. Taylor (1984). Seismic evidence for an ancient rift beneath the Cumberland Plateau, Tennessee: A detailed analysis of broad-band teleseismic P waveforms, *J. Geophys Res., 89*, 7783–7795.

Reasenberg, P., W. Ellsworth, and A. Walter (1980). Teleseismic evidence for a low–velocity body under the Coso geothermal area, *J. Geophys. Res., 85*, 2471–2483.

Reilinger, R., J. Oliver, L. Brown, A. Sanford, and E. Balazs (1980). New measurements of crustal doming over the Socorro magma body, New Mexico, *Geology, 8*, 291–295.

Reiter, M., C.L. Edwards, H. Harmon, and C. Weidman (1975). Terrestrial heat flow along the Rio Grande rift, New Mexico and southern Colorado, *Geol. Soc. Am. Bull., 86*, 811–818.

Reiter, M, C. Shearer, and C.L. Edwards (1978). Geothermal anomalies along the Rio Grande rift in New Mexico, *Geology, 6*, 85–88.

Reiter, M., A. Mansure, and C. Shearer (1979). Geothermal characteristics of the Rio Grande rift within the southern Rocky Mountain complex, in *Rio Grande Rift: Tectonics and Magmatism,* edited by R.E. Riecker, AGU, Washington, D.C., 253–267.

Rinehart, E.J. (1979). The determination of an upper crustal model for the Rio Grande rift near Socorro, New Mexico, employing S–wave reflections produced by local micoearthquakes, *Ph.D. Thesis*, New Mexico Tech, Socorro, New Mexico, 207pp.

Rinehart, E.J. and A.R. Sanford (1981). Upper crustal structure of the Rio Grande rift near Socorro, New Mexico, from inversion of microearthquake S–wave reflections, *Bull. Seismol. Soc. Am., 71*, 437–450.

Rinehart, E.J., A.R. Sanford, and R.M. Ward (1979). Geographic extent and shape of an extensive magma body at mid–crustal depths in the Rio Grande rift near Socorro, New Mexico, in *Rio Grande Rift: Tectonics and Magmatism,* edited by R.E. Riecker, AGU, Washington, D.C., 237–251.

Roller, J.C. (1965). Crustal structure in the eastern Colorado Plateau province from seismic refraction measurements, *Bull. Seismol. Soc. Am., 55*, 107–119.

Ryan, M.P. (1988). The mechanics and three–dimensional internal structure of active magmatic systems: Kilauea Volcano, Hawaii, *J. Geophys. Res., 93,* 4213–4248.

Sanford, A.R. (1983). Magma bodies in the Rio Grande rift in central New Mexico, *New Mexico Geological Society 34th Annual Field Conference Guidebook,* 123–125.

Sanford, A.R. and P. Einarsson (1982). Magma chambers in rifts, in *Continental and Oceanic Rifts, Geodynamics Series, Vol. 8,* AGU, Washington, D.C., 147–168.

Sanford, A.R., K.H. Olsen, and L.H. Jaksha (1979) Seismicity of the Rio Grande rift, in *Rio Grande Rift: Tectonics and Magmatism,* edited by R.E. Riecker, AGU, Washington, D.C., 87–106.

Sanford, A.R., O. Alptekin, and T.R. Topozada (1973). Use of reflection phases on microearthquake seismograms to map an unusual discontinuity beneath the Rio Grande rift, *Bull. Seismol. Soc. Am., 63,* 2021–2034.

Sanford, A.R., R.P.Mott, P.J. Shuleski, E.J. Rinehart, F.J. Caravella, R. M. Ward, and T.C. Wallace (1977). Geophysical evidence for a magma body in the vicinity of Socorro, New Mexico, in *The Earth's Crust: Its Nature and Physical Properties, Geophys. Monogr. Ser., Vol. 20,* edited by J.G. Heackock, AGU, Washington, D.C., 385–404.

Sato, H., I.S. Sacks, T. Murase, and C.M. Scarfe (1988). Thermal structure of the low velocity zone derived from laboratory and seismic investigations, *Geophys. Res. Lett., 11,* 1227–1230.

Schlue, J.W., P.J. Singer and C.L. Edwards (1986). Shear wave structure of the upper crust of the Albuquerque–Belen basin from Rayleigh wave phase velocities, *J. Geophys. Res., 91.* 6277–6281.

Sengor, A.M.C. and K. Burke (1978). Relative timing of rifting and volcanism on Earth and its tectonic implications, *Geophys. Res. Lett., 5,* 419–421.

Singer, P.J. (1989). Crustal structure of the Socorro area of the Rio Grande rift from time–term analysis, *Ph.D. Dissertation,* New Mexico Tech, Socorro, New Mexico, 206pp.

Sinno, Y.A., G.R. Keller, and M.L. Shar (1981). A crustal seismic refraction study in west–central Arizona, *J. Geophys. Res., 86,* 5023–5038.

Sinno, Y.A., P.H. Daggett, G.R. Keller, P. Morgan and S.H. Harder (1986). Crustal structure of the southern Rio Grande rift determined from seismic refraction profiling, *J. Geophys. Res., 91,* 6143–6156.

Sinton, J.M. and R.S. Detrick (1992). Mid–ocean ridge magma chambers, *J. Geophys. Res., 97,* 197–216.

Sinton, J.M., S.M. Smoglik, J.J. Mahoney and K.C. MacDonald (1991). Magmatic processes at superfast spreading ocean ridges: Glass compositional variations along the East Pacific Rise, 13°–23°S, *J. Geophys. Res., 96,* 6133–6155.

Sleep, N.H. (1975). Formation of oceanic crust: Some thermal constraints, *J. Geophys. Res., 80,* 4037–4042.

Sleep, N.H. (1978). Thermal structure and kinematics of mid–ocean ridge axis, some implications to basaltic volcanism, *Geophys. Res. Lett., 5, 425–428.*

Solomon, S.C. (1973). Shear wave attenuation and melting beneath the Mid–Atlantic ridge, *J. Geophys. Res., 78,* 6044–6059.

Stewart, S.W. and L.C. Pakiser (1962). Crustal structure in eastern New Mexico interpreted from the GNOME explosion, *Bull. Seismol. Soc. Am., 52,* 1017–1030.

Toomey, D.R., G.M. Purdy, and S.C. Solomon (1989). Three–dimensional structure of the East Pacific Rise at 9°30′N, *EOS Trans AGU, 70,* 1317.

Toomey, D.R., S.C. Solomon, and G.M. Purdy (1988). Microearthquakes beneath the median valley of the Mid–Atlantic ridge near 23°N: Tomography and tectonics, *J. Geophys. Res., 93,* 9093–9112.

Toomey, D.R., G.M. Purdy , S.C. Solomon, and W. Wilcox (1990). The three dimensional seismic velocity structure of the East Pacific Rise near lattitude 9°30′N, *Nature, 347,* 639–644.

Toomey, D.R, S.C. Solomon, G.M. Purdy, and M.H. Murray (1985). Microearthquakes beneath the median valley of the Mid–Atlantic ridge near 23°N: Hypocenters and focal mechanisms, *J. Geophys. Res., 90,* 5443–5458.

Toppozada, T.R. and A.R. Sanford (1976). Crustal structure in central New Mexico interpreted from the GASBUGGY explosion, *Bull. Seismol. Soc. Am., 66,* 877–886.

Turcotte, D.L. (1982). Magma migration, *Ann. Rev. Earth Planet Sci., 10,* 397–408.

Vera, E.E., P. Buhl, J.C. Mutter, A.J. Harding, J.A. Orcutt, and R.S. Detrick (1990). The structure of 0–0.2 My old oceanic crust at 9°N in the East Pacific Rise from expanded spread profiles, *J. Geophys. Res., 95,* 15529–15556.

Wong, I.G., D.J. Cash, and L.H. Jaksha (1984). The Crownpoint, New Mexico earthquakes of 1976 and 1977, *Bull. Seismol. Soc. Am., 74,* 2435–2449.

APPENDIX A

This appendix displays the raw seismograms containing the P−waveform of the events used for this study. It is divided into three sections: southeast data, south data and northwest data. Each section begins with a table which provides information on each seismogram in the section.

TABLE OF CONTENTS:

SOUTHEAST DATA

This section shows the raw teleseismic P–waveforms for two groups of events from the southeast. Group 1 consists of three events and group 2 consists of four events. The two groups are separated by distance within the same backazimuth cluster. Table A1 provides information on the origin time as well as the times corresponding to the 120 second window of data displayed for each event.

TABLE A1. Event Information and P-waveform Isolation Times for the Southeast Data

Event Information			120 sec P-waveform Record		
I.D.	Date*	Origin Time*	Page	Start Time	Cut Interval**
		CLUSTER 1			
15090	30 May 90	02:34:05.8	A3	02:42:20.736	2990–3110
32790	23 Nov 90	22:35:34.7	A4	22:42:36.795	0348–0468
09591	05 Apr 91	04:19:49.5	A5	04:28:05.908	3095–3225
		CLUSTER 2			
28390	10 Oct 90	01:00:05.5	A6	01:09:51.773	0059–0179
14491	24 May 91	20:50:55.8	A7	21:00:27.385	1013–1233
17491	23 Jun 91	21:22:28.9	A8	21:32:36.418	2823–2943
18791	06 Jul 91	12:19:49.5	A9	02:28:59.974	2457–2577

* From U.S. Geological Survey Preliminary Determination of Epicenters Monthly Listings.
** In seconds; for use with intrinsic "cut" command in Seismic Analysis Code (SAC).

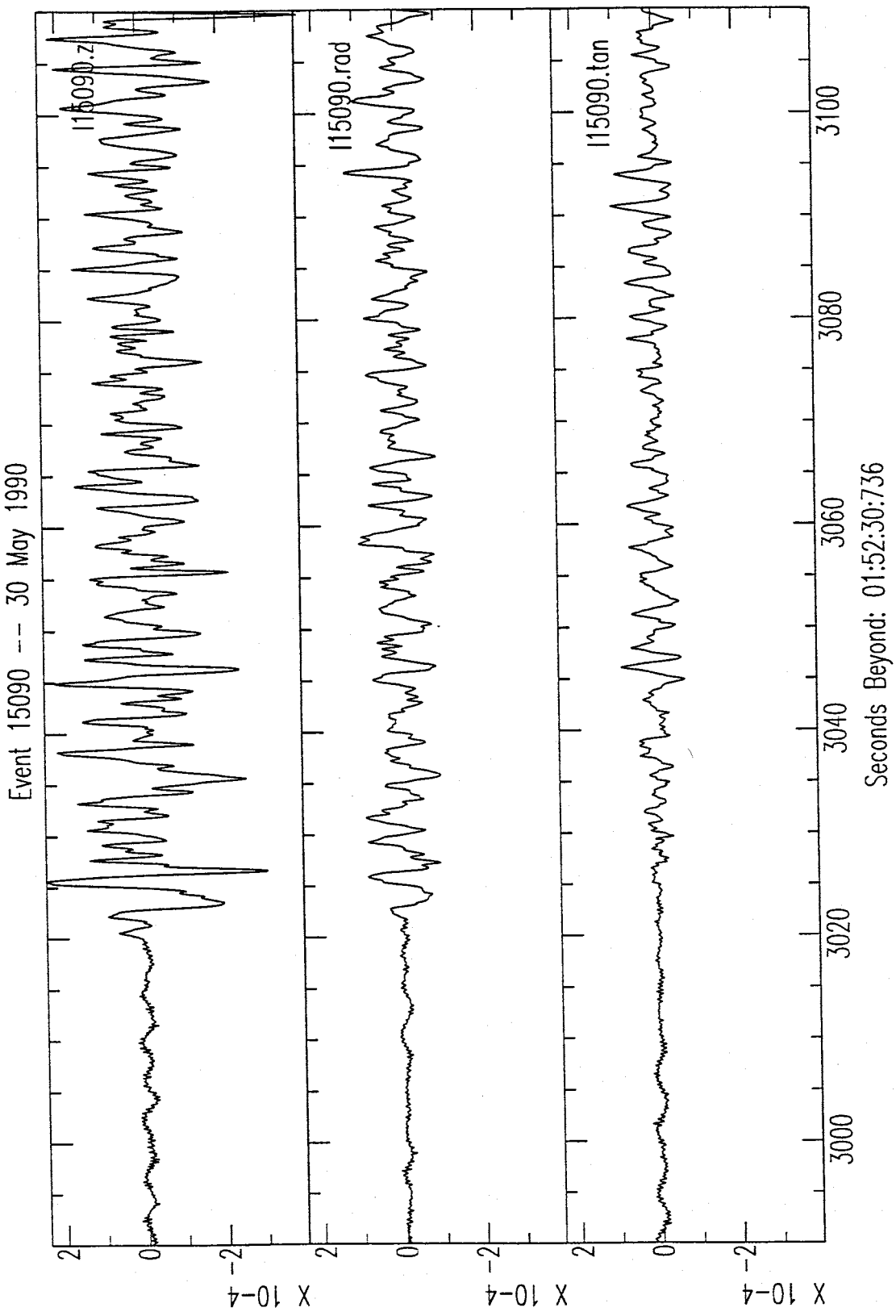
Event 15090 -- 30 May 1990
I15090.z
I15090.rad
I15090.tan
X 10-4
2
0
-2
3000
3020
3040
3060
3080
3100
Seconds Beyond: 01:52:30:736

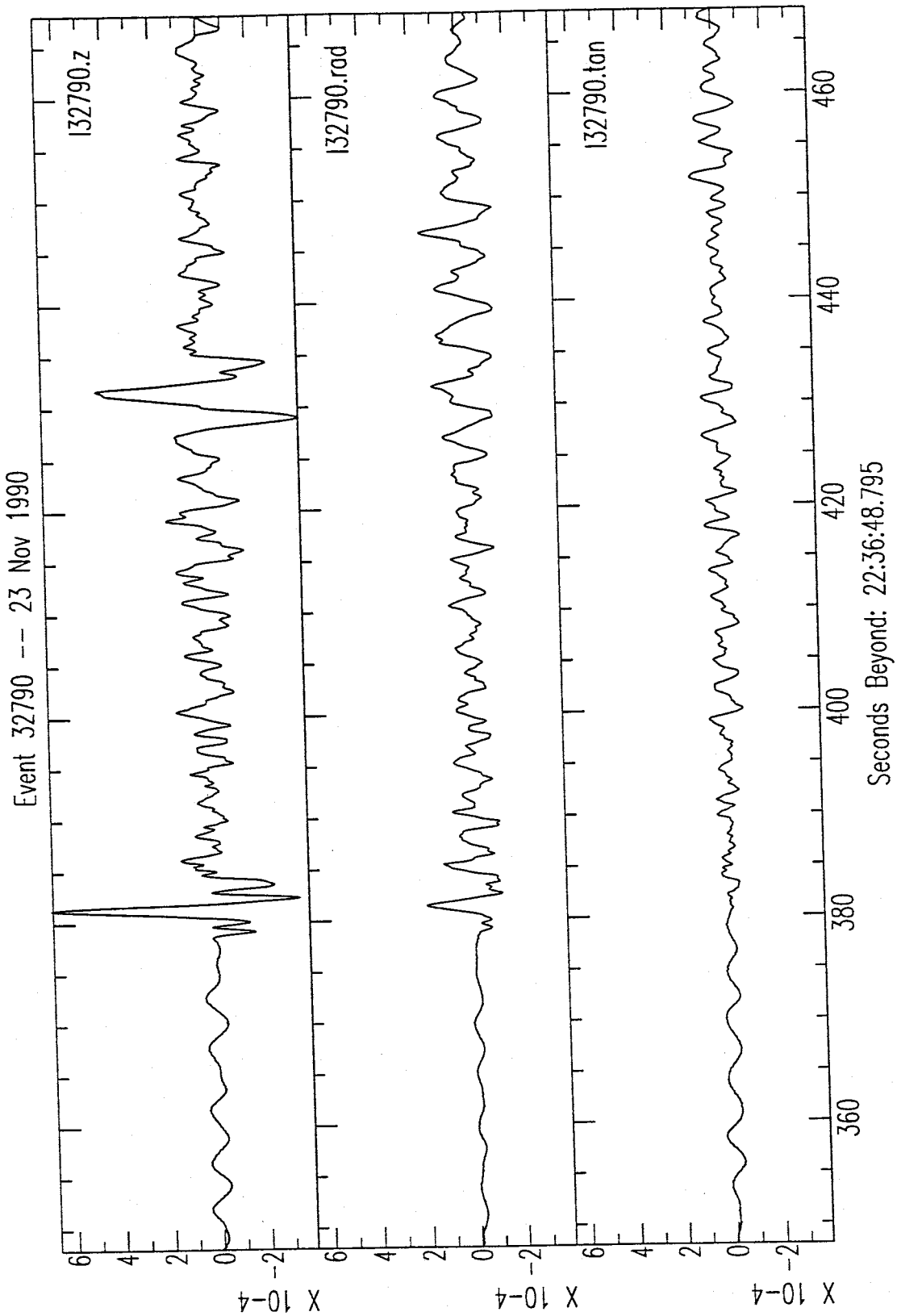
Event 32790 -- 23 Nov 1990
132790.z
132790.rad
132790.tan
X 10-4
6
4
2
0
-2
360
380
400
420
440
460
Seconds Beyond: 22:36:48.795

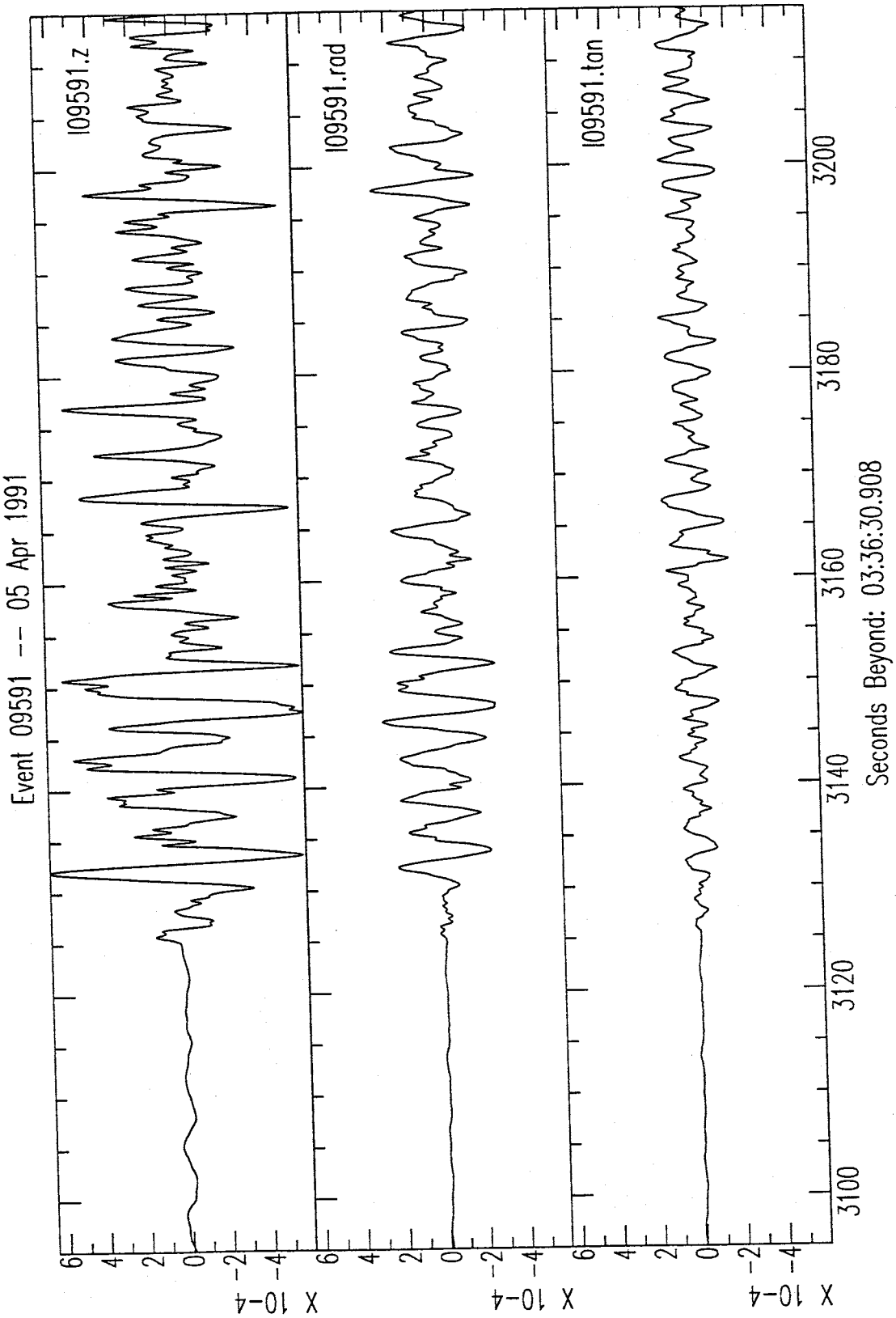
Event 09591 -- 05 Apr 1991
I09591.z
I09591.rad
I09591.tan
X 10-4
6
4
2
0
-2
-4
3100
3120
3140
3160
3180
3200
Seconds Beyond: 03:36:30.908

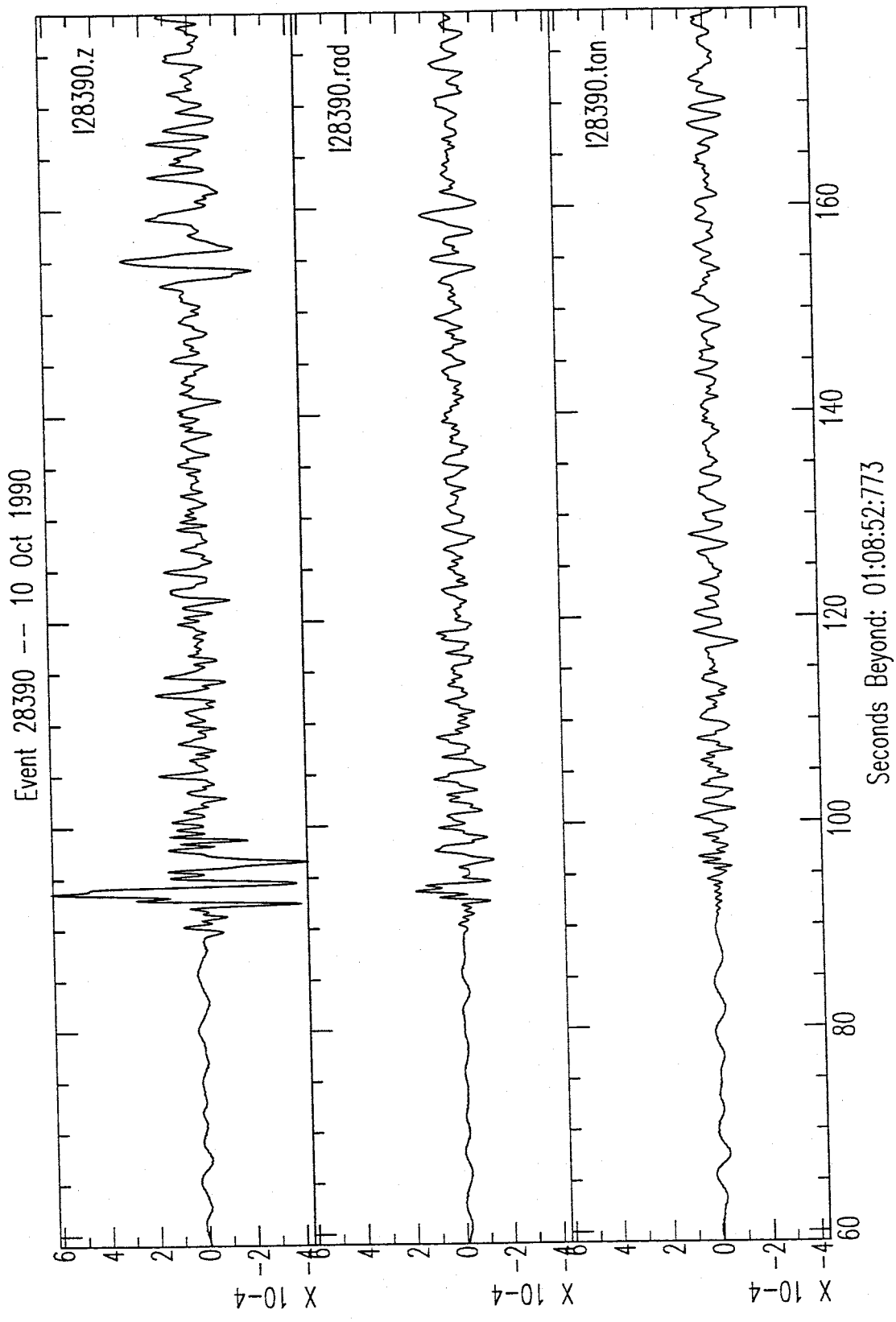
Event 28390 -- 10 Oct 1990
128390.z
128390.rad
128390.tan
X 10-4
Seconds Beyond: 01:08:52:773

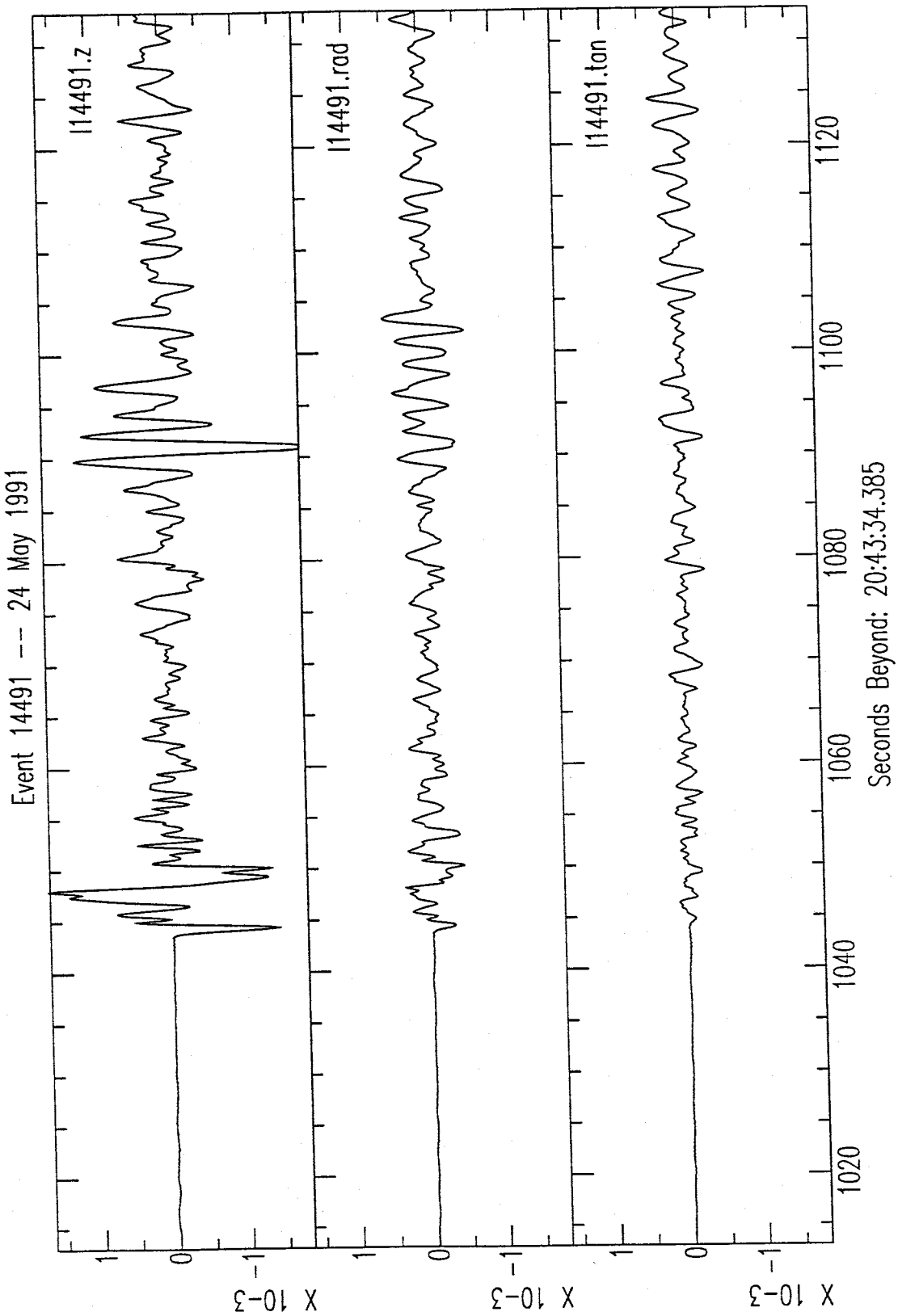
Event 14491 -- 24 May 1991
I14491.z
I14491.rad
I14491.tan
X 10-3
1020
1040
1060
1080
1100
1120
Seconds Beyond: 20:43:34.385

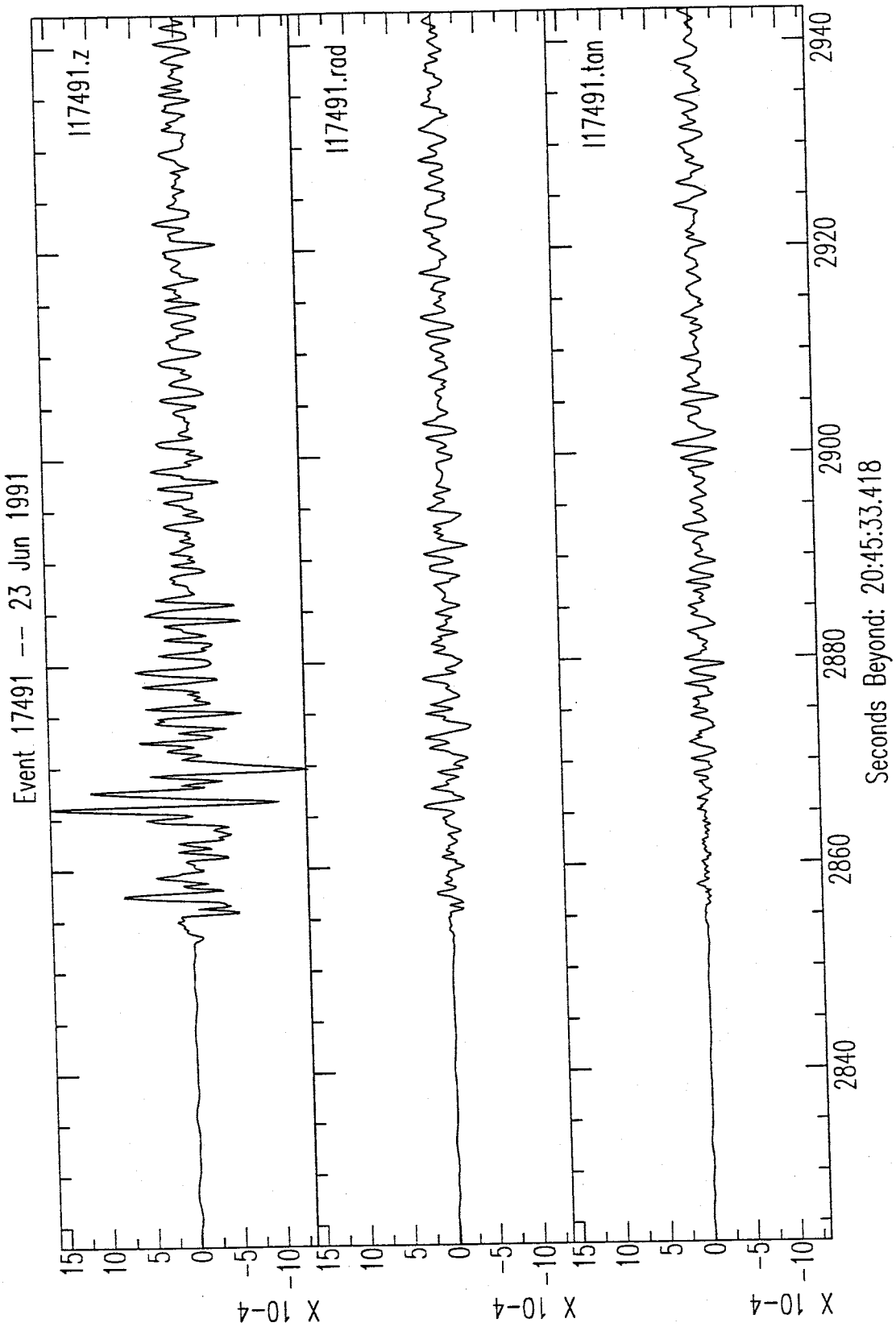
Event 17491 -- 23 Jun 1991
I17491.z
I17491.rad
I17491.tan
X 10-4
15
10
5
0
-5
-10
2840
2860
2880
2900
2920
2940
Seconds Beyond: 20:45:33.418

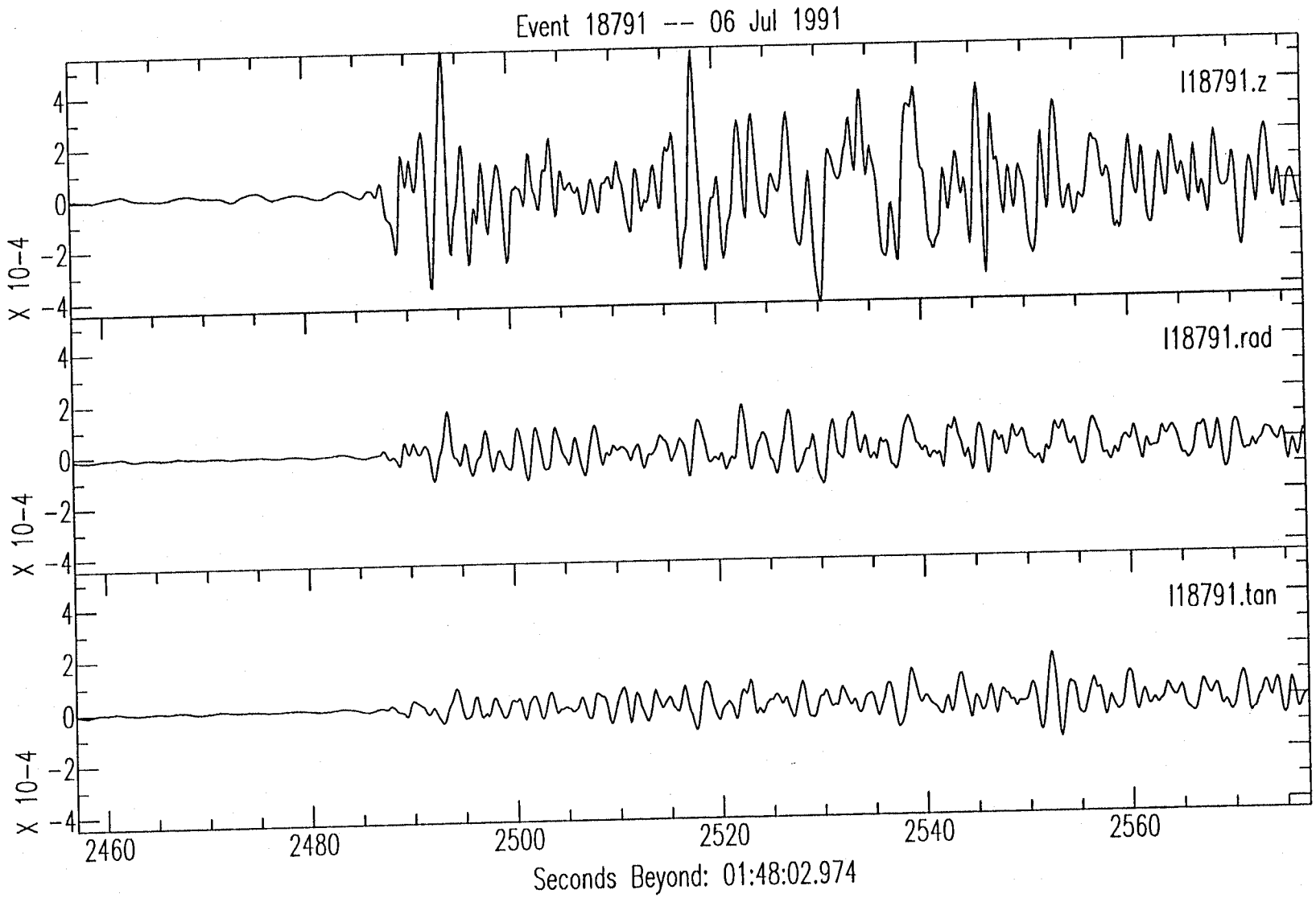
Event 18791 -- 06 Jul 1991
I18791.z
I18791.rad
I18791.tan
X 10-4
4
2
0
-2
-4
2460
2480
2500
2520
2540
2560
Seconds Beyond: 01:48:02.974

SOUTH DATA

This section shows the raw teleseismic P−waveforms for the three events from the south. Table A2 provides information on the origin time as well as the times corresponding to the 120 second window of data displayed for each event.

TABLE A2. Event Information and P-waveform Isolation Times for the South Data

Event Information			120 sec P-waveform Record		
I.D.	Date*	Origin Time*	Page	Start Time	Cut Interval**
23390	21 Aug 90	14:13:04.8	A11	14:22:51.402	1515-1635
24691a	03 Sep 91	09:05:28.3	A12	09:14:13.309	1202-1322
24691b	03 Sep 91	11:56:16.2	A13	12:05:01.909	0644-0764

* From U.S. Geological Survey Preliminary Determination of Epicenters Monthly Listings

** In seconds; for use with intrinsic "cut" command in Seismic Analysis Code (SAC).

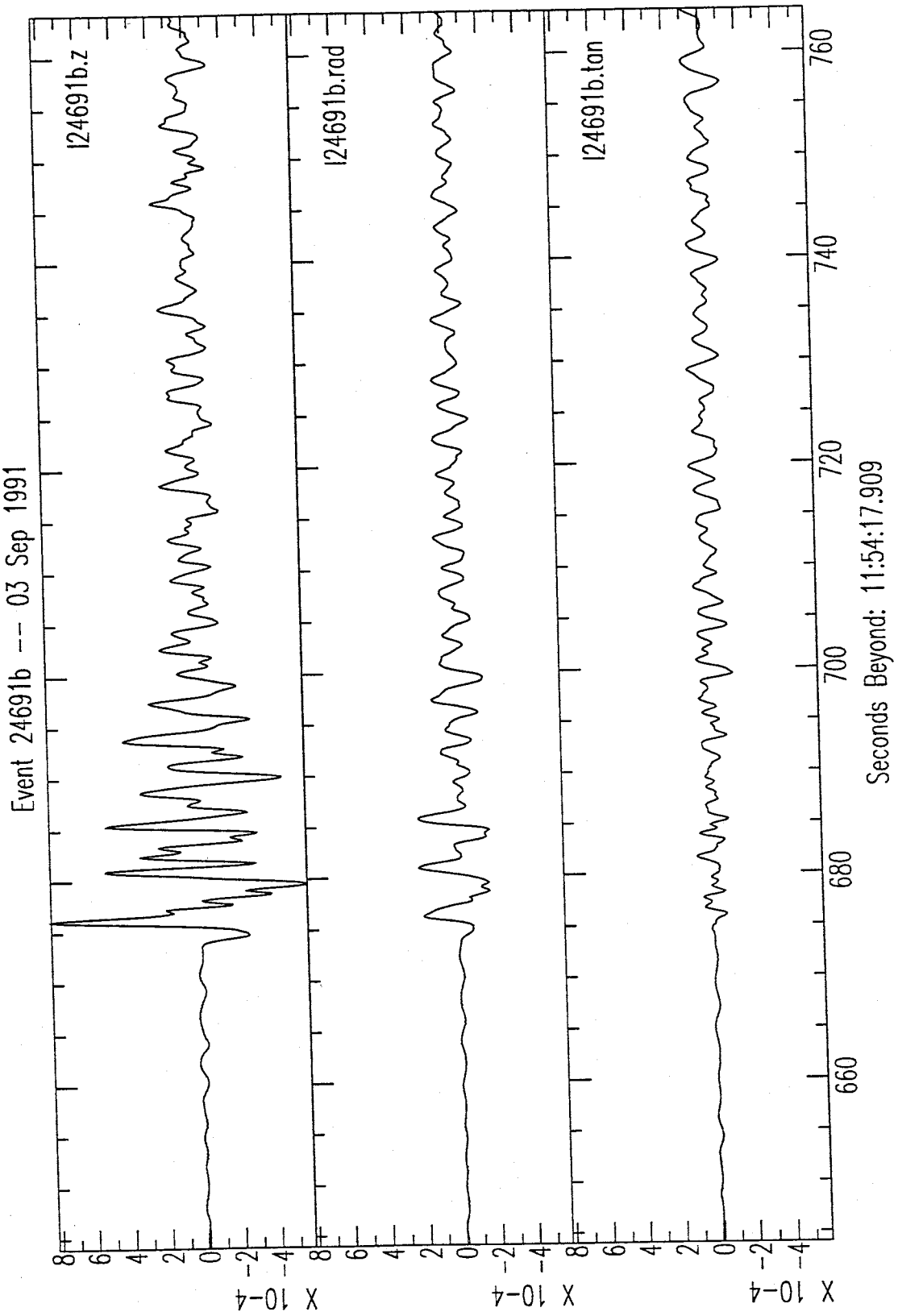
Event 24691b -- 03 Sep 1991
124691b.z
124691b.rad
124691b.tan
X 10-4
8
6
4
2
0
-2
-4
660
680
700
720
740
760
Seconds Beyond: 11:54:17.909

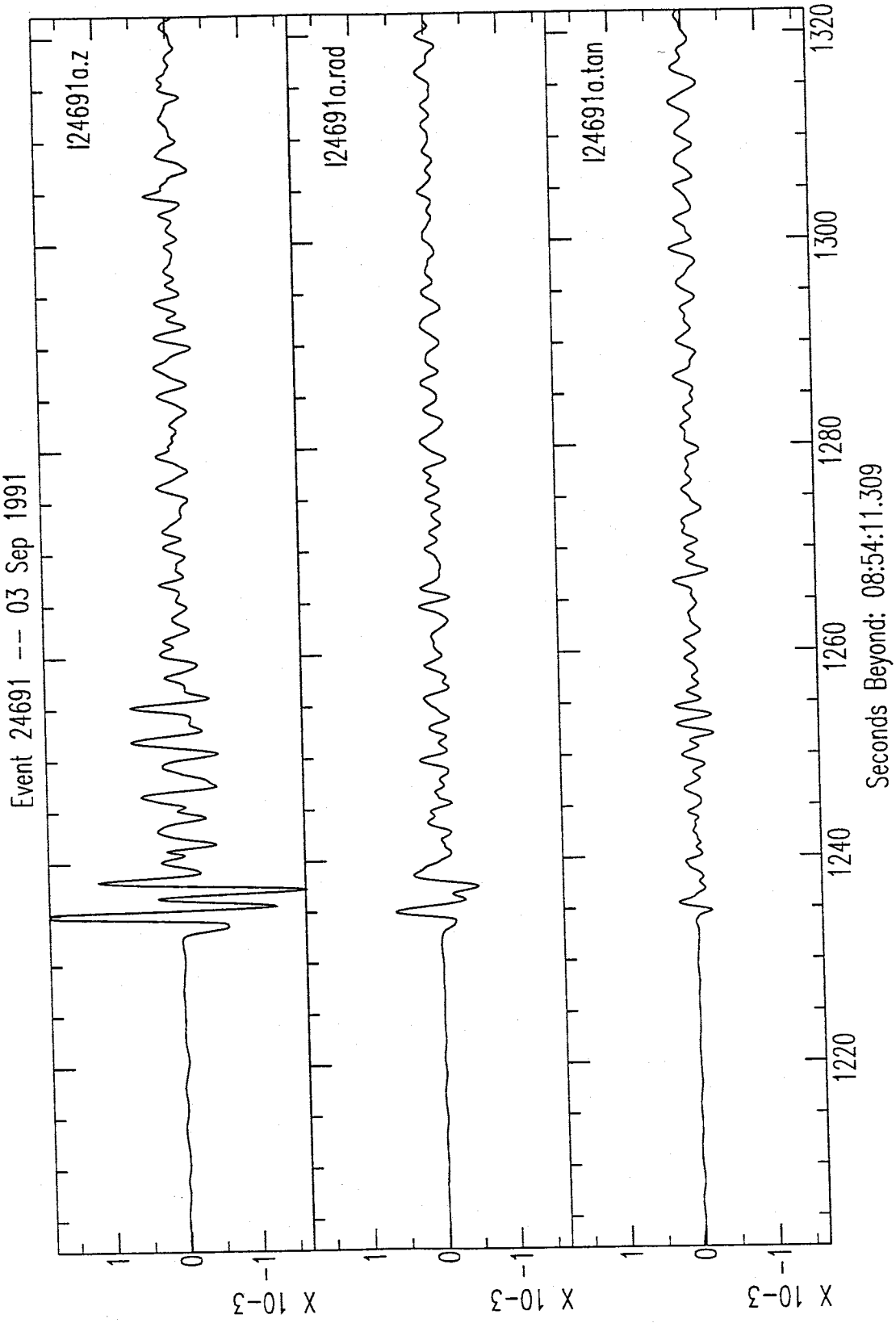
Event 24691 -- 03 Sep 1991
124691a.z
124691a.rad
124691a.tan
X 10-3
1
0
-1
1220
1240
1260
1280
1300
1320
Seconds Beyond: 08:54:11.309

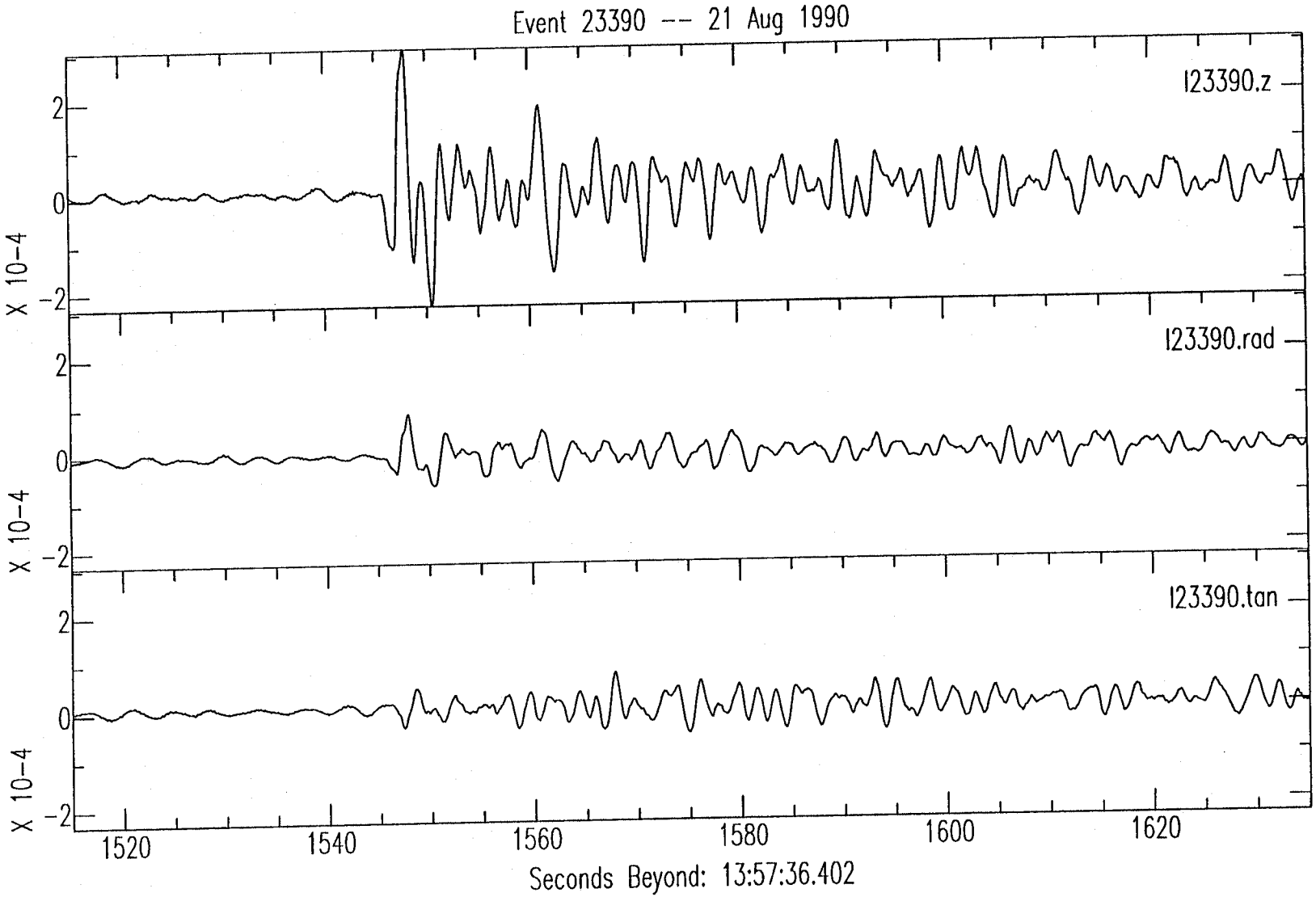
Event 23390 -- 21 Aug 1990
123390.z
123390.rad
123390.tan
X 10-4
2
0
-2
1520
1540
1560
1580
1600
1620
Seconds Beyond: 13:57:36.402

NORTHWEST DATA

This section shows the teleseismic P−waveforms for the four events from the northwest. Table A3 provides information on the origin time as well as the times corresponding to the 120 second window of data displayed for each event.

TABLE A3. Event Information and P-waveform Isolation Times for the Northwest Data

Event Information			120 sec P-waveform Record		
I.D.	Date*	Origin Time*	Page	Start Time	Cut Interval**
32590	21 Nov 90	01:48:26.4	A15	01:56:38.995	1343-1463
05291	21 Feb 91	02:35:34.0	A16	02:44:03.410	2145-2265
06791	08 Mar 91	11:36:28.4	A17	11:46:01.092	3011-3131
15091	30 May 91	13:17:41.9	A18	13:25:11.585	2194-2314

* From U.S. Geological Survey Preliminary Determination of Epicenters Monthly Listings.
** In seconds; for use with intrinsic "cut" command in Seismic Analysis Code (SAC).

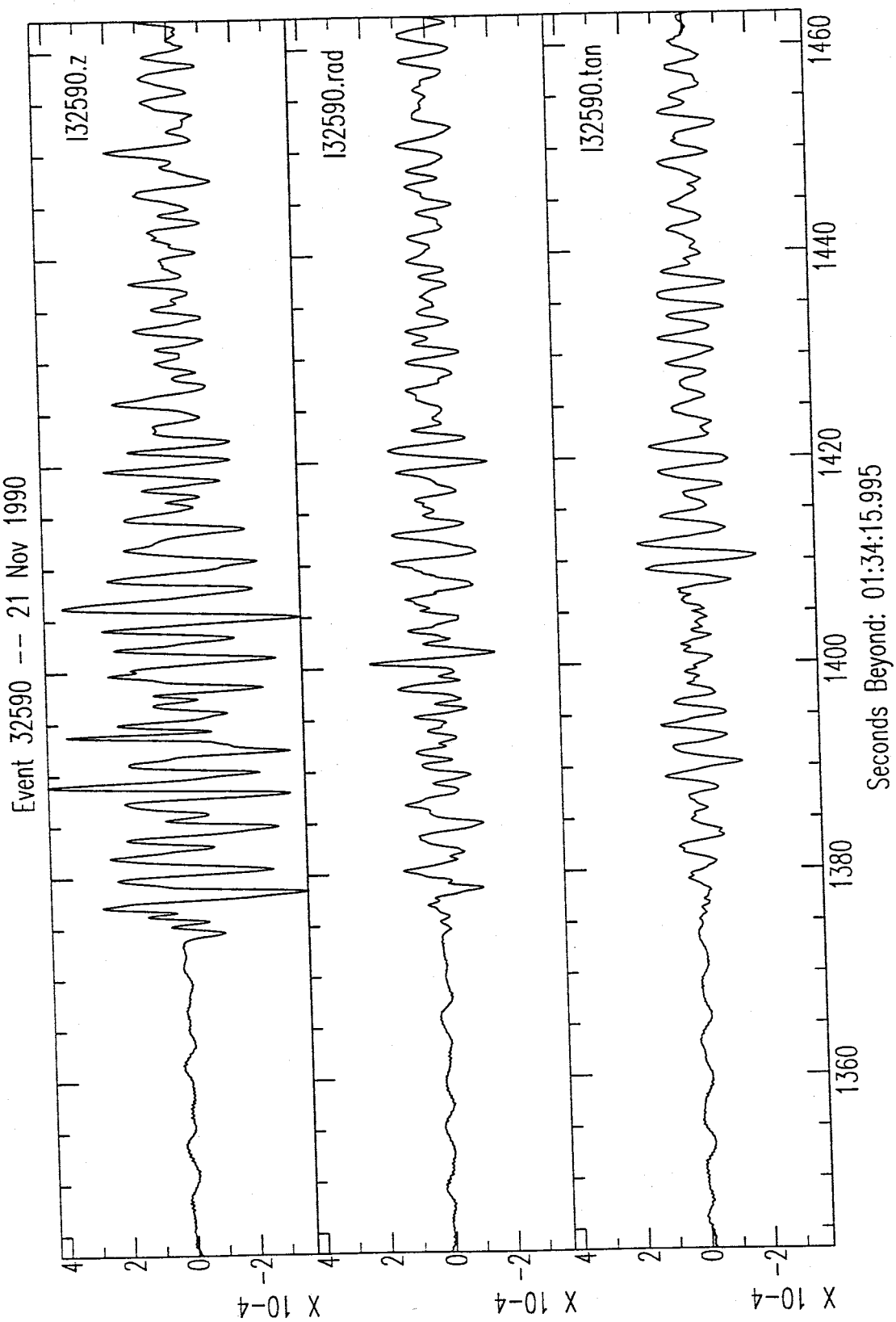
Event 32590 -- 21 Nov 1990
132590.z
132590.rad
132590.tan
X 10-4
4
2
0
-2
1360
1380
1400
1420
1440
1460
Seconds Beyond: 01:34:15.995

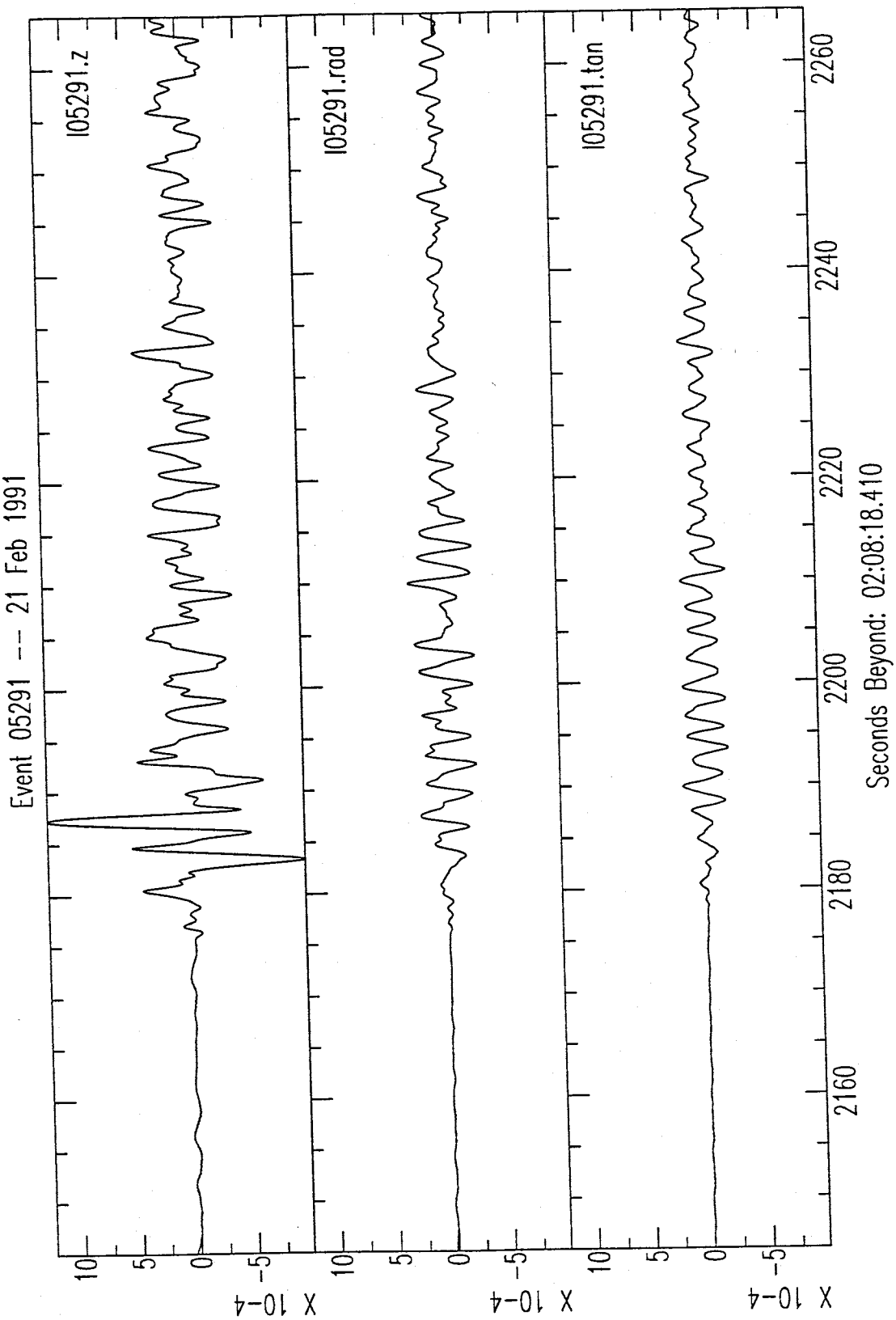
Event 05291 -- 21 Feb 1991
105291.z
105291.rad
105291.tan
X 10-4
10
5
0
-5
2160
2180
2200
2220
2240
2260
Seconds Beyond: 02:08:18.410

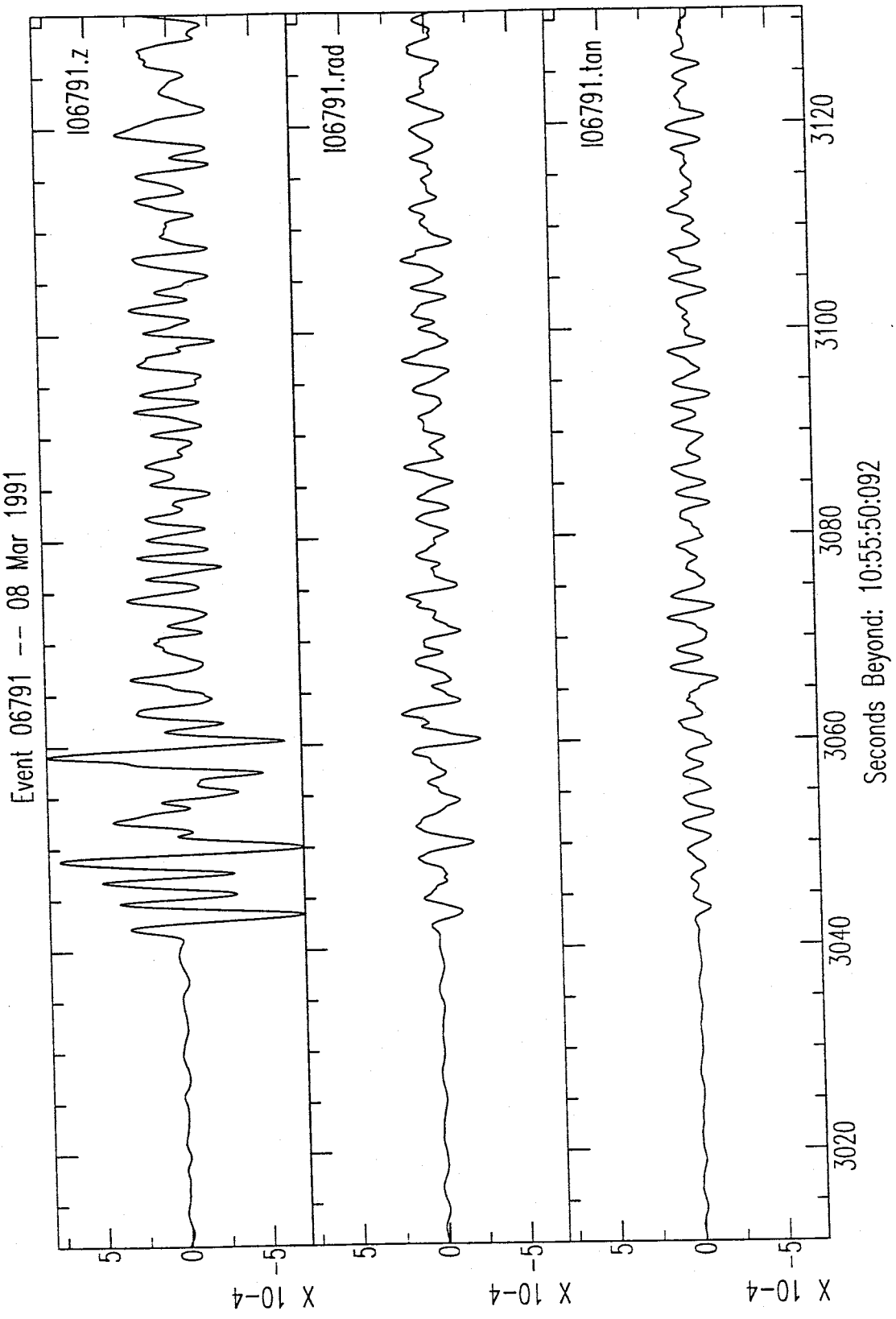
Event 06791 -- 08 Mar 1991
I06791.z
I06791.rad
I06791.tan
X 10-4
5
0
-5
3020
3040
3060
3080
3100
3120
Seconds Beyond: 10:55:50:092

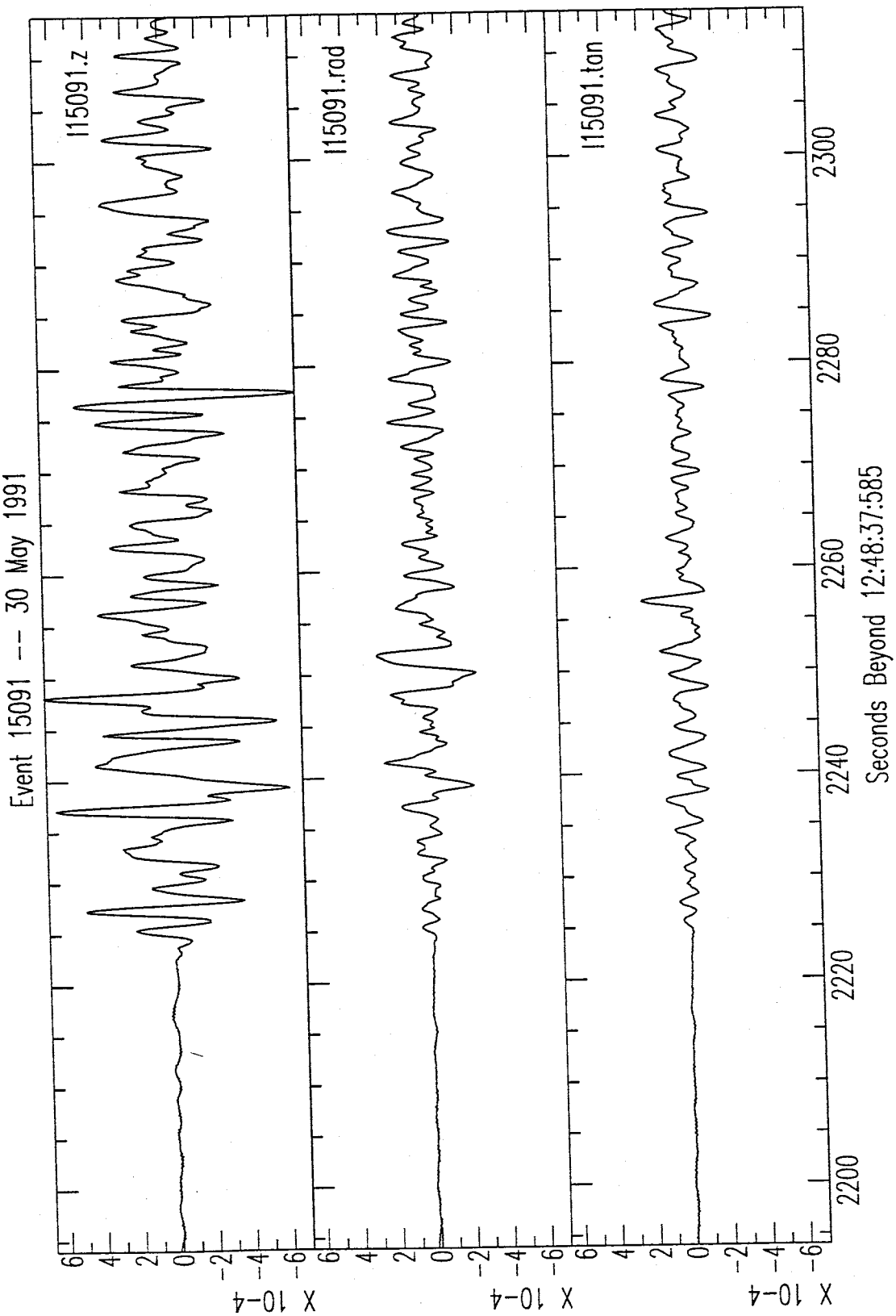
Event 15091 -- 30 May 1991
115091.z
115091.rad
115091.tan
X 10-4
2200
2220
2240
2260
2280
2300
Seconds Beyond 12:48:37:585

APPENDIX B

This appendix displays the radial and tangential receiver functions for each of the events used for this study. It is divided into three sections: southeast data, south data and northwest data. Each section begins with a table which provides information on the receiver functions in the section.

TABLE OF CONTENTS:

SOUTHEAST DATA

This section shows the first forty seconds of the radial and tangential receiver functions for seven events from the southeast. The direct P arrival, marked by the TO line, represents the beginning of the receiver function. The two groups of three and four events (see Appendix A) were combined into one cluster due to their similar radial receiver functions. Table B1 provides information on the deconvolution parameters used in the source equalization of each event.

TABLE B1. Deconvolution Parameters used for Source Equalization of Southeast Data

Event I.D.	Date*	Page	Water-Level Parameter	Gaussian Filter Width
15090	30 May 90	B3	0.01	2.5
28390	10 Oct 90	B4	0.01	2.5
32790	23 Nov 90	B5	0.01	2.5
09591	05 Apr 91	B6	0.01	2.5
14491	24 MAy 91	B7	0.01	2.5
17491	23 Jun 91	B8	0.01	2.5
18791	06 Jul 91	B9	0.01	2.5

* From U.S. Geological Survey Preliminary Determination of Epicenters Monthly Listings.

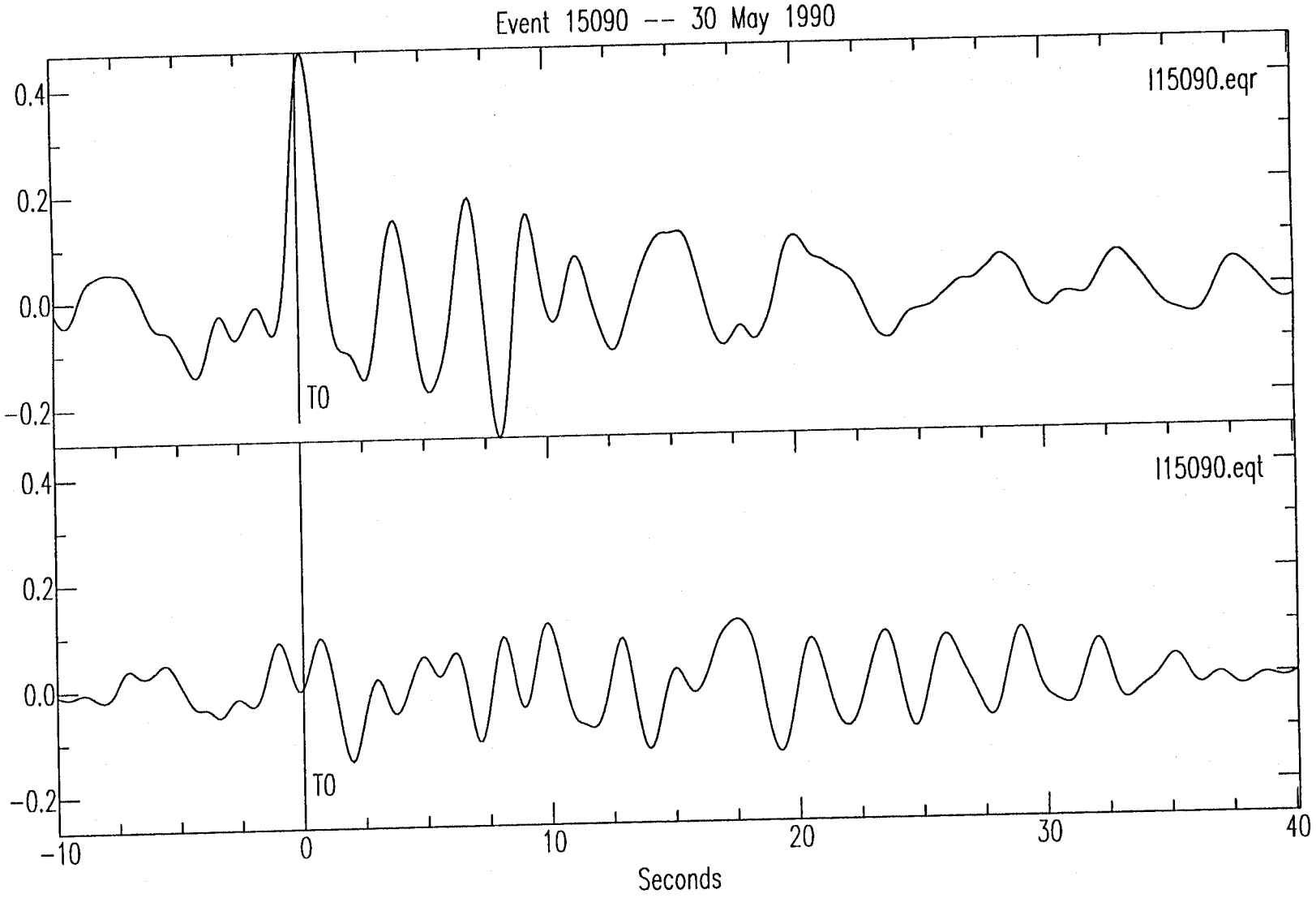
Event 15090 -- 30 May 1990
I15090.eqr
I15090.eqt
0.4
0.2
0.0
-0.2
T0
-10
0
10
20
30
40
Seconds

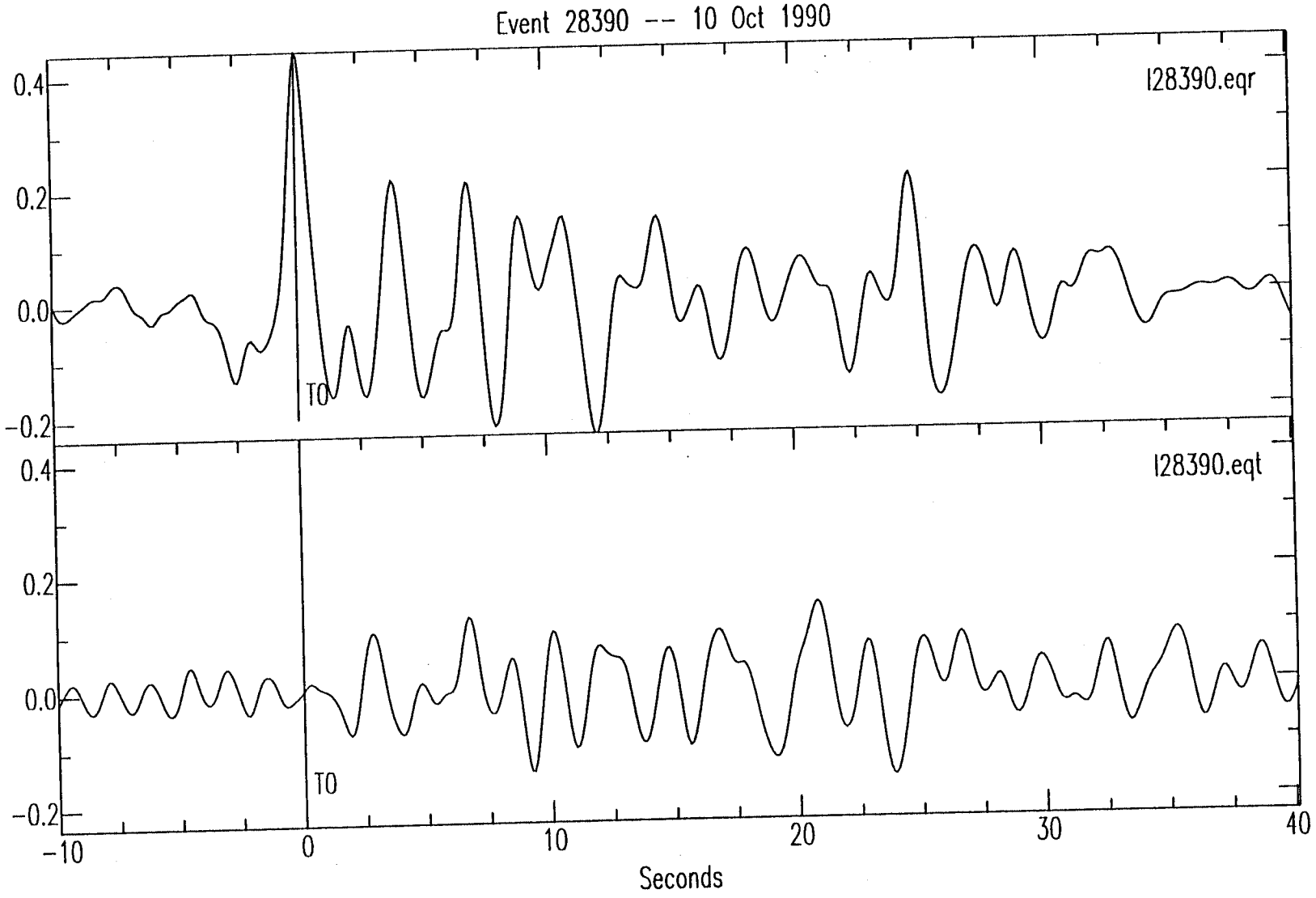
Event 28390 -- 10 Oct 1990
128390.eqr
128390.eqt
0.4
0.2
0.0
-0.2
T0
-10
0
10
20
30
40
Seconds

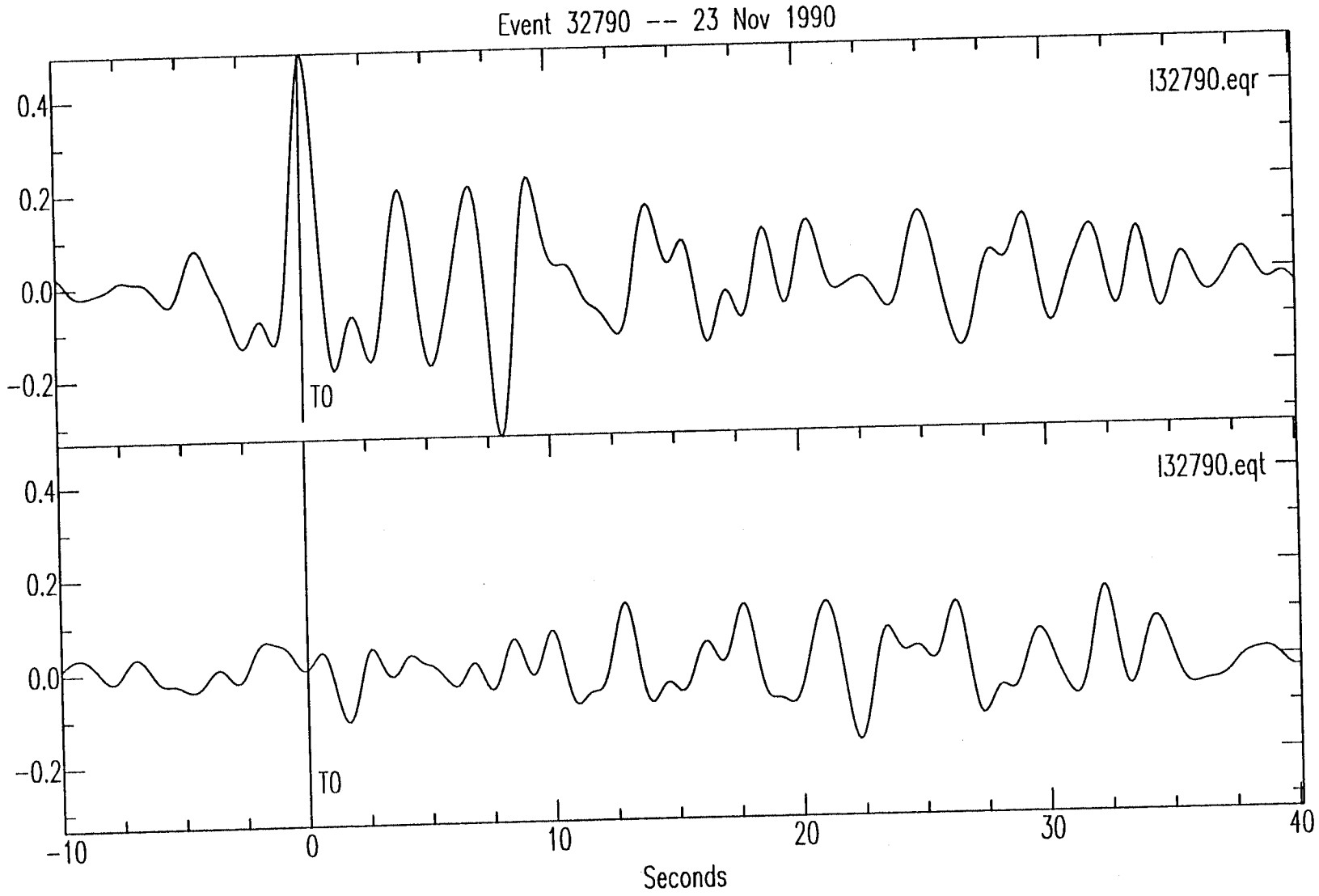
Event 32790 -- 23 Nov 1990
132790.eqr
132790.eqt
0.4
0.2
0.0
-0.2
T0
-10
0
10
20
30
40
Seconds

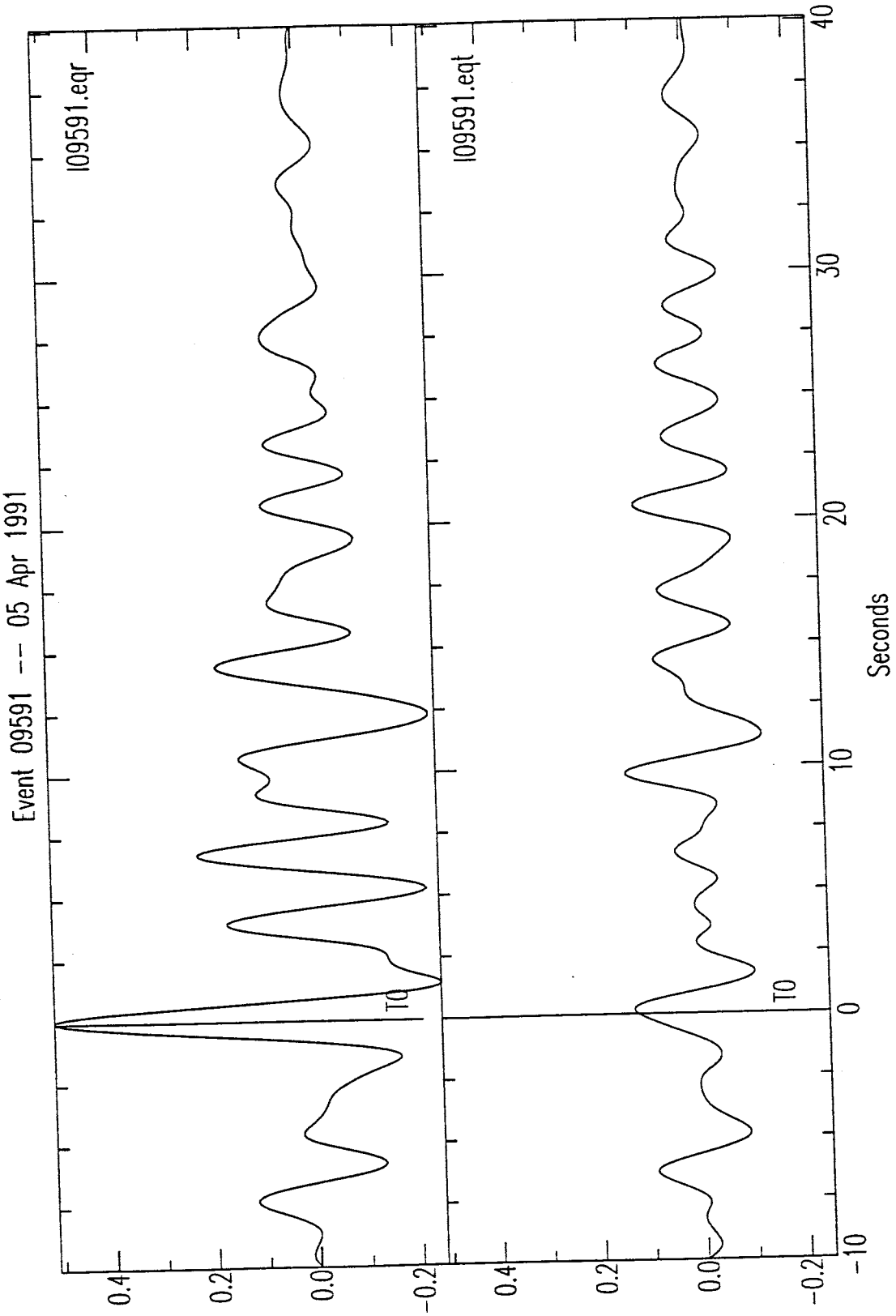
Event 09591 -- 05 Apr 1991
109591.eqr
109591.eqt
TO
TO
0.4
0.2
0.0
-0.2
-10
0
10
20
30
40
Seconds

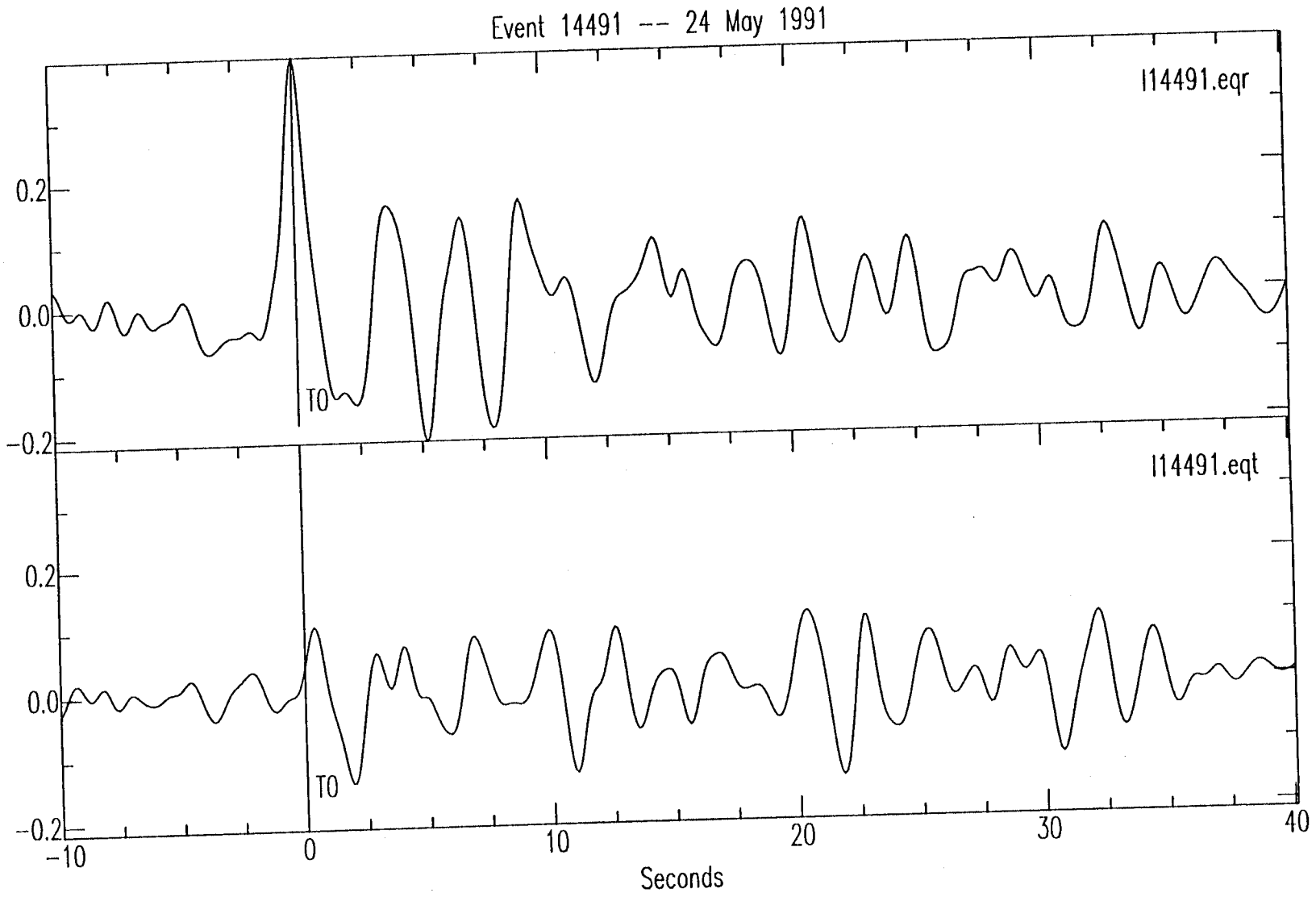
Event 14491 -- 24 May 1991
I14491.eqr
0.2
0.0
-0.2
T0
I14491.eqt
0.2
0.0
-0.2
T0
-10
0
10
20
30
40
Seconds

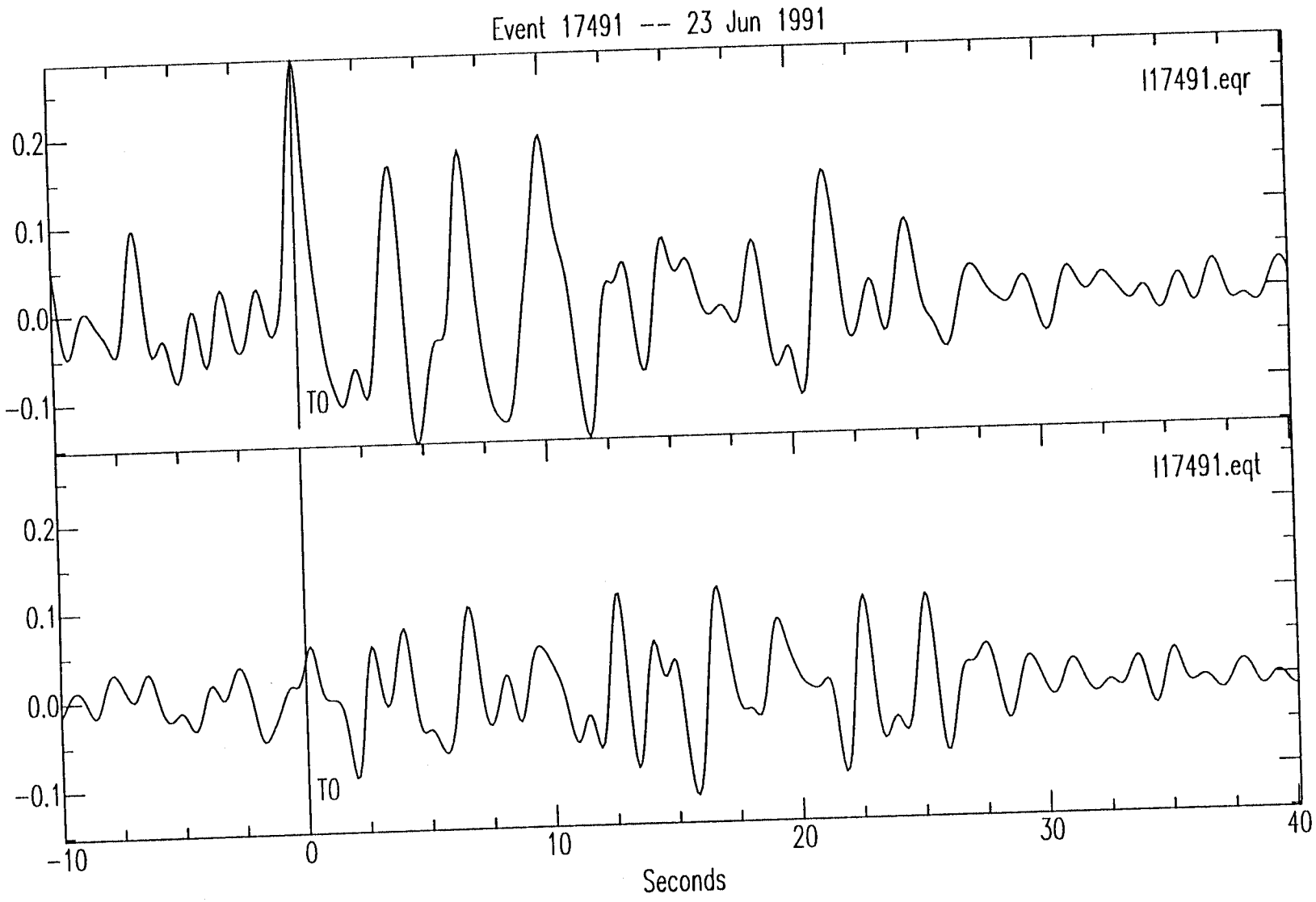
Event 17491 -- 23 Jun 1991
I17491.eqr
I17491.eqt
0.2
0.1
0.0
-0.1
T0
T0
-10
0
10
20
30
40
Seconds

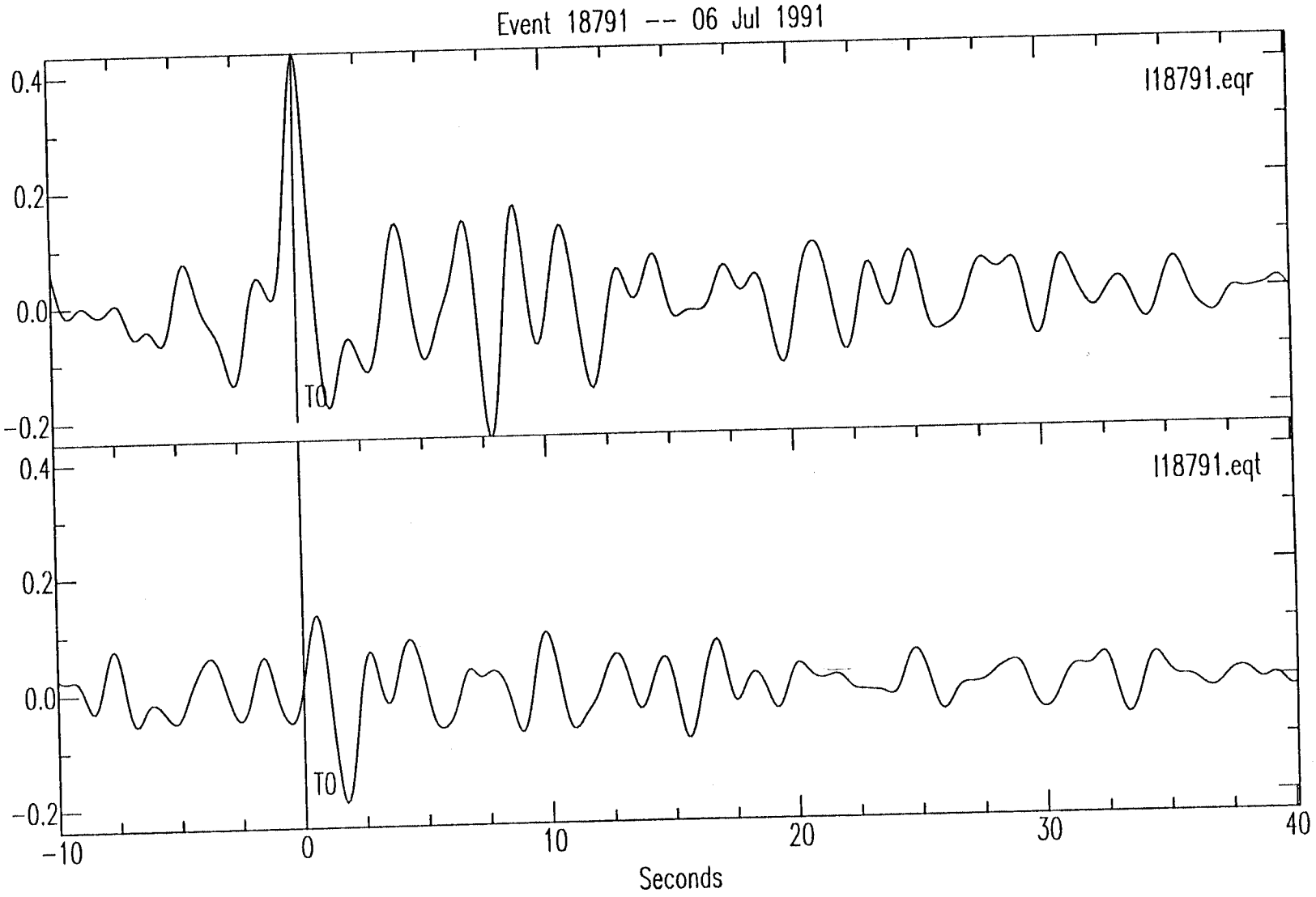
Event 18791 -- 06 Jul 1991
I18791.eqr
I18791.eqt
T0
T0
0.4
0.2
0.0
-0.2
0.4
0.2
0.0
-0.2
-10
0
10
20
30
40
Seconds

SOUTH DATA

This section shows the first forty seconds of the radial and tangential receiver functions for the three events from the south. The direct P arrival, marked by the TO line, represents the beginning of the receiver function. Table B2 provides information on the deconvolution parameters used in the source equalization of each event.

TABLE B2. Deconvolution Parameters used for Source Equalization of South Data

Event I.D.	Date*	Page	Water-Level Parameter	Gaussian Filter Width
23390	21 Aug 90	B11	0.001	2.5
24691a	03 Sep 91	B12	0.001	2.5
24691b	03 Sep 91	B13	0.001	2.5

* From U.S. Geological Survey Preliminary Determination of Epicenters Monthly Listings.

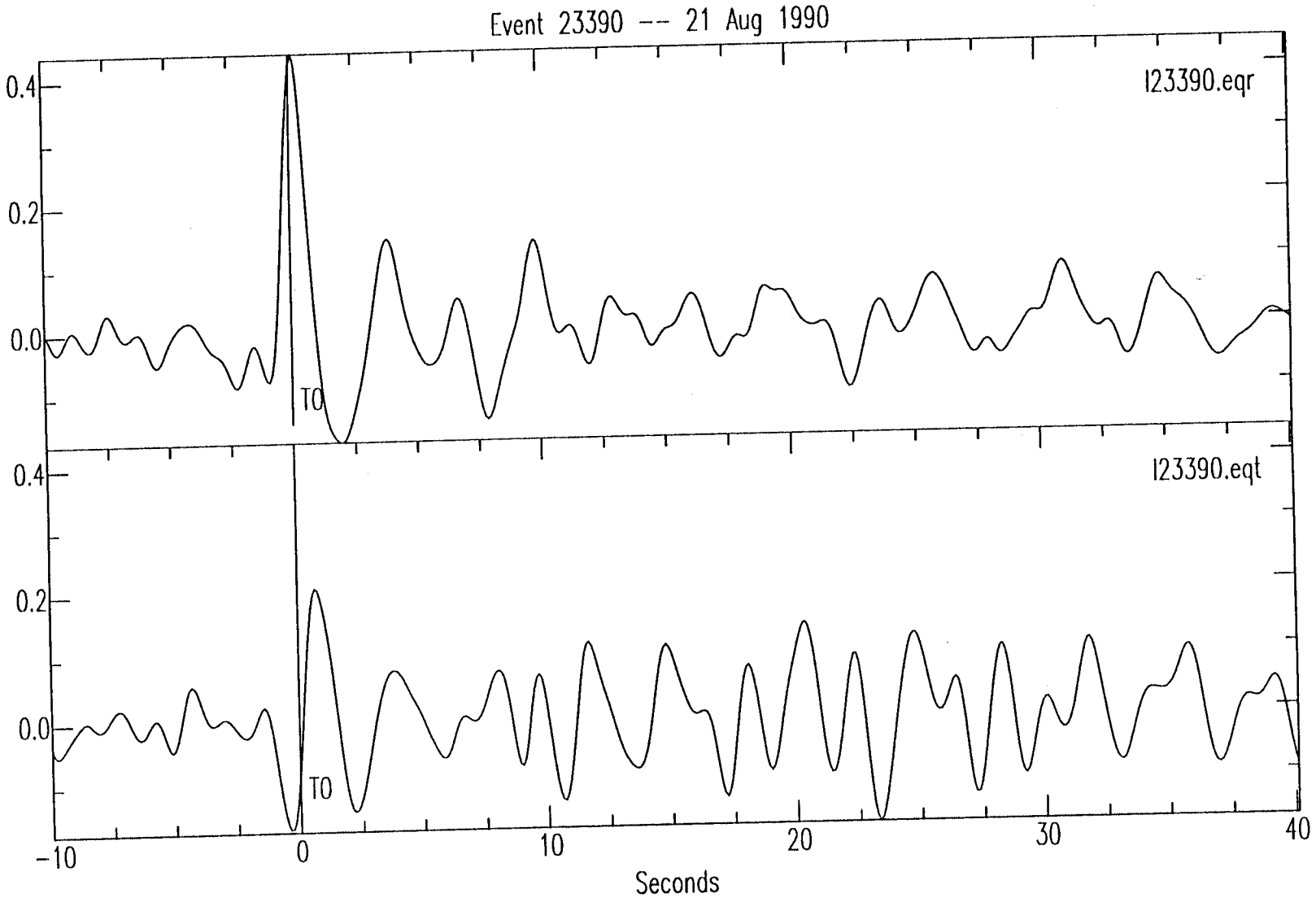
Event 23390 -- 21 Aug 1990
123390.eqr
123390.eqt
0.4
0.2
0.0
T0
-10
0
10
20
30
40
Seconds

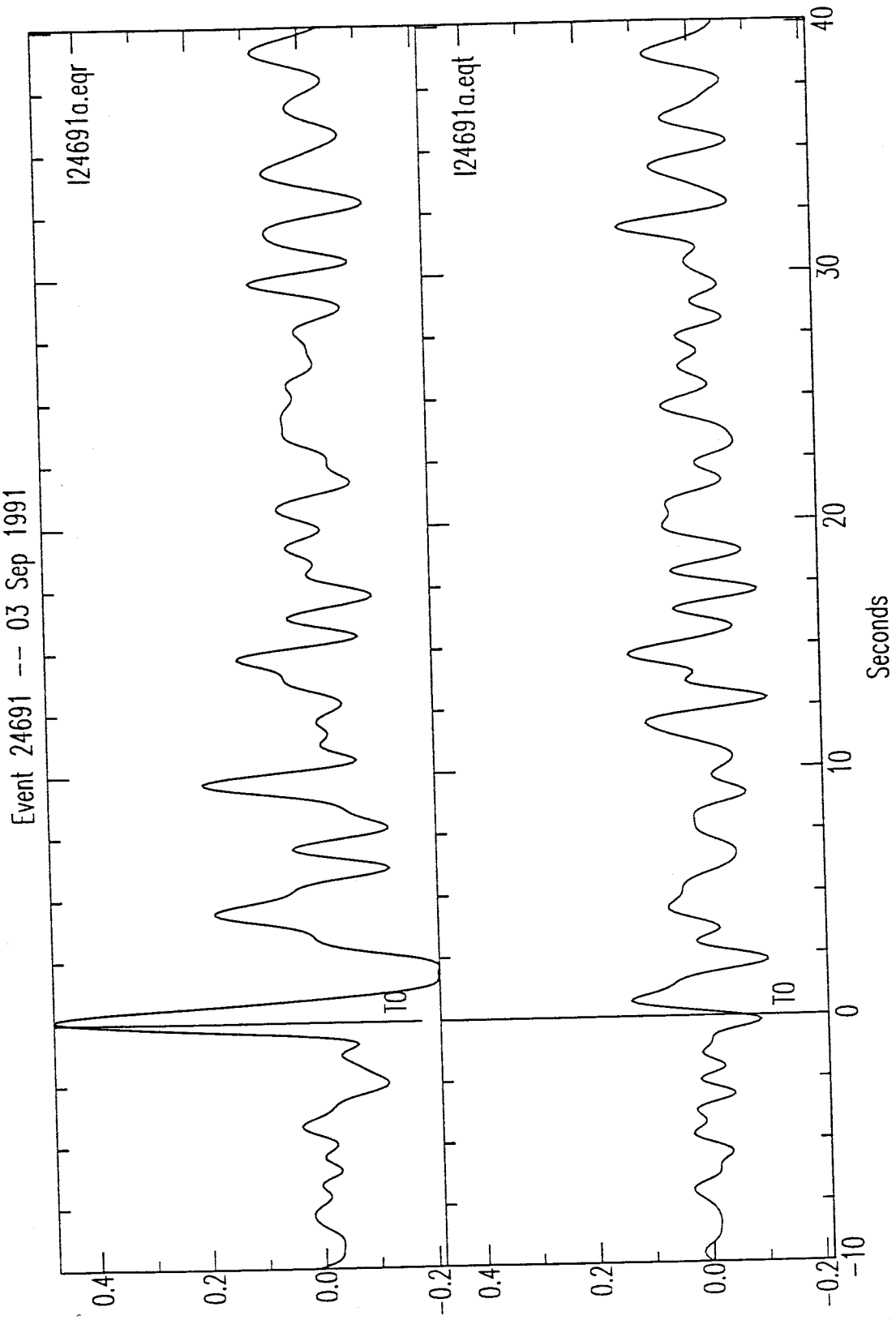
Event 24691 -- 03 Sep 1991
I24691a.eqr
I24691a.eqt
T0
T0
0.4
0.2
0.0
-0.2
0.4
0.2
0.0
-0.2
-10
0
10
20
30
40
Seconds

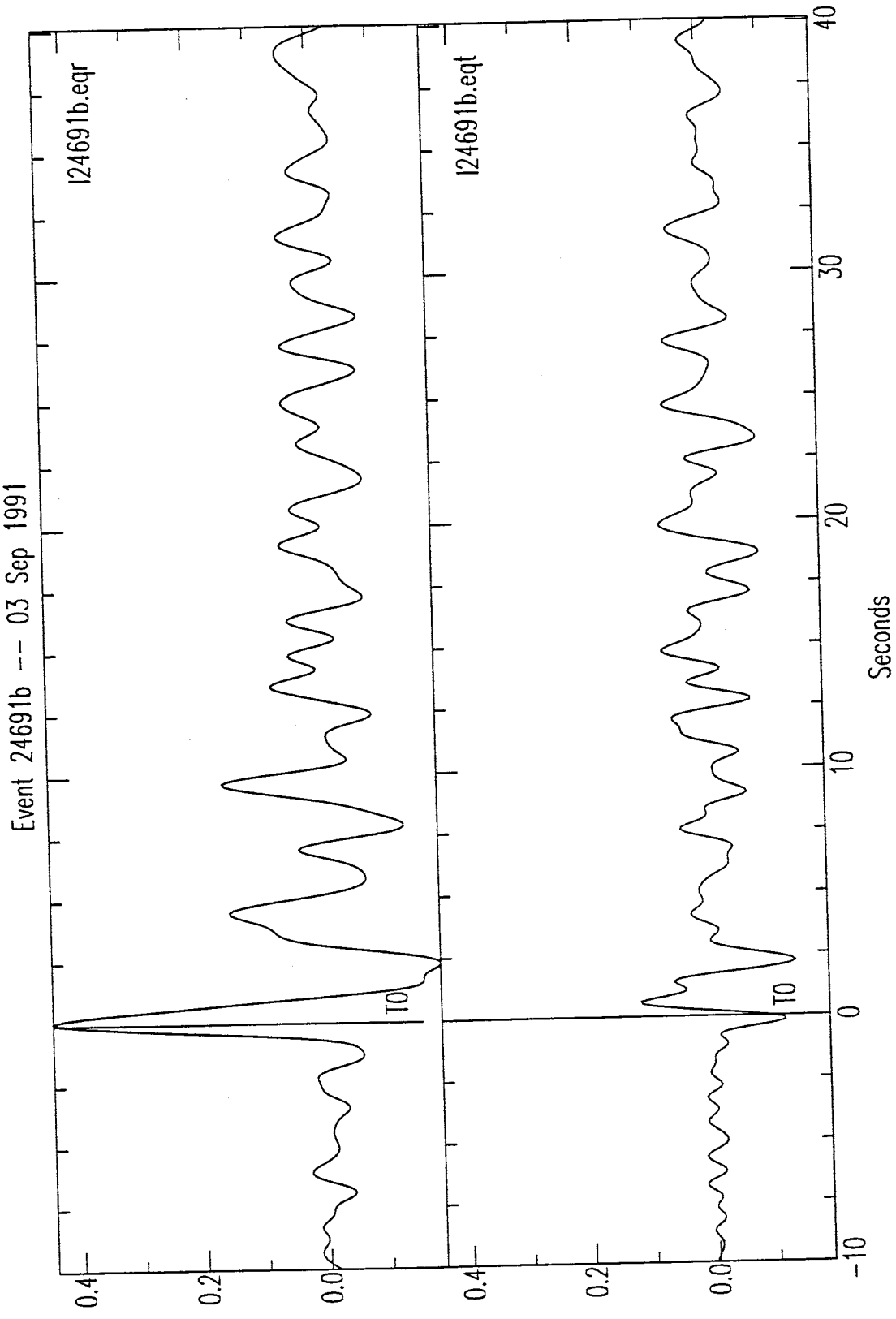
Event 24691b -- 03 Sep 1991
124691b.eqr
124691b.eqt
T0
T0
0.4
0.2
0.0
0.4
0.2
0.0
-10
0
10
20
30
40
Seconds

NORTHWEST DATA

This section shows the first forty seconds of the radial and tangential receiver functions for the four events from the northwest. The direct P arrival, marked by the TO line, represents the beginning of the receiver function. Table B3 provides information on the deconvolution parameters used in the source equalization of each event.

TABLE B3. Deconvolution Parameters used for Source Equalization of Northwest Data

Event I.D.	Date*	Page	Water-Level Parameter	Gaussian Filter Width
32590	21 Nov 90	B15	0.001	2.5
05291	21 Feb 91	B16	0.001	2.5
06791	08 Mar 91	B17	0.001	2.5
15091	30 May 91	B18	0.001	2.5

* From U.S. Geological Survey Preliminary Determination of Epicenters Monthly Listings.

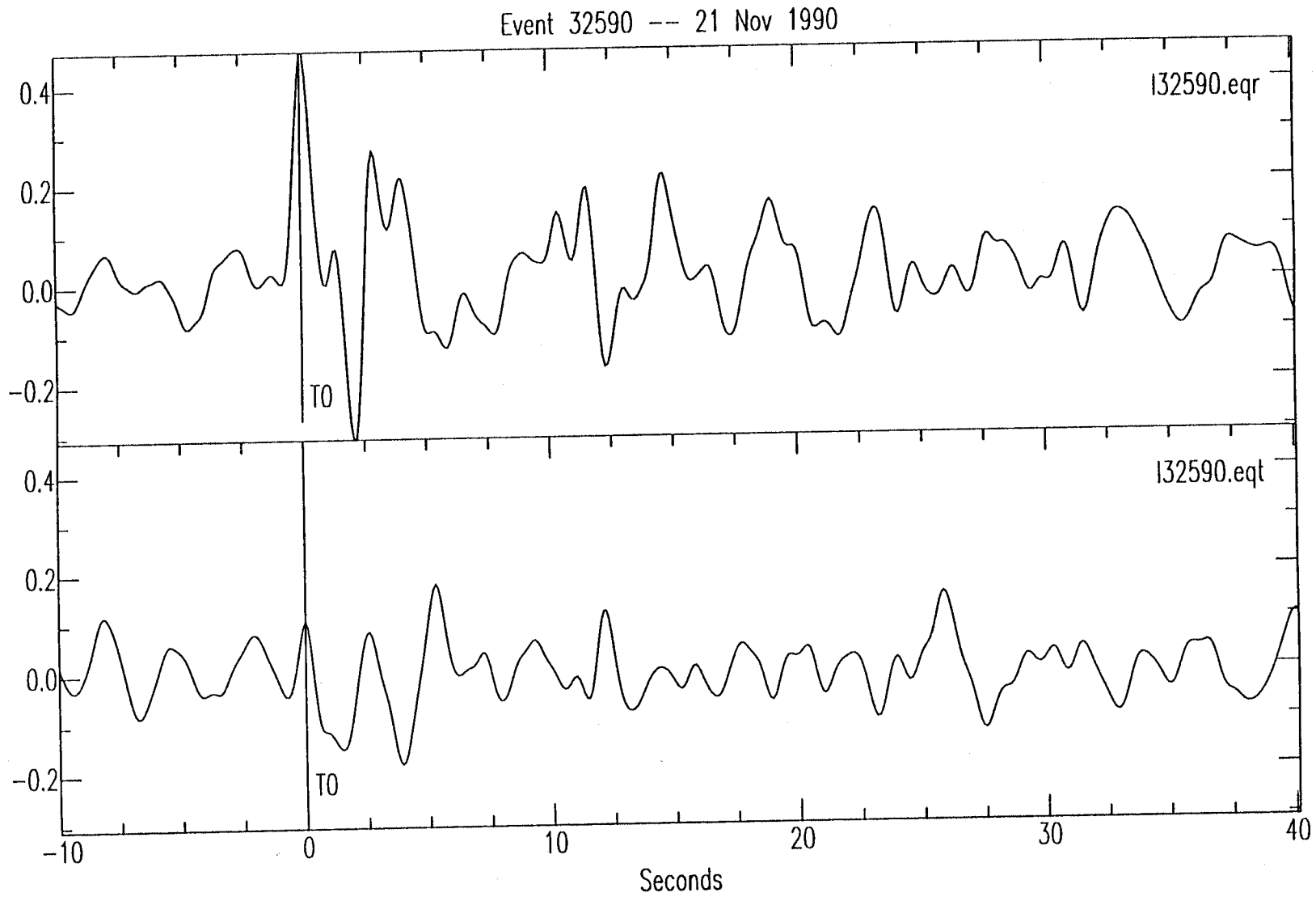
Event 32590 -- 21 Nov 1990
132590.eqr
132590.eqt
T0
T0
0.4
0.2
0.0
-0.2
0.4
0.2
0.0
-0.2
-10
0
10
20
30
40
Seconds

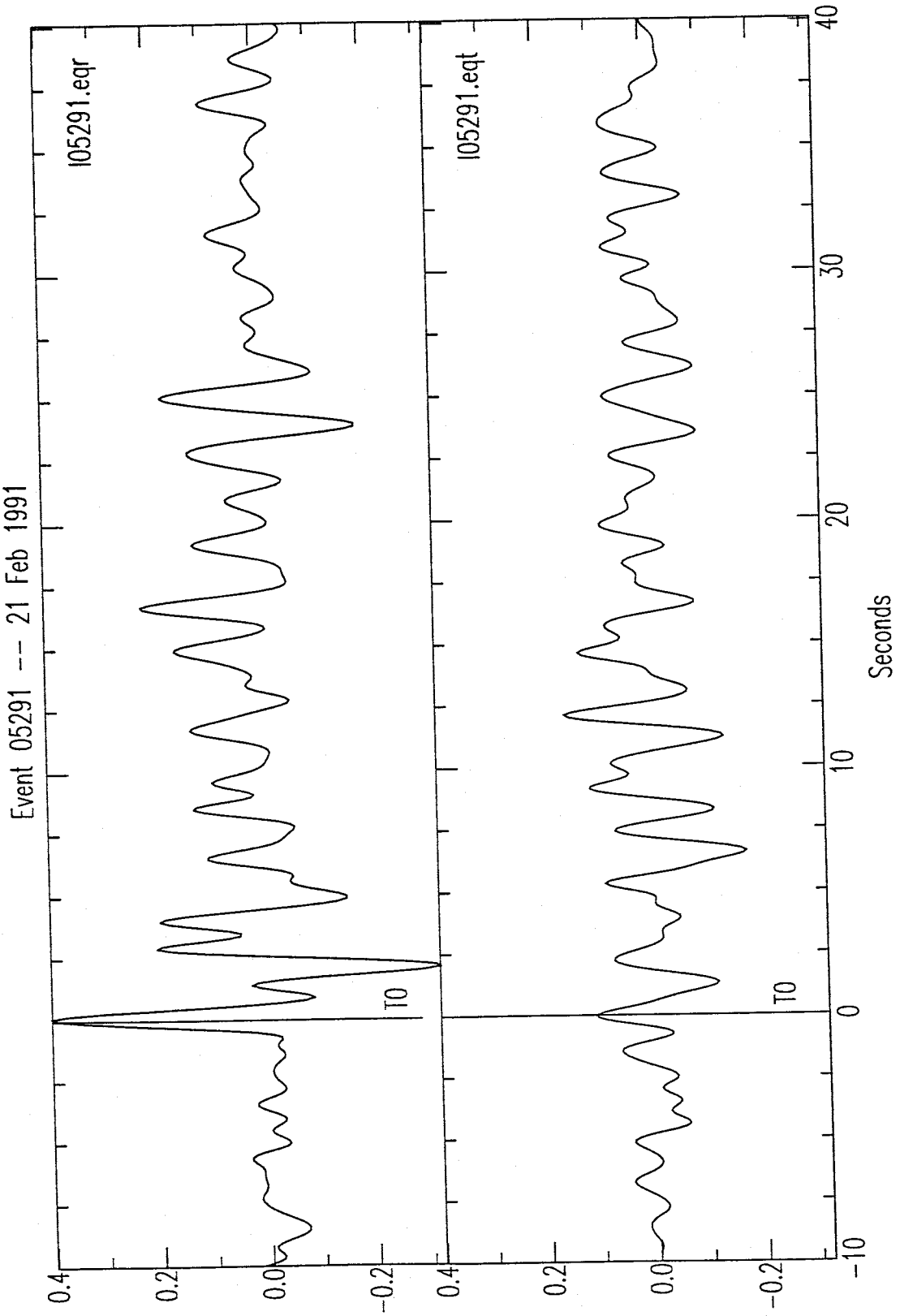
Event 05291 -- 21 Feb 1991
105291.eqr
105291.eqt
T0
T0
0.4
0.2
0.0
-0.2
0.4
0.2
0.0
-0.2
-10
0
10
20
30
40
Seconds

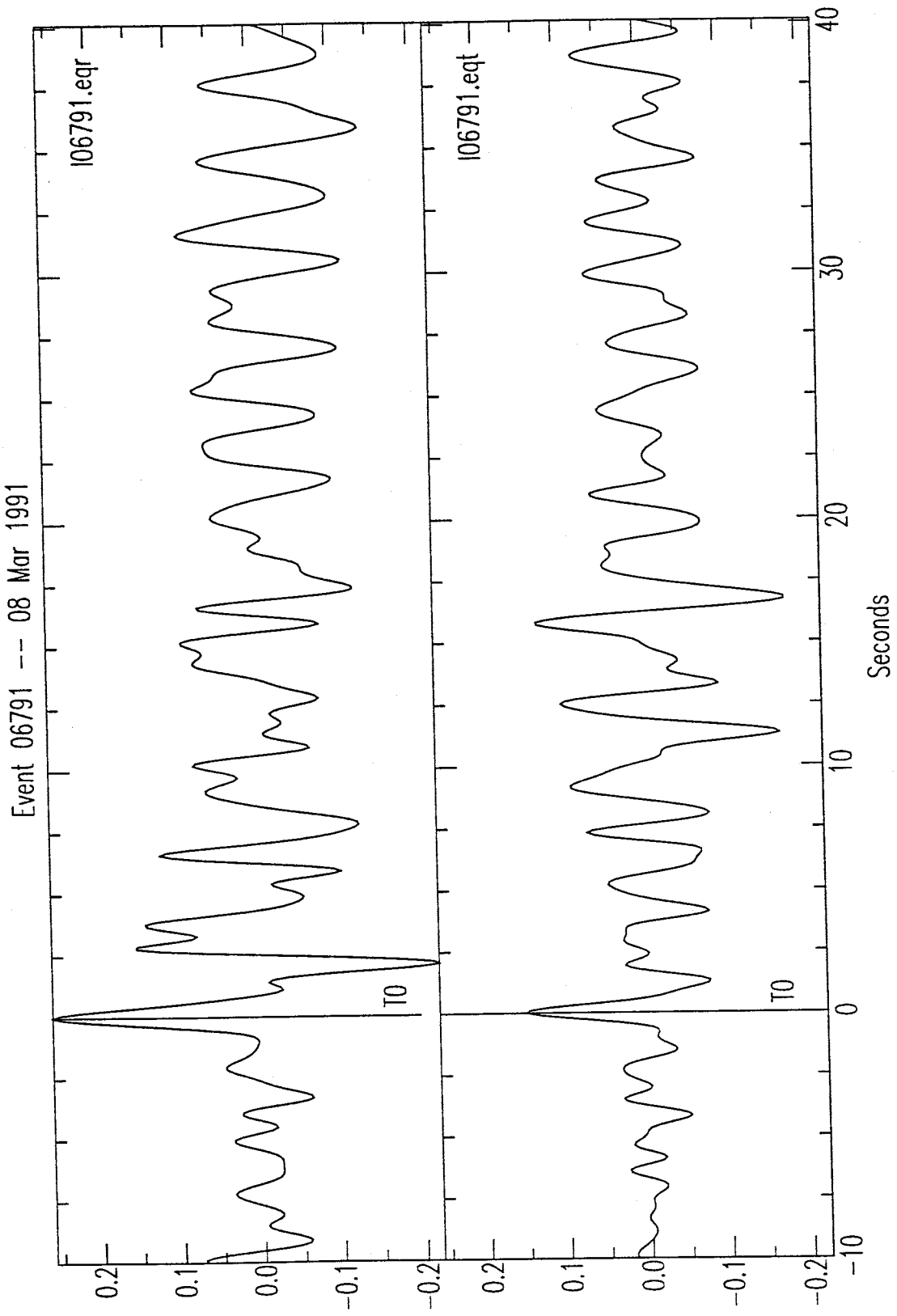
Event 06791 -- 08 Mar 1991
106791.eqr
106791.eqt
T0
T0
0.2
0.1
0.0
-0.1
-0.2
-10
0
10
20
30
40
Seconds

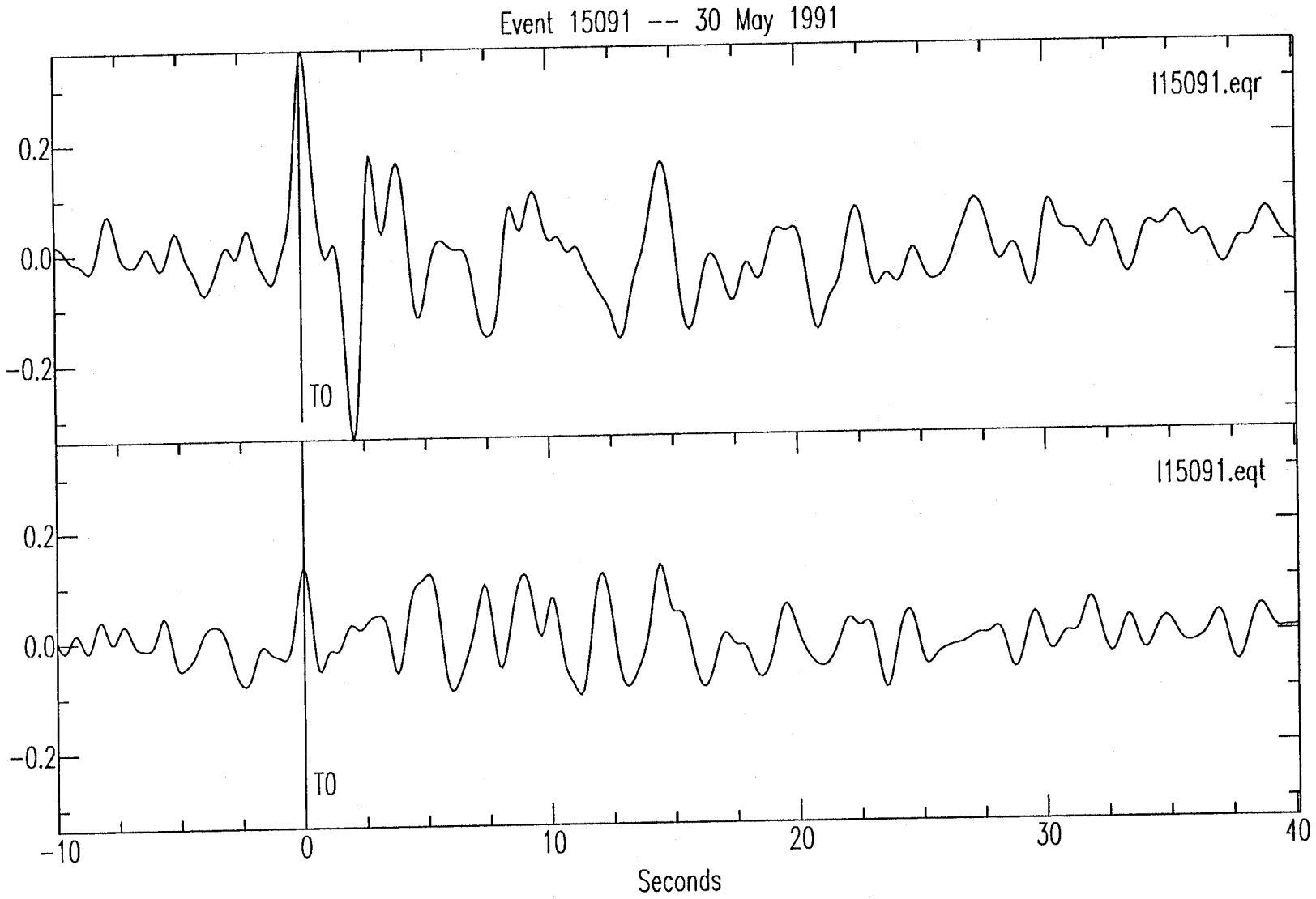
Event 15091 -- 30 May 1991
I15091.eqr
0.2
0.0
-0.2
T0
I15091.eqt
0.2
0.0
-0.2
T0
-10
0
10
20
30
40
Seconds

APPENDIX C

MANUAL FOR USING TELESEISMIC RECEIVER

FUNCTION INVERSION CODES

PLUS

SHORTCUT TRICKS FOR SAC AND OTHER USEFUL

SHELLSCRIPTS

TABLE OF CONTENTS

INTRODUCTION

This manual provides information on a variety of programs that are necessary for obtaining and interpreting receiver function modeling results. Section I is simply a compilation of a few how–to's, some of which are general to SAC, and some of which are specific to the geophysics Sparc station, passcal2. This section is given first because many of the lessons learned will be referenced in later sections. Section II describes methods of finding good events for a receiver function inversion, but can be used for finding events for any type of study. Sections III through VII deal specifically with the steps for the source equalization and inversion of teleseismic receiver functions.

Throughout many of the sections, there are references to executable programs, shell scripts and SAC macros, the names of which will appear in **bold type**. Table C1 gives the alphabetical listing of all the bold type programs listed in this manual and the location of the respective source code (Because the Seismic Analysis Code package is referred to so frequently in the manual, "SAC" will not appear in bold type). The executables for all standard language programs and non–edited C–shell scripts are located in /usr/local/bin. Also, there are many instances where examples of program runs are given. To display the questions and statements that would normally prompt you on the computer screen, a different font (question or prompt font) will be used.

TABLE C1. Executable Programs, Shell Scripts, and SAC macros with the Respective Source Code Locations

PROGRAM NAME	SOURCE CODE LOCATION
anmohder (ISM)	/usr/local/SAC/aux/macros
bza	/usr/local/src/seis
bzc	/usr/local/src/seis
bzw	/usr/local/src/seis
czlhder (ISM)	/usr/local/SAC/aux/macros
decon (CS)	/usr/local/src/Rftn.Forward
mailagent	/usr/local/src/mailagent
manyinv	/usr/local/src/Rftn.Inverse
manyvplot	/usr/local/src/Rftn.Forward
mktable	/usr/local/src/crosscor
pltmac1 (FSM)	/usr/local/src/Rftn.Forward
pltrec (ISM)	/usr/local/SAC/aux/macros
pql	/usr/local/src/lamont/src/pql
pwaveqn	/usr/local/src/Rftn.Forward
ref2segy	/usr/local/src/lamont/src/ref2segy
respknt	/usr/local/src/Rftn.Forward
rminst (ISM)	/usr/local/SAC/aux/macros
rstack	/usr/local/src/Rftn.Forward
sac	/usr/local/SAC/src
segy2sac	/usr/local/src/lamont/src/segy2sac
sgftops	/usr/local/SAC/utils
smthinv	/usr/local/src/Rftn.Inverse
snglinv	/usr/local/src/Rftn.Inverse
srun1 (CS)	/usr/local/src/Rftn.Forward
sweep (CS)	/usr/local/src/Rftn.Forward
vplot	/usr/local/src/Rftn.Forward
wtxhder (ISM)	/usr/local/SAC/aux/macros
zps	/usr/local/src/seis

(CS): C-shell script; (ISM): Installed SAC macro; (FSM): Floating SAC macro
All other executables are from standard FORTRAN or C languages and can be found in /usr/local/bin.

Section I: Assorted facts and tricks for SAC and UNIX

The commands to re-compile and update SAC, as well as the SAC executable are in /usr/local/SAC/bin.

Initiating SAC

To start up SAC, all that you need to do is type SAC at the prompt. After the copyright information, you will get a sac prompt:

SAC>

There are two types of windows that you can bring up in SAC; a sunwindow or an X-window. X-windows are preferred because you can change the window size as you would change any other window on the screen. Sunwindows are a standard, unchangeable size, but can be moved around the screen. To bring one of these windows up, use the begin device (bd) command as follows:

```
SAC> bd sun      (for sunwindow)
SAC> bd x        (for X-window)
```

Another command that is commonly used is qdp off. Qdp stands for **q**uick and **d**irty **p**lot. By default qdp is on, meaning that plotting will be sped up because SAC will not plot every data point. This is fine for large files that you simply want to glance at, but in most cases you will want to type:

```
SAC> qdp off
```

This will produce a much smoother plot. (See qdp in SAC manual for more details)

SAC Macros

You can write a series of SAC commands together and execute them all at once by creating a macro. The following is an example of how to create a very simple macro to edit ("cut") a file, read it in, perform a fast Fourier transform, and write the output to a new filename. Note that the file "sacfile1" must be in SAC format.

```
% vi macro1    (create a file called macro1)
```

Starting on the top line, type a list of commands

```
cut 100 200
r sacfile1
fft
w sacfft1
```

Once the macro has been created, you can execute it from SAC by simply typing:

```
SAC> macro <path> macroname
```

where <path> is the pathway to the directory where macro1 resides. If you have a macro that you frequently use, you can make it a permanent SAC macro by using the installmacro command. Simply type

```
SAC> installmacro <path> macro1
```

Once you make macro1 a permanent macro, you can use it from that point on without providing a path. All installed macros are placed in /usr/local/SAC/aux/macros. Any time that a SAC macro is referenced in this manual without the <path> in place, the macro has already been installed as a permanent SAC macro. For examples of more complicated interactive macros, see the SAC manual or look at some of the previously installed macros.

SAC Graphics Files

Creating SAC Graphics Files

To get a hard copy of any plot that you create in SAC, all that you have to do is open a SAC graphics file and then type the plot command as usual. However, instead of showing up on the screen like it usually does, the plot is sent to a SAC graphics file. The following is an example of creating a SAC graphics file for a plot of the SAC file signal.vert:

```
% sac
SAC> qdp off          (quick and dirty plot off)
SAC> bd x             (open X-window for plot)
SAC> r signal.vert     (read the SAC data)
SAC> bg sgf           (open SAC graphics file)
SAC> p1               (see NOTES 1 and 2)
SAC>  q               (quit sac)
```

NOTE 1: The plot will NOT show up on the screen!

NOTE 2: See section on graphics action module in the SAC manual for different plotting commands.

A new file will have been created in the working directory called f00?.sgf, where ? = 1,2,3,... depending on how many plots you create. Once the "bg sgf" command is given, all plotting commands will be send to f00?.sfg files until you quit SAC.

Printing SAC Graphics Files

To make a hard copy of a SAC graphics file on a laser printer, you must first use the executable called **sgftops,** which converts the .sgf file into a postscript (PS) file so that the printers can print it out. From passcal2, you can send the postscript files to either the Sparc printer connected to griffy (griffy is the name of the Sparc2 machine in the geophysics computer lab) or over to the printers at the TCC. Sending to griffy is quite a bit simpler since you just use the "lpr" command just as if the printer were hooked up directly to passcal2.

To send a SAC graphics file to griffy, assuming that you have already created the SAC graphics file and have quit quit SAC, use the folowing commands.

```
% sgftops f001.sgf f1    (this creates a PS file, f1)
% lpr -Psparc f1         (-Psparc designates black and white printer)
```

If you do not want the actual postscript file sitting around, you can combine these commands into one line,

```
% sgftops f001.sgf - | lpr -Psparc
```

This converts f001.sgf to a PS file and sends it directly to standard out (denoted by the -) rather than to a file. It then pipes that through the lpr command to print it out.

Sending a printout to the TCC printers requires that you have an account on one of the school machines through which you can communicate via a remote shell (see manual pages on rsh). To use a remote shell, you must first get into your school account (on titan for example) and create a ".rhost" file. In this file you just type one line.

```
passcal2  yourpasscal2loginname
```

Things work much easier if your login name is the same for both machines. This way, there is no fussing around with passwords. Once this is done, you can use the remote shell (rsh) command to print SAC plots in the following way:

```
% sgftops f001.sgf - | rsh titan lpr -Pspruce
```

This also converts f001.sgf to a PS file and sends it directly to standard out (denoted by the -), but pipes it through a remote shell command for printing on the TCC postscript printer called spruce.

Writing and Reading from Exabyte Tapes

In order to back up files to a tape, or read files from a tape, you need to use the "tar" and "mt" commands. Once a blank tape is inserted into the Exabyte drive, you can write a file to tape by typing:

tar cvf /dev/rst0 filename

NOTE: replace filename with a directory name to back up a whole directory

To look at the contents of a tape type:

tar tvf /dev/rst0

To extract files from a tape and place them in current directory:

tar xvf /dev/rst0

In any of the above, use nrst0 instead of rst0 to execute the command without rewinding the tape afterward. This is necessary in order to append files. After each time you write a file or a directory to tape, an end-of-file (EOF) is inserted. If you want to write more files to that tape, you must first jump over the end-of-file. This is where the "nrsto" and the "mt" commands come in. For example, if you had already placed a small directory of files on a tape (and ejected the tape which automatically rewinds it) and you know that there is room to put some more files on it, you can skip over the EOF and write the new files. To do this, insert the tape and type the following:

mt -f /dev/nrst0 fsf 1 (1 is the number of EOF's to skip)

This will skip over 1 EOF and just sit there and wait for another command, which in this case would, of course, be another write command. You could ap-

pend a third set of files at a later date by simply changing the 1 to a 2 in the above command. Other uses for the mt command include:

```
mt -f /dev/rst0 rew      (to rewind a tape)
mt -f /dev/rst0 status   (to give status of the SCSI drive)
```

Section II: Finding Appropriate Events

The first step in gathering data for a receiver function study is to find specific teleseismic events that can be used for the study. Generally, you want events that are between 30 and 90 degrees away and have sufficient magnitude to achieve a good signal to noise ratio (usually 5.8 or larger). There are two ways to search the archive of USGS data to find events that fit the above (or any other) criteria. First, and most laborious is to search through the archive printouts by hand (These printouts are just copies of the USGS earthquake locations that we receive almost daily via electronic mail, which are archived my month and stored in usr/local/ARCHIVE), and look for events that fit the magnitude constraints. Once you have gathered a number of possible events, you can use the program called **bzw** (for station WTX). This program asks you for the latitude and longitude of the event and returns the distance and back-azimuth from station wtx. Programs **bza** and **bzc** will do the same for stations at Albuquerque (anmo) and Cerro Azul (czl) respectively. After this step is completed, you have the magnitude and distance to the events and can decide which ones are suitable to look at.

The Mailagent

How to use the Mailagent

A second and much quicker way to search the archives is to use a program called **mailagent**. This program was written by a real programmer who used C so I mostly use it as a black box, but the README is very good. Thus, I suggest that you read it in addition to the following overview. **Mailagent** works in two different modes. First, it acts as a filter to all mail coming from USGS to Dr. Schlue's fnsr account, searching for any events that fit the specified magnitude and distance constraints. Any such event is printed out in a file called "good_events" which lists the date, origin time, magnitude, depth, distance and back–azimuth. The mail filter is presently set to pull out events with magnitude greater than 5.6 and distance between 30 and 110 degrees. (This allows for SKS studies as well) Another way to use **mailagent** is to use the version that is located on the Sparc station in the mailagent directory. With this "interactive" version of the program, you can search through the old archives for specific events. As mentioned above, the USGS mails are archived in monthly files which can be searched by **mailagent**. Say, for example that you wanted to find all events in the JUL91 file with magnitude greater that 4.5 which were between 38 and 52 degrees away. To do this, simply edit the file called localdefs.h (in /mailagent) which list all of the constraints, and change the magnitude and distance values accordingly. Once this is done type "make" to re–compile the program. Before you can search the JUN91 file you need to make one small addition; you must edit it and place the line "from USGS.Gov" at the very top (most months in the archive already have it, just check to make sure) This fools the mailagent into thinking that the file is still mail. Now just type:

```
% cat JUL91 | mailagent
```

Some messages may appear on the screen (ignore them), and if any events in that month fit the constraints, they will show up in a file called good_events.

Problems with the mailagent

Mailagent does have one glitch that I do not know how to fix. If the latitude and longitude listed in the USGS message do not have three digits after the decimal (e.g 135.25 E instead of 135.251 E), the mailagent will not like it. In fact, it will place a zero there and assume north (if Lat.), and west (if Lon.). So the above longitude would be read as 135.250 W. Most of the time, the USGS sends three digits, so it is not often a problem. Simply check any "good events" for latitudes and longitudes ending in 0 N or 0 W and double check the original mail to see if **mailagent** has made a false assumption.

Getting P and S Wave Arrival Times

No matter which method you use to search for an event, you will eventually know the origin time, depth and distance of the event. With the program **zps**, you can use these three values to get the P and S wave arrival times. The program first asks for the distance to the event in degrees, and then asks you to enter a number (0–9) that corresponds to a the depth that is closest to the depth of the event. The numbers and corresponding depths (in kilometers) are:

0: 33.0	5: 351.6
1: 96.7	6: 415.3
2: 160.4	7: 479.0
3: 221.1	8: 542.7
4: 287.8	9: 00.00 (surface)

If an event was at depth 240km you would enter 3 for the depth.

The output from **zps** are the P and S wave travel times (in minutes and seconds) which need to be added to the origin time to get the arrival times. These arrival times will become valuable when downloading events from tape.

Section III: Preparing The Teleseisms For Deconvolution

After finding an event that fits the magnitude and distance constraints, you must find the Exabyte tape that contains the event and download that tape to the computer. This can be done by using the program called **ref2segy**. The following steps show how to download a tape.

1. Create a directory in which to place the data from the tape.

   % mkdir trans

2. Get into that empty directory.

   % cd trans

3. Insert the tape into the Exabyte drive, close the door and wait for the green "ready" light to come on.
4. Type the command:

% ref2segy −x /dev/rst0 wtx?? (?? is the number on the tape)

Depending on the amount of data on the tape, this step can take from 20 − 40 minutes.

5. When downloading is finished, remove the tape and re−file.

SEGY Data Format

After downloading, the directory /trans will contain many subdirectories named R???.0$, where ??? is the julian day and $ will be either 1 or 2 and refers to the data stream. On the information sticker of the tape that was downloaded you will find which data stream was used for which instruments. In most cases, data stream 1 is used for the broadband instruments and data stream 2 is used for the intermediate−period instruments, but there are a few exceptions. Inside each of these directories is where you will find the actual data, broken down into 1 hour blocks. The filenames will look like the following example:

12.48.37.0029.4

--12.48.37 is the hr.min.sec of the beginning of the hour block

--0029 is the Reftek I.D. number

--4 is the component.

In stream 1, the components are 1, 2 and 3 for vertical, north–south and east–west respectively. In stream 2, the components are 4, 5, and 6 for vertical, north–south and east–west. The above would thus be the vertical component on stream 2.

Viewing SEGY Data with PQL

Once the hour block containing the event is found, you can take a look at it with **pql** (Passcal Quick Look) to check the signal–to–noise ratio before converting to SAC. To look at all three components of a given hour of data simply type:

% pql 12*

See the **pql** manual for details on how to move around once in **pql.**

Converting SEGY data to SAC format

If the event looked good in pql and you wish to process the event further, then you need to convert the data into SAC format. Before doing this, it is recommended that you create two directories, /rd and /sac. Directory /rd will contain the raw data (one hour in SEGY format), and /sac will contain the same hour of data in SAC format. The actual program that converts the data into SAC format is called **segy2sac**. The following is an example (starting from the beginning) of converting data to SAC:

```
% cd R150.02
% mkdir rd sac
% segy2sac 12* -d sac ("-d sac" puts SAC data in the sac dir)
% cd sac
% ls
```

You should see

12.48.37.0029.4.sac

12.48.37.0029.5.sac
12.48.37.0029.6.sac

% cd .. (move out of sac directory back to R150.02 direcory)
% mv 12.48.37* rd (moves raw SEGY data into /rd)

If there are no other events on that day, remove all the rest of the hour blocks of data by typing:

% rm * (this will NOT remove /rd and /sac)

Now go back one directory and change the name of the Reftek directory so that you know that you have an event in SAC format on that day.

% cd ..
% mv R150.02 I15091

I is the instrument – Intermediate ; 150 is the julian day ; and 91 is the year. It is best to move this directory out of /trans and into a directory where it can be processed (e.g. /events).

SAC Processing Needed Prior to Deconvolution

In the directory where the SAC data are located, change the names of the three components (vert,ns,ew) to a1, a2 and a3 respectively. This is necessary in order to use some of the general macros in SAC. Just type:

% mv 12.48.37.0029.4.sac a1
% mv 12.48.37.0029.5.sac a2
% mv 12.48.37.0029.6.sac a3

At this point, you must figure out how many seconds into the hour block (3600 sec) of data the event is. You should have the P arrival time from the program **zps**. By subtracting the time at which the hour block begins from the P

arrival time, and converting to seconds, you have how far into the block you need to go. The general steps that need to be done in preparation for deconvolution are as follows:

1. Cut about 120 seconds of data (30 sec pre P, 90 sec after).
2. Process the header information using the appropriate SAC macro.
   wtxhder -- for station WTX
   clzhder -- for station CZL
   anmohder -- for station ANMO

-- The macro will ask you to enter the latitude and longitude of the event as well as the station name. The station name for will obviously depend on which station the data came from. The macro automatically figures out the distance and back-azimuth of the event and records the information in the event header file. If the station contains two sets of instruments, it is a good idea to include the instrument type in the station name to avoid confusion (e.g., WTXI for intermediate instruments and WTXB for broadband).

3. Decimate if necessary (down to 10 samples per second).

-- If you are sampling at 10 samples per second, you obviously do not have to do this, but if you are sampling at 20 samples per second, you want to decimate to 10. This is simply to help speed up the deconvolution.

4. Switch polarity on the NS intermediate trace (for WTX only!).

-- The polarity for instrument # 172 is reversed, if this is still the instrument in use (as of this manual it is), than you need to multiply the trace by -1.

5. Pad the data with zeros.

-- All that you want to go into the inversion are the data from right where the initial P wave begins until about 40 second after that point; the rest should be padded with zeros. To do this in SAC, you need to use the "cuterr fillz" command.

The example "data preparation" (page C19 and C20) will show how to use this command.

6. Rename the components.

-- a1 a2 and a3 need to be renamed so that you know that they have been processed, and so the normalization macros can identify components. A good renaming convention is IXXXYY.c where I is the instrument (I or B), XXX is the julian day, YY is the year and c is the component (z, n or e)

7. Normalize the instrument response.

(NOTE: the following description of instrument normalization is for the intermediate band instruments.)

-- This may sometimes be referred to as "removing the instrument" but, in actuality, we are just normalizing the instrument response so that the effects of the instrument on the signal will come out in the deconvolution. To do this, you need the individual instrument specification sheets. From these sheets, you will need the following values for each instrument:

1. the generator constant: G
2: the damping resistor: DR
3. the coil resistance: CR

From these values, you can calculate the effective generator constant (G_e) from the following relationship:

$$G_e = \frac{DR}{DR + CR}$$

Each component of displacement needs to be divided by it's respective effective generator constant.

A simple macro called **rminst** has been created to quickly normalize the intermediate instruments with vert, ns and ew serial numbers 137, 172, and 169 respectively. The numbers for new instruments could easily be placed into the macro.

8. Print the results to make sure that you haven't goofed.

The following example shows the exact commands given during a routine preparation for deconvolution. A reference to the numbered steps above will be given.

```
        % sac
---------------------------- STEP 1
        sac> qdp off
        sac> bd x
        sac> cut 2194 2314
        sac> r a1 a2 a3
        sac> p1          (make sure that the cut was right)
        sac> w over
---------------------------- STEP 2
        sac> cut off     (cut must be off to process header)
        sac> macro hder
                LAT? 54.5       (north is positive)
                LON? -161.57    (east is positive)
                STA? WTX
---------------------------- STEP 3
        sac> r a1 a2 a3
        sac> dec 2       (for data sampled at 20 sps)
        sac> w over
---------------------------- STEP 4
        sac> r a2
        sac> mul -1      (change polarity on n-s trace)
        sac> w a2
---------------------------- STEP 5
```

```
sac> cuterr fillz
sac> cut 2224 2264    (40 seconds following direct P)
sac> r a*
sac> rmean
sac> taper
sac> w over
sac> cut 2194 2314   (original 120 sec cut)
sac> w over
------------------------- STEP 6
sac> r a1 a2 a3
sac> w I15091.z I15091.n I15091.e
------------------------- STEP 7
sac> macro rminst
------------------------- STEP 8
sac> r I15091.z I15091.n I15091.e
sac> p1
```

Figure C1 shows the vertical component of the above event cut down to 120 seconds (above) and same component padded with zeros and ready for deconvolution (below).

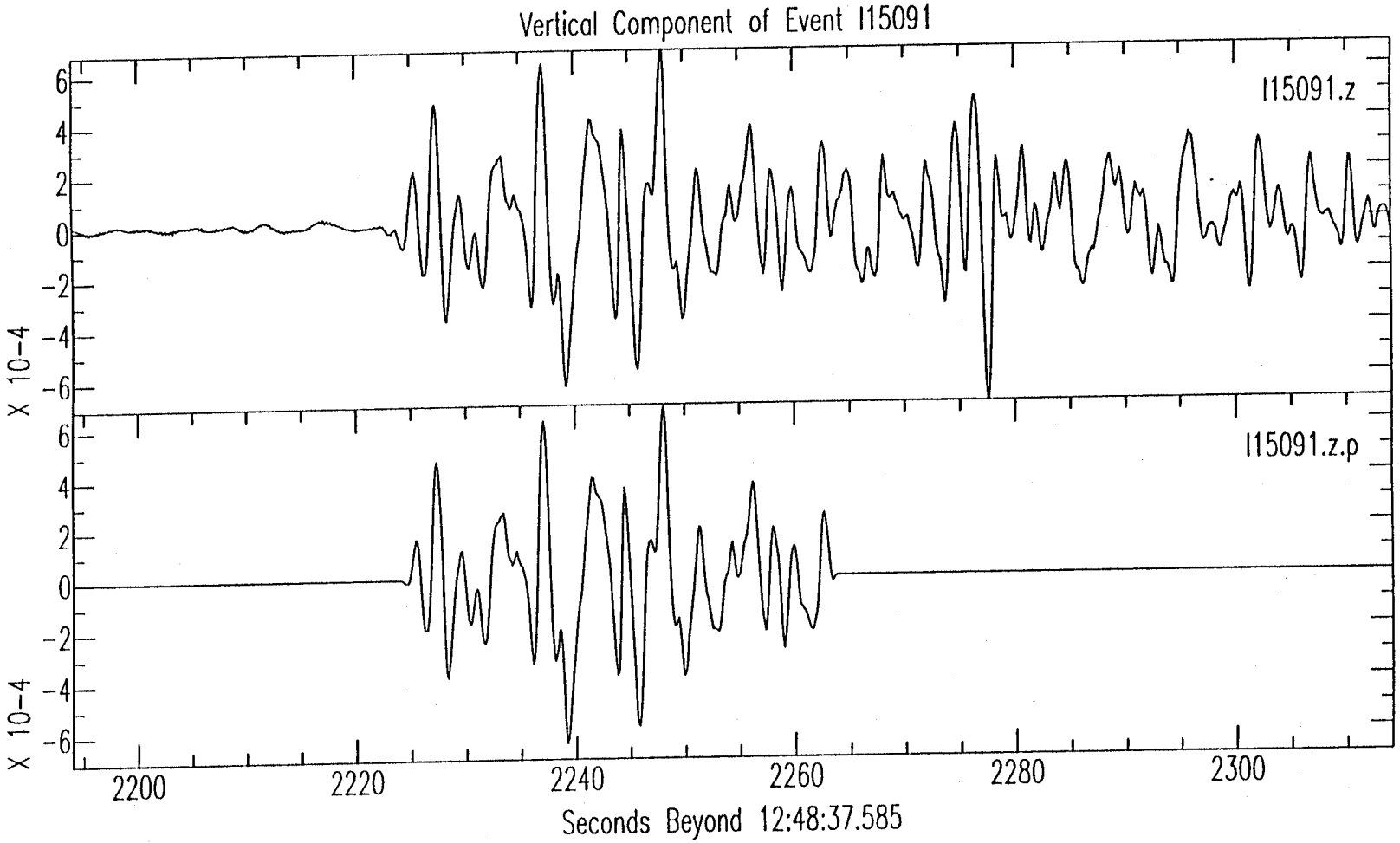

Figure C1. 120 second cut of raw data containing the P-waveform for event I15091 before padding with zeros (top) and after padding all but the first 40 seconds of P-waveform with zeros (bottom).

Section IV: Performing the Deconvolution

The deconvolution of the vertical energy from the horizontals is done by a program called **pwaveqn**. To run **pwaveqn** you must be in the directory where the components processed in the previous section reside (e.g., I15091.z, I15091.n I15091.e). The program automatically rotates the horizontals into the radial and tangential directions, so you needn't do so beforehand. Using **pwaveqn** to deconvolve the example data would look like:

```
% pwaveqn
Specify quake file:
% I15091
Real data (y or n):
% y                    (as opposed to synthetic)
Window data (y or n):
% n
Specify outfil:
% I15091
Trough filler c =:
% 0.001                (see NOTE 1 below)
Gaussian scale a =:
% 2.5                  (see NOTE 2 below)
Enter phase shift:
% 30                   (see NOTE 3 below)
Try another:
% n
```

NOTE 1: The trough filler (c) is also called the "water level" and determines the minimum amplitude in the spectra of the vertical component. This filling of spectral holes becomes necessary when the spectra of the horizontals gets divided by the spectra of the vertical during deconvolution. Common values for c are 0.1 0.01 0.001 and 0.0001. Ultimately, you want to use the smallest trough filler for which you can achieve stable deconvolution.

NOTE 2 The Gaussian scale (a) is the width factor for the Gaussian filter. The smaller this width, the more the signal gets filtered. Common values for the Gausse filter width are 2.5 and 5.0

NOTE 3: The phase shift is simply the number of seconds before the first arrival in the receiver function. 30 seconds is commonly used.

The output will look like :

I15091_2.5_0.001.eqr --- for the radial receiver function
I15091_2.5_0.001.eqt --- for the tangential receiver function

Deconvolving Over a Suite of Parameters

There is a shell script called **sweep** that invokes another shell script called **decon** which runs pwaveqn for a series of trough filler / Gaussian scale combinations. For each of two gaussian scales (2.5 and 5.0) it uses each of four trough fillers (0.1, 0.01, 0.001 and 0.0001). To run sweep, simply type **sweep** followed by the quakefile:

```
% sweep I15091
```

The output will be 16 files, 8 radial and 8 tangential. If you wish to change the parameters over which the program sweeps, just edit the shellscript accordingly. It is not a program, so it does not get compiled. It simply invokes **decon** which runs **pwaveqn**.

Plotting Deconvolution Results

There is an easy way to plot all 8 radial receiver functions for comparison. The macro called **pltrec** will plot the four receiver functions where a is 2.5 on one page and the four where a is 5.0 on another page. The macro automatically cuts the radial receiver functions down to 70 seconds in length. Keep this in mind when stacking (next section) because this macro does not touch the tangentials, which will therefore be longer. Running **pltrec** is very simple, just make sure that you are in the directory where the 8 receiver functions are and type the following:

```
% sac
SAC> macro pltrec
```

SAC will echo what it is reading and finally **pltrec** will automatically quit SAC for you. In the working directory should be two new SAC graphics files: f001.sgf and f002.sgf. Simply send these to the printer by one of the methods given in section I. The output will look like Figures C2 and C3.

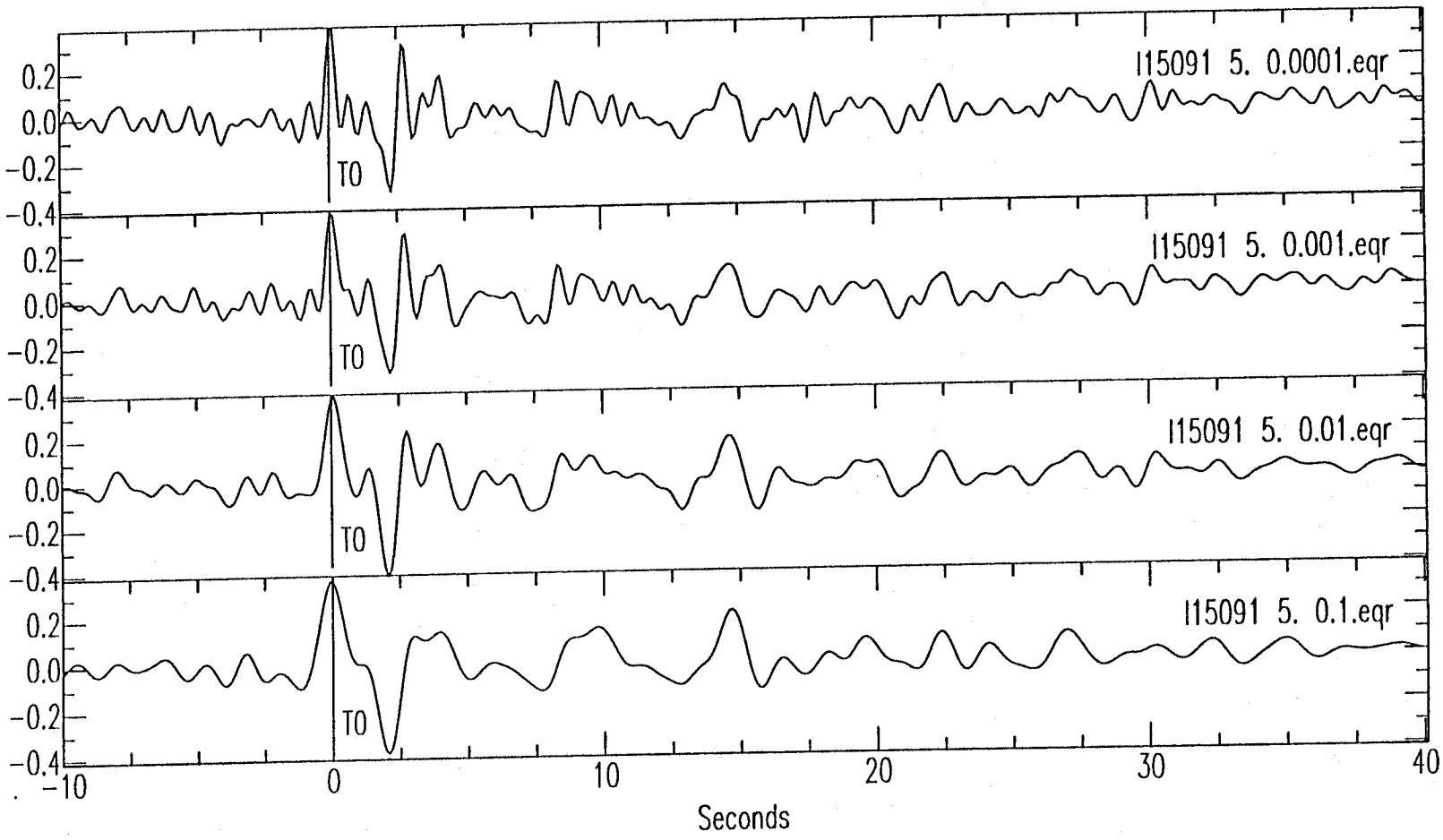

Figure C2. Example output from SAC macro **pltrec.** Receiver functions for event I15091 using four different water-level parameters (c = 0.0001, 0.001, 0.01, 0.1) and a Gaussian filter width (a) of 2.5.

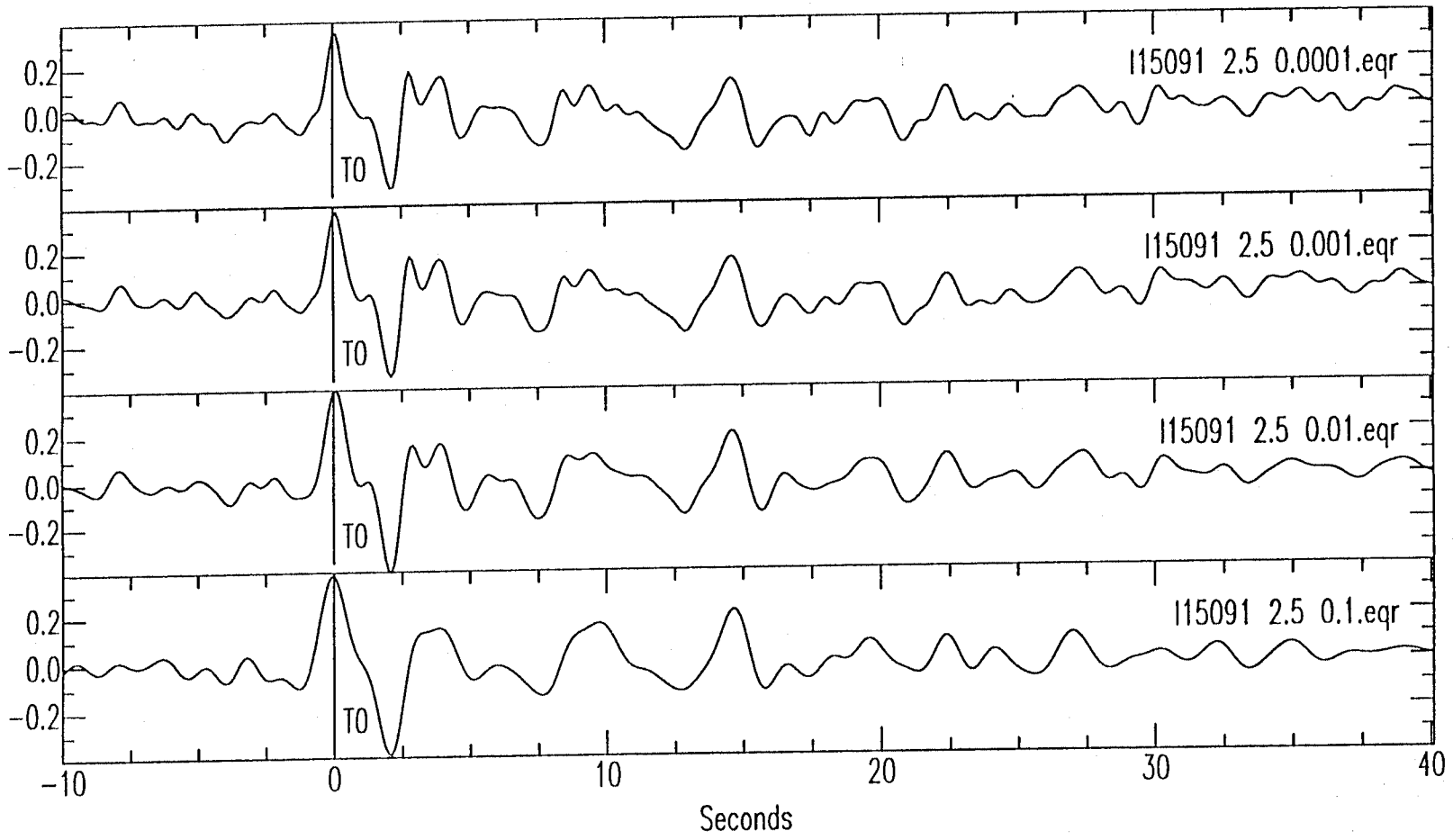

Figure C3. Example output from SAC macro **pltrec.** Receiver functions for event I15091 using four different water-level parameters (c = 0.0001, 0.001, 0.01, 0.1) and a Gaussian filter width (a) of 5.0.

Section V: Stacking Receiver Functions

Once you have run **sweep** on a number of events from a given back-azimuth and direction, you are ready to make a stack. In choosing which receiver functions to stack (within the event cluster), you simply need to decide which set of deconvolution parameters gives the best match among the events. It is acceptable to stack events with differing water level values, but I would stick with one gaussian scale value. Say, for example, that you have three events that you need to stack:

I15091_2.5_0.001.eqr
I16091_2.5_0.001.eqr
I17091_2.5_0.001.eqr

You can stack these events using either SAC or a FORTRAN program called **rstack**.

Stacking with SAC

It is fairly simple to stack receiver functions in SAC. The only thing that you need to be careful of is to make sure that all of the files are the same length. This means that the "npts" value in the header needs to be identical for all events. To alleviate any problems, it is best to make a cut on all files before stacking. After the stacking is done, the result is once again cut down to 30 seconds in length before inverting. The following example illustrates stacking events with SAC.

```
sac> cut 20 70
sac> r *.eqr    (read all of the .eqr files to be stacked)
sac> w over     (now they are all the same length)
sac> r I15091_2.5_0.001.eqr
sac> addf I16091_2.5_0.001.eqr
sac> addf I17091_2.5_0.001.eqr
sac> div 3
```

```
sac> w se_2.5_0.001.eqr.stk   (name for the stack)
sac> cut 20 50          (final cut to 30 seconds)
sac> r se_2.5_0.001.eqr.stk
sac> ch allt −30   (lines up the T0  line at 0)
sac> taper
sac> fileid t n    (places filename in upper right corner)
sac> w over
sac> qdp off
sac> bd x
sac> p1
```

The last command is to plot the final product of the stack to see if things worked. The above procedure should also be done for the tangential components of the three events.

Stacking Outside of SAC

There is a FORTRAN program called **rstack**, which can also stack data files. The nice thing about **rstack** is that it returns the variance and standard deviation along with the resulting stack. For **rstack**, the "npts" values do not have to be identical (although it is a good idea), you just have to know the order of files from smallest to largest. The following example stacks the same three events using **rstack**.

```
                % rstack
enter stacking files info.
enter file suffix:
                % _2.5_0.001.eqr    (suffix that is common to all of the files)
if npts in all arrays are not identical, input names in order
from smallest to largest.
filename:
                % I15091
filename:
```

% I16091

filename:

% I17091

filename:

% [return] (a blank return means that you are done)

weigh the seismograms:

% n

stack output file:

% se_2.5_0.001.rad.stk (stack filename)

For output, you will have (SAC files):

se_2.5_0.001.rad.stk
se_2.5_0.001.rad.stk_var
se_2.5_0.001.rad.stk_std

NOTE: If you are stacking different water levels, just use .eqr as the suffix and enter the rest with the filename. Also, you will want to go into SAC and cut down to 30 seconds before inverting (5 seconds before the initial pulse, 25 seconds after).

Section VI: Running an Inversion

There are three different programs that can be used for inverting the stacked receiver functions. They are **manyinv**, **snglinv** and **smthinv**. No matter which of these programs is used, the first step is to arrive at some starting model. Figure C4 is an example of a starting model called "brstd". The top portion shows the model in the exact format as required by the programs. The lower portion (below the line of asterisks) explains the format. "Brstd" is a general 40 layer model and is often used in case where little is known about the structure in question. The number and thickness of layers can be changed if desired, as was done in Figure C5 which shows the Hartse.m starting model for the Socorro area. The inversion programs are presently set up to read only the seismic velocities and the densities of the layers. A Q value of 500 for P−waves and 225 for S−waves is assumed for every layer. Also, each layer is assumed to be horizontal, so strike and dip are automatically set to zero. The programs have flags that can be set so that the Q values, strike, and dip will be considered. See the comments at the top of the programs (program names are given below) for details. Keep in mind that the solutions that you get back from the inversion will have the same layer dimensions as the starting model.

Inverting with "Manyinv"

The program **manyinv** takes the initial model that you give it and iterates a specified number of times to a solution. It then perturbs ("tweeks") the initial model slightly and iterates again. The process continues for as many times as you tell it to "tweek" the initial model (usually 24). The program is initiated through a shellscript called **srun1**. This script contains the information that the inversion programs needs to run. The contents of **srun1** are shown in Figure C6, with a brief description of what each item in the script represents (below dotted line). The descriptions are self−explanatory with the possible exeption of the few items decribed below.

```
40 BR STD VMODEL
 1    4.0000   2.0500   1.9100   0.5000   600.00   300.00   0.0000   0.0000
 2    4.0000   2.0500   1.9100   0.5000   600.00   300.00   0.0000   0.0000
 3    4.9000   2.6750   2.2800   1.0000   600.00   300.00   0.0000   0.0000
 4    4.9000   2.6750   2.2800   1.0000   600.00   300.00   0.0000   0.0000
 5    4.9000   2.6750   2.2800   1.0000   600.00   300.00   0.0000   0.0000
 6    5.2600   2.9250   2.4280   1.0000   600.00   300.00   0.0000   0.0000
 7    5.6200   3.1750   2.5760   1.0000   600.00   300.00   0.0000   0.0000
 8    5.8125   3.3100   2.6531   1.0000   600.00   300.00   0.0000   0.0000
 9    5.8375   3.3300   2.6594   1.0000   600.00   300.00   0.0000   0.0000
10    5.8265   3.3500   2.6656   1.0000   600.00   300.00   0.0000   0.0000
11    5.8875   3.3700   2.6719   1.0000   600.00   300.00   0.0000   0.0000
12    5.9215   3.3900   2.6781   1.0000   600.00   300.00   0.0000   0.0000
13    5.9375   3.4100   2.6844   1.0000   600.00   300.00   0.0000   0.0000
14    5.9625   3.4300   2.6906   1.0000   600.00   300.00   0.0000   0.0000
15    6.0000   3.4600   2.7000   1.0000   600.00   300.00   0.0000   0.0000
16    6.0000   3.4600   2.7000   1.0000   600.00   300.00   0.0000   0.0000
17    6.0000   3.4600   2.7000   1.0000   600.00   300.00   0.0000   0.0000
18    6.0000   3.4600   2.7000   1.0000   600.00   300.00   0.0000   0.0000
19    6.0000   3.4600   2.7000   1.0000   600.00   300.00   0.0000   0.0000
20    6.0000   3.4600   2.7000   1.0000   600.00   300.00   0.0000   0.0000
21    6.0200   3.4720   2.7040   1.0000   600.00   300.00   0.0000   0.0000
22    6.0400   3.4840   2.7080   1.0000   600.00   300.00   0.0000   0.0000
23    6.0600   3.4960   2.7120   1.0000   600.00   300.00   0.0000   0.0000
24    6.0900   3.5140   2.7180   1.0000   600.00   300.00   0.0000   0.0000
25    6.1250   3.5345   2.7280   1.0000   600.00   300.00   0.0000   0.0000
26    6.1750   3.5635   2.7440   1.0000   600.00   300.00   0.0000   0.0000
27    6.2250   3.5925   2.7600   1.0000   600.00   300.00   0.0000   0.0000
28    6.2750   3.6215   2.7760   1.0000   600.00   300.00   0.0000   0.0000
29    6.3250   3.6505   2.7920   1.0000   600.00   300.00   0.0000   0.0000
30    6.3750   3.6795   2.8080   1.0000   600.00   300.00   0.0000   0.0000
31    6.4250   3.7085   2.8240   1.0000   600.00   300.00   0.0000   0.0000
32    6.4750   3.7375   2.8400   1.0000   600.00   300.00   0.0000   0.0000
33    6.5250   3.7665   2.8560   1.0000   600.00   300.00   0.0000   0.0000
34    6.6000   3.8100   2.8800   1.0000   600.00   300.00   0.0000   0.0000
35    7.8000   4.5000   3.2700   3.1250   600.00   300.00   0.0000   0.0000
36    7.8250   4.5563   3.2797   3.1250   600.00   300.00   0.0000   0.0000
37    7.8500   4.6125   3.2895   3.1250   600.00   300.00   0.0000   0.0000
38    7.8875   4.6969   3.3041   3.1250   600.00   300.00   0.0000   0.0000
39    7.9062   4.7124   3.3105   6.2250   600.00   300.00   0.0000   0.0000
40    7.9187   4.6871   3.3135   0.0000   600.00   300.00   0.0000   0.0000

**********************************************************************

# layers    velocity model name
layer#  Vp       Vs     den.  thickness   Qp        Qs    strike    dip

       (km/s)   (km/s) (g/cm)    (km)                    (deg.)    (deg.)

**********************************************************************
```

Figure C4. Initial model brstd in the format required by inversion programs. Explanation of the model contents is provided beneath the model (inside asterisk lines -- NOT part of model).

```
25 HARTSE STD VMODEL
 1   5.9500  3.4100  2.7000  0.5000  600.00  300.00  0.0000  0.0000
 2   5.9500  3.4100  2.7000  0.5000  600.00  300.00  0.0000  0.0000
 3   5.9500  3.4100  2.7000  1.0000  600.00  300.00  0.0000  0.0000
 4   5.9500  3.4100  2.7000  2.0000  600.00  300.00  0.0000  0.0000
 5   5.9500  3.4100  2.7000  2.0000  600.00  300.00  0.0000  0.0000
 6   5.9500  3.4100  2.7000  2.0000  600.00  300.00  0.0000  0.0000
 7   5.9500  3.4100  2.7000  2.0000  600.00  300.00  0.0000  0.0000
 8   5.8000  3.4400  2.7500  2.0000  600.00  300.00  0.0000  0.0000
 9   5.8000  3.4400  2.7500  2.0000  600.00  300.00  0.0000  0.0000
10   5.8000  3.4400  2.7500  2.0000  600.00  300.00  0.0000  0.0000
11   5.8000  3.4400  2.7500  2.7500  600.00  300.00  0.0000  0.0000
12   3.2500  1.0000  2.6000  0.2500  600.00  300.00  0.0000  0.0000
13   6.4000  3.6500  2.9000  2.0000  600.00  300.00  0.0000  0.0000
14   6.4000  3.6500  2.9000  2.0000  600.00  300.00  0.0000  0.0000
15   6.4000  3.6500  2.9000  2.0000  600.00  300.00  0.0000  0.0000
16   6.4000  3.6500  2.9000  2.0000  600.00  300.00  0.0000  0.0000
17   6.4000  3.6500  2.9000  2.0000  600.00  300.00  0.0000  0.0000
18   6.4000  3.6500  2.9000  2.0000  600.00  300.00  0.0000  0.0000
19   6.4000  3.6500  2.9000  2.0000  600.00  300.00  0.0000  0.0000
20   8.1000  4.3500  3.3000  2.0000  600.00  300.00  0.0000  0.0000
21   8.1000  4.3500  3.3000  4.0000  600.00  300.00  0.0000  0.0000
22   8.1000  4.3500  3.3000  4.0000  600.00  300.00  0.0000  0.0000
23   8.1000  4.3500  3.3000  4.0000  600.00  300.00  0.0000  0.0000
24   8.1000  4.3500  3.3000  4.0000  600.00  300.00  0.0000  0.0000
25   8.1000  4.3500  3.3000  0.0000  600.00  300.00  0.0000  0.0000
```

Figure C5. Initial model hartse.m for the Socorro area. Note that the number of layers and the layer thicknesses are different from the model brstd. Format is the same as shown in Figure C4.

```
/usr/local/bin/manyinv > srun1.log <<end
hartse.m
1.0
7.8
20.
4
0.3
6
1
nw_2.5_0.1.rad.stk
.068
5.
end
-----------------------------------------
initial model
maximum cubic perturbation
stop perturbing at this velocity
maximum random perturbation (in % of
   cubic perturbation)
maximum # of iterations per inversion
smoothness trade-off parameter
# of inversions (x 4) 6 => 24 inversions
# waveforms
sac file name(s)
slowness
waveform delay
```

Figure C6. Contents of shell-script **srun1**, which invokes the inversion program **manyinv**. Explanation of contents provided beneath the dotted line. See text for details.

```
r inv.mdl.1504.vs inv.mdl.1704.vs inv.mdl.1804.vs
xlim 1 6
ylim -60 2
fileid l ll
line inc on
xvport .1 .4
yvport .1 .9
title "Inversion Models" si m
xlabel 'Vs [km/sec]'
ylabel 'Depth [km]'
p2
xlim off
ylim -0.2 0.7
r nw_2.5_stack.eqr syn01.1504 syn01.1704 syn01.1804
add .2 0 0 0
ch b -5
fileid l ur
xvport .5 .9
yvport .4 .9
title "Comparison of Data and Synthetics" si m
ylabel off
xlabel 'Seconds'
plabel 'Data from the' on s m b p 0.64 0.21 0
plabel 'Northwest Backazimuth' on s m b p 0.6 0.16
p2
```

Figure C7. Contents of SAC macro **pltmac1**, which is used to plot results from **manyinv**. See text for details.

-- The cubic and random perturbation values can pretty much be left alone

-- The smoothness trade-off parameter usually varies from 0.1 (least smoothing) to 0.5 (most smoothing). 0.2 of 0.3 are usually safe ground, but the situation would dictate.

-- The slowness can be calculated from the average depth and distance of the stacked events by using the IASPEI Seismological Tables.

-- The waveform delay gives some time before the first arrival on the resulting synthetics (30 seconds is usually a good value).

Once you have edited **srun1** for a specific inversion, you must make a directory (e.g /inv1) and place the following three items in that directory: the stacked receiver function (a SAC file), the initial model, and **srun1**. Make sure that the initial model and the SAC filename listed in **srun1** are the same ones that you placed in the directory. To initiate the inversion, type

% csh srun1& (the "&" places the job in background)

Depending on how many layers the initial model has, the inversion can take from 1 to 2.5 hours (take a nap).

The output from **manyinv** is plentiful and comes in two forms. First is the ASCII files that are simply velocity model solutions in the same format as the initial model. They will be called:

inv.mdl.XXYY

where XX is the inversion number (01-24) and YY is the iteration number (00-04). The second form of output are the synthetic receiver functions (SAC files) that correspond to the above velocity models. They will be called

syn01.XXYY (Where XX and YY are the same as above)

Inverting with "Snglinv"

As discussed above, **manyinv** perturbs the initial model 24 times, thus creating 24 solutions. The program **snglinv** simply runs the inversion one time using the exact initial model given. The inversion will iterate as many times as you request. **Snglinv** is not initiated with the **srun1** script as **manyinv** was. You have to enter the information interactively. The following is a sample run with **snglinv**.

```
% snglinv
Input velocity model:
% brstd
Enter the max number of iterations:
% 8
Enter the smoothness tradeoff parameter:
% 0.2
Input inversion ID number (for output naming):
% 01
number of seismograms:
% 1
sac file:
% se_2.5_0.001.rad.stk
slowness:
% 0.07
delay:
% 5.
```

The output from **snglinv** will look like

inv.mdl.XXYY and syn01.XXYY

where XX is the inversion ID number (01 above), and YY is the iteration number.

Inverting with "smthinv"

Smthinv is a program that will invert using just one initial model, but with 10 different smoothness parameters. You enter the minimum and maximum smoothness parameters, as well as the number of iterations per inversion, and the program will invert 10 times, once for each of the 10 (evenly spaced) smoothness parameters between the min and max values that you specify. The following is a sample run using **smthinv**.

```
% smthinv
Input velocity model:
% brstd
Enter the max number of iterations per inversion:
% 8
Enter the minimum smoothing tradeoff parameter:
% 0.1
Enter the maximum smoothing tradeoff parameter:
% 0.4
number of seismograms:
% 1
sac file:
% se_2.5_0.001.rad.stk
slowness:
% 0.07
delay:
% 5.
```

The output from **smthinv** is just like the output from **snglinv** except that XX will now be from 01 to 10, representing the 10 smoothness parameters used. YY is still the iteration number.

Looking at Inversion Output

There are a number of ways to look at the results of the inversion programs discussed above. Key programs for doing so include:

vplot pltmac1 manyvplot mktable

*Using "**vplot**"*

The program **vplot** creates plots of P−wave and S−wave velocity profiles as well as density profiles in SAC format for any given ASCII format inversion result. To execute **vplot** just type:

%vplot inv.mdl.1404 (or whichever model you want)

The program returns three SAC files:

inv.mdl.1404.vp
inv.mdl.1404.vs
inv.mdl.1404.rho

To look at the resulting profile in SAC:

```
sac> qdp off
sac> bd x
sac> macro mkbox          (sets up plot limits and box corners)
sac> r inv.mdl.1404.vp    (or whichever you want to look at)
sac> p                    (plots the profile)
```

*Using "**manyvplot**"*

A common way to convert the ASCII velocity files to SAC profiles for the output of **manyinv** is with a program called **manyvplot**. This program requires an input file that lists all of the models that you wish to convert to

P–velocity profiles (not S or density here!). The input file that is commonly used is called "Models" and is simply a list of the fourth iteration of all 24 solution models for a given inversion. You can, of course, change the list to whatever you want. To run **manyvplot**, just type:

```
% manyvplot
MANYVPLOT – Input filename (contains list):
% Models     (make sure Models is in the working directory)
```

The output will be .vp files for all of the fourth iterations of the models listed in Models. Even though the 00–03 iterations are present, the fourth is usually the solution of interest. You can look at all 24 .vp files individually and select velocity profiles that are similar enough to be grouped together into solution "families". Do this just like you would with the vplot results except that you must read all 24. For example:

```
sac> r *.vp
sac> macro mkbox
sac> p    (one will plot; hit RETURN to move through all 24)
```

*Using **"pltmac1"***

Pltmac1 is a SAC macro used for plotting the SAC–format velocity profiles created with **vplot** or **manyvplot** on the same page that compares the corresponding synthetic seismograms to the data. **Pltmac1** is not a permanently installed SAC macro because you need to edit it each time you use it, so you just want to keep it someplace where you know that it will always be. As shown in Figure C7, **pltmac1** has two read lines, one at the very top and one about half way down. In the first read line, you want to list the velocity profiles (the .vp files) that you want to display. For **manyinv** output you would probably want to list all the the .vp files that make up a "family" of solutions. In the second line, you put the name of the data stack followed by the list of the synthetics corresponding to the models listed in the first read line. The rest of the lines are SAC plotting commands which are described in detail in the SAC manual. To run **pltmac1**, just type the following commands while in SAC:

```
sac> bf          (begin frame for 2 plots on one page)
sac> macro <PATH> pltmac1
sac> ef          (end frame)
```

Since **pltmac1** is not installed, you must provide a path if the macro is not in the working directory. To generate a SAC graphics file so that you can print out the plot, just type the "bg sgf" command before the "bf" so that a .sgf file will be created. The resulting plot will look like the example shown in Figure C8.

*Using "**mktable**"*

The program **mktable** is program that is specific to the 24 model output from **manyinv, mktable** gives average velocities for each model and cross–correlation values between the first 12.5 seconds of the corresponding synthetic and the stack. The program is presently set up to give averages from 0–10 km, from 10–20 km and from 20 km to the Moho depth, which is defined by the depth at which the P–wave velocity first reaches 7.8 km/s or greater. The depths for averages can be easily changed by altering the program mktable.f. **Mktable** will ask you for the names of the initial model and the stack. An example run would look like:

```
% mktable
specify receiver stack:
% se_2.5_0.001.rad.stk
specify initial model:
% brstd
```

The output will be in an ASCII file called "table", which can be looked at with the "more" command. An example "table" is provided in Figure C9

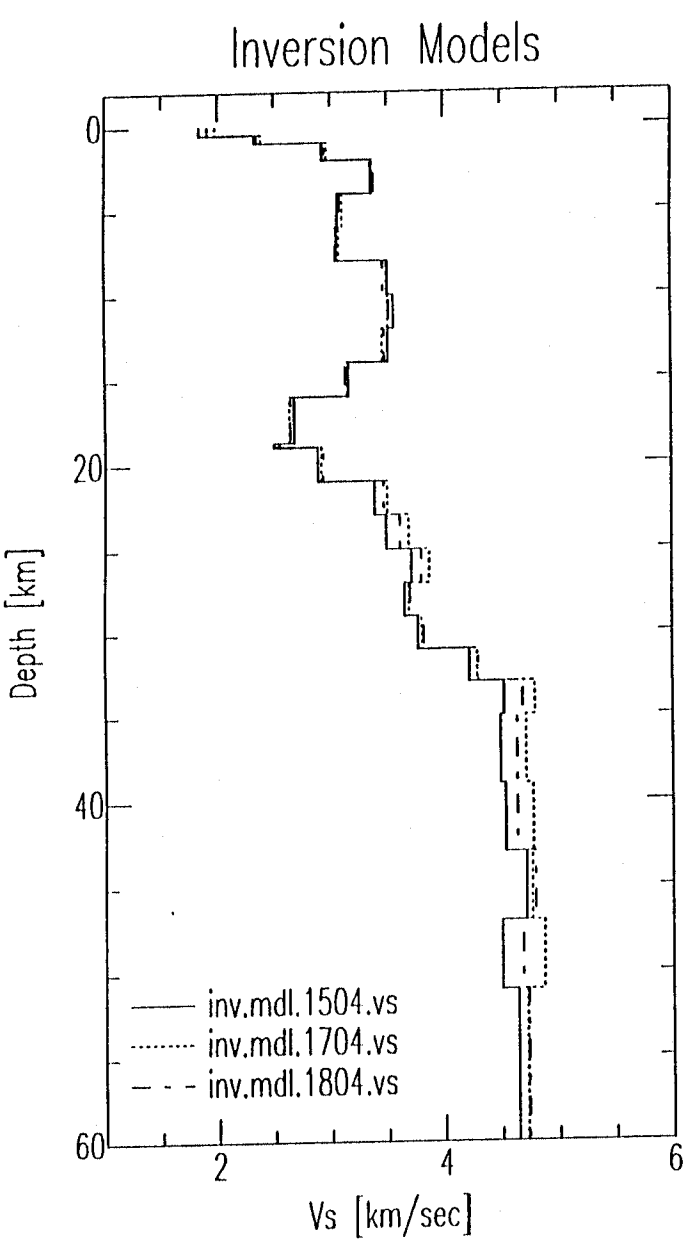

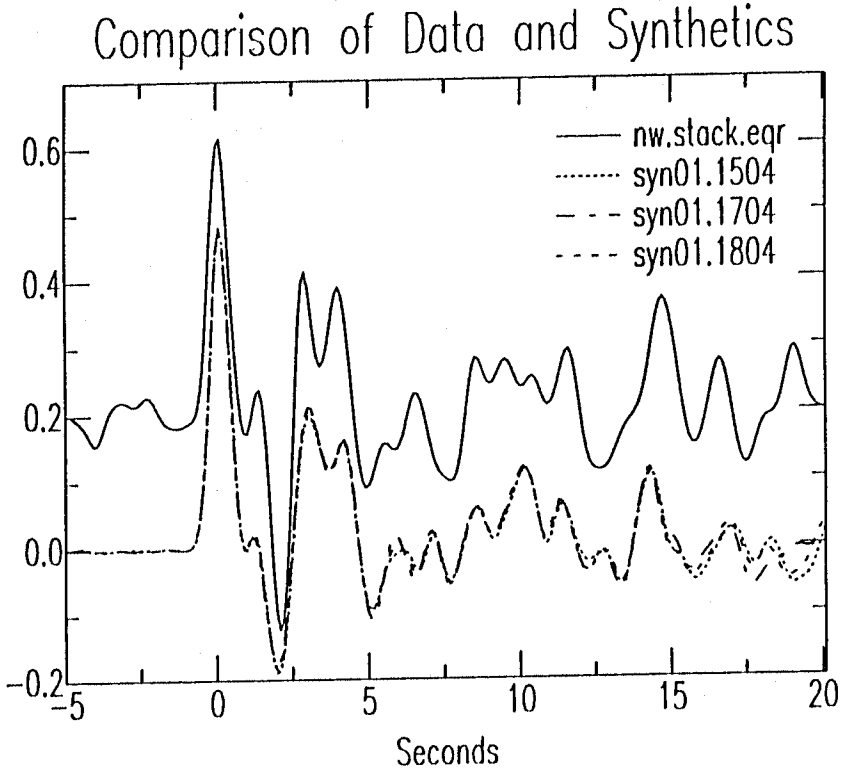

Figure C8. Output from SAC macro **pltmac1**. Overlay of velocity profiles (left plot) and comparison of corresponding synthetics to the stacked data (right plot).

STACKED RECEIVER FUNCTION: data.stack.rad INIT. MODEL: hartse.m

Hartse:	3.41	3.44	3.65	4.40	5.95	5.80	6.40	8.10	33.0	
	S avgs				P avgs				depth	corr
	upper	mid	low	mant	upper	mid	low	mant		
.0104	3.56	2.38	3.24	NaN	6.18	4.13	5.61	NaN	51.0	0.89
.0204	3.68	2.78	3.18	NaN	6.38	4.81	5.52	NaN	51.0	0.91
.0304	4.01	3.16	3.35	4.69	6.94	5.47	5.81	8.13	35.0	0.90
.0404	4.06	3.47	3.49	4.72	7.02	6.01	6.04	8.18	35.0	0.92
.0504	4.02	3.60	3.68	4.59	6.96	6.23	6.37	7.96	39.0	0.93
.0604	4.04	3.62	3.78	4.77	7.00	6.28	6.55	8.27	39.0	0.92
.0704	3.56	2.49	3.47	NaN	6.16	4.32	6.02	NaN	51.0	0.91
.0804	3.73	2.91	3.32	NaN	6.46	5.05	5.74	NaN	51.0	0.92
.0904	3.97	3.14	3.33	4.63	6.88	5.44	5.77	8.02	35.0	0.91
.1004	4.05	3.58	3.66	4.76	7.02	6.20	6.35	8.25	39.0	0.93
.1104	4.03	3.65	3.81	4.81	6.99	6.32	6.60	8.32	39.0	0.92
.1204	4.05	3.63	3.80	4.77	7.01	6.29	6.58	8.26	39.0	0.92
.1304	4.09	3.30	3.45	3.69	7.08	5.71	6.39	6.40	39.0	0.91
.1404	3.43	3.57	3.82	NaN	5.94	6.18	6.61	NaN	51.0	0.94
.1504	3.41	3.47	3.56	NaN	5.91	6.01	6.16	NaN	51.0	0.95
.1604	3.50	3.15	3.65	NaN	6.06	5.45	6.33	NaN	51.0	0.92
.1704	3.42	3.43	3.68	NaN	5.92	5.94	6.38	NaN	51.0	0.94
.1804	3.26	3.35	3.67	NaN	5.63	5.80	6.35	NaN	51.0	0.92
.1904	4.01	3.57	3.69	4.70	6.95	6.18	6.38	8.15	39.0	0.93
.2004	3.43	3.71	3.59	4.54	5.93	6.42	6.21	7.87	39.0	0.95
.2104	3.45	3.28	3.71	NaN	5.97	5.68	6.43	NaN	51.0	0.93
.2204	3.27	2.83	3.79	NaN	5.66	4.90	6.56	NaN	51.0	0.91
.2304	3.29	2.85	3.77	NaN	5.70	4.93	6.53	NaN	51.0	0.91
.2404	3.18	2.81	3.78	NaN	5.50	4.86	6.55	NaN	51.0	0.92

Figure C9. Output from program **mktable**. Compares the average upper, middle, lower crustal, and mantle velocities to the velocities in the model provided by [Hartse, 1991] (top of table), for each of the 24 models resulting from running **manyinv**. Depth column corresponds to the Moho depth, defined by the depth where the P-velocity exceeds 7.8 km/s. NaN in mantle column means that 7.8 km/s was never reached. Corr column lists the correlation coefficient between the first 12.5 seconds of the model synthetic receiver function with the data.

Section VII: Forward Modeling

There are often times when you would like to create a velocity model and see what the receiver function would look like. To do this forward modelling, you need to use the program called **respknt** which will create the synthetic vertical and radial seismograms. You must then use **pwaveqn** just as before to deconvolve the synthetics. Say, for example, that you wanted to get a synthetic receiver function for the "brstd" model. Before running **respknt**, you need to decide on a sampling interval and you need to choose a slowness. The following example will create synthetic seismograms for the brstd model.

```
% respknt
velocity model name?
% brstd
list the site model (y or n)
% n      (Yes would just echo back the input model)
Incident P(1) or S(2) wave?
% 1
sampling interval?
% 0.1    (or whatever you want to use here)
signal duration?
% 30     (length in seconds of synthetic, whatever you want)
enter slowness
% 0.07   (for source ~ 45 degrees away and 40km depth)
partial(p) or full(f)
% f      (use full here)
mode conversions (y or n)
% y      (you probably want mode conversions)
```

The output will be a synthetic vertical and radial seismogram (SAC format) which will look like:

brstd_sp.z and brstd_sp.r

*If you had chosen an incident S wave, brstd_sp.t will also be created.

To get a synthetic receiver function, deconvolve using **pwaveqn**. First, however, you must copy the vertical over to a tangential component, because **pwaveqn** expects to see one. This, of course, means that your tangential receiver function will just be a delta function and rather useless. To deconvolve, just follow this example:

```
        % pwaveqn
specify quake file:
        % brstd
real data (y or n)
        % n          (synthetic, not real data this time)
window data (y or n)
        % n
specify outfil:
        % brstd
trough filler c=:
        % 0.001      (see NOTE 1 in section IV)
gaussian scale a=:
        % 2.5        (see NOTE 2 in section IV)
Enter phase shift:
        % 5.
try another (y or n)
        % n
```

Your output will be brstd.eqr and brstd.eqt. The latter of which can be disregarded if an incident P wave is chosen. The SAC file brstd.eqr, when plotted, should look like Figure C10.

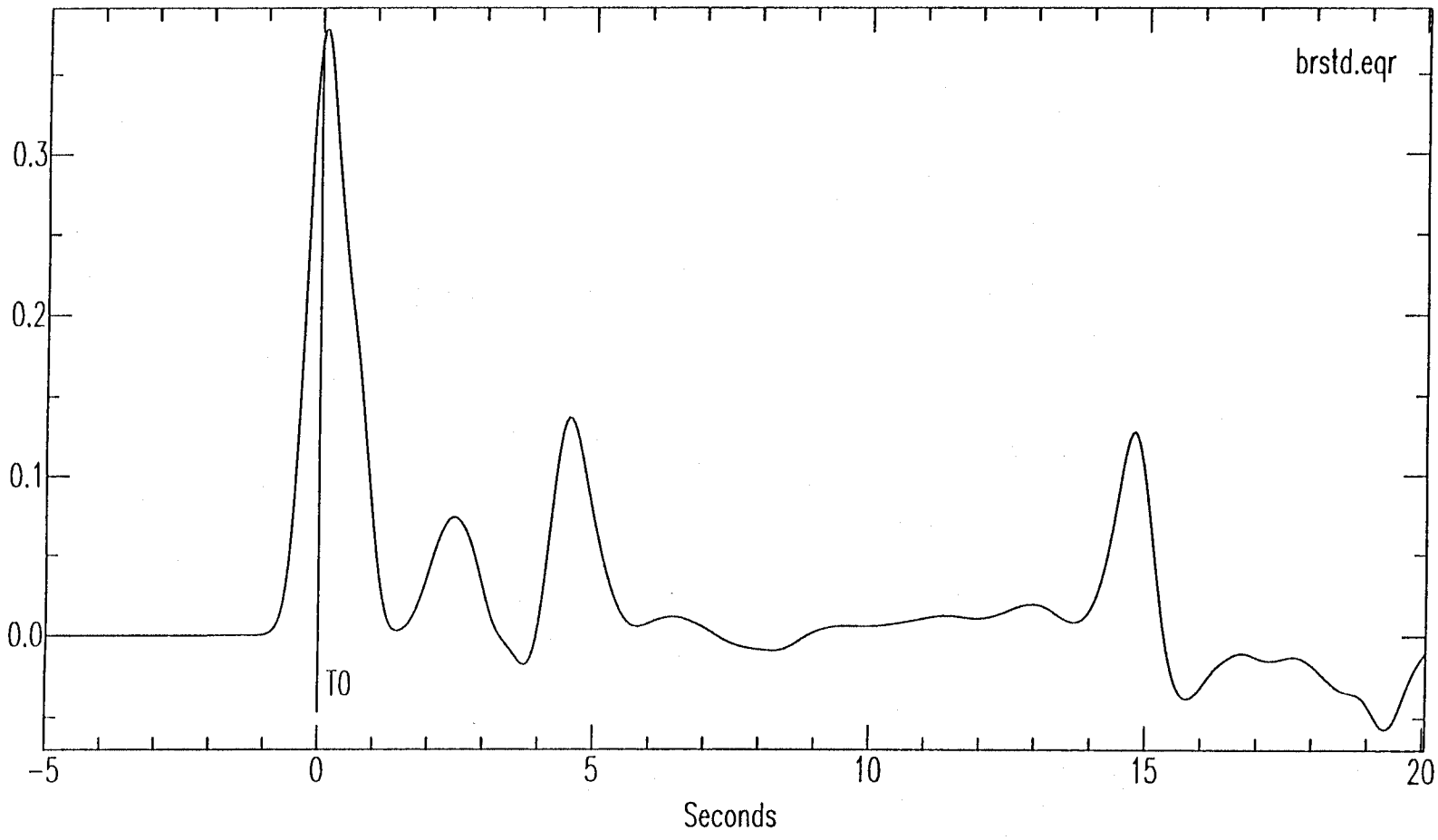

Figure C10. Synthetic radial receiver function for the brstd model. Gaussian filter width (a) = 2.5; water-level parameter (c) = 0.001.